

# **Parameterisation of the near surface by combined geophysical and direct push techniques in the frame of geotechnical site investigation**

## **Dissertation**

der Mathematisch-Naturwissenschaftlichen Fakultät  
der Eberhard Karls Universität Tübingen  
zur Erlangung des Grades eines  
Doktors der Naturwissenschaften  
(Dr. rer. nat.)

vorgelegt von  
Dipl.-Geol. Jörg Hausmann  
aus Meißen

Tübingen  
2013

Tag der mündlichen Qualifikation:

05.03.2014

Dekan:

Prof. Dr. Wolfgang Rosenstiel

1. Berichterstatter:

Prof. Dr. Peter Grathwohl

2. Berichterstatter:

Prof. Dr. Peter Dietrich

Dedication

---

*to my son*

---

---

## Abstract

Knowledge of the spatial distribution of geotechnical parameters in the near surface is essential in engineering geology. Latest developments in engineering geophysics and direct push-based (*DP*) data acquisition provide a large set of techniques for non-invasive and *in situ* data recording for high-resolution parameterisation. Different traditional but sparse geotechnical surveying and analysis tools are typically used at selected locations such as drillings and sieve analysis, respectively. *State-of-the-art* laboratory techniques and supporting field measurements are used to gather the relevant soil properties for soil type classification helping to assign this information to homogeneous sections of the ground (layers). Site-specific data interpretation however becomes challenging because actual field conditions (*in situ*) differ from those appropriated in the laboratory, owing to the high spatial heterogeneity of near-surface unconsolidated sediments. We performed intensive fieldwork at two test sites (Löbnitz and Taucha) representing typical construction grounds in Central Germany. We tested electrical resistivity tomography, ground penetrating radar, refraction seismic, multi-channel analysis of surface waves, and mobile *DP*-based seismic travelttime tomography. A combination can overcome the deficiencies restrictions of the particular individual methods, compensating the deficiencies of each method, helping therefore to minimise any drawbacks or limitations that depend on the contrast of and between the physical properties, which each technique is sensitive to. In developing mobile seismic tomography, we overcame prior restrictions imposed by existing on-site boreholes by using *DP*-devices as carrier systems. The derived geotechnical parameters allows us to carry out uncertainties evaluated by additional applied *DP*-methods gathering high-resolution data for ground truthing. Furthermore, we show that *DP*-based *in situ*-obtained soil colour yields information about the vertical stratigraphic pattern. So far, no methods exist that stipulate how best to handle such high-resolution data from colorimeter probes. We present improvements of direct data acquisition, numerical transformation, filtering, and interpretation. We found that filtered colour surrogates provide more detailed information about the soil which corresponds to its geological set-up. The results help us gain a new understanding of soil colours as a technically reliable proxy that is applicable in geotechnical site characterisation. The findings encourage an enable the reliable characterisation of a highly heterogeneous ground, especially for appraising information uncertainty at different scales. Compared with traditional sparse geotechnical measurements, we obtain more information for definition of clearly homogeneous sections (layers). The combined data interpretation compensates for any disadvantages of a single method. Thus, we expect a significant positive impact for near-surface characterisation in the frame of engineering geological investigations.

---

## Zusammenfassung

In der Ingenieurgeologie sind Kenntnisse über die Verteilung von geotechnischen Parametern im oberflächennahen Untergrund von entscheidender Bedeutung. Neueste Entwicklungen im Bereich der Ingenieurgeophysik und von Direct-Push-Verfahren (*DP*) bieten umfangreiche technische Möglichkeiten für nichtinvasive bzw. In-situ-Parametrisierung. Es kommen unterschiedliche, eher grobe, geotechnische Standarduntersuchungs- und Analyseverfahren zum Einsatz, z.B. Bohrungen und Siebanalysen. Standardisierte Labormethoden und unterstützende Geländemessungen zur Bestimmung relevanter Bodeneigenschaften sowie zur Bodentypbestimmung können Homogenbereichen (Schichten) im Untergrund zugeordnet werden. Die standortabhängige Interpretation dieser Daten ist jedoch schwierig, da die natürlichen Eigenschaften am Standort (*in situ*) auf Grund der stark heterogenen Natur oberflächennaher Lockergesteine von den Laborbedingungen abweichen. An zwei Standorten (Löbnitz und Taucha) wurden umfangreiche Feldarbeiten durchgeführt. Als Repräsentanten typischer Baugrundsituationen in Mitteldeutschland, wurden hier die Elektr. Widerstandstomographie, Bodenradar, Refraktionsseismik, multichannel analysis of surface waves sowie eine mobile, *DP*-basierte seismische Laufzeit tomographie getestet. Der kombinierte Einsatz gleicht Beschränkungen und Nachteile einzelner Verfahren aus, welche sich aus dem Kontrast bzw. der spezifischen Sensitivität gegenüber dem jeweilig gemessenen physikalischen Parameter ergeben. Durch den Einsatz von *DP*-Systemen in der Entwicklung einer mobilen, seismischen Tomographie kann die Abhängigkeit zu stationär vorhandenen Bohrlöchern überwunden werden. Die abgeleiteten geotechnischen Parameter erlauben eine Unsicherheitsabschätzung, evaluiert durch hochauflösende Daten zusätzlich durchgeführter *DP*-Methoden. Ferner ermöglichen *DP*-basierte In-situ-Bodenfarbmessungen mittels Colorimetersonden eine stratigraphische Modelbildung. Bisher sind für solcherart hochaufgelöster Daten keine Auswerterroutinen bekannt. Die Arbeit stellt Entwicklungen im Bereich der Datenakquisition, der numerischen Umrechnung, Filterung sowie Interpretation vor. Die gefilterten Farbdaten bilden als zusätzliche Bodeneigenschaft die geologischen Gegebenheiten ab. Die Ergebnisse belegen den Mehrwert von Bodenfarben als technisch belastbarer Kennwert zur Anwendung in der geotechnischen Standorterkundung. Die Schlussfolgerungen ermöglichen eine belastbare Parametrisierung stark heterogener Untergründe, insbesondere für Unsicherheitsabschätzung auf verschiedenen Skalen. Gegenüber traditionellen, eher groben geotechnischen Messverfahren erhöht sich der Informationsgewinn zu klar abgrenzbaren Homogenbereichen (Schichten). Die gemeinsame Dateninterpretation gleicht die Nachteile einzelner Methoden aus. Die Ergebnisse haben erhebliche Bedeutung für die oberflächennahe Charakterisierung im Rahmen ingenieurgeologischer Untersuchungen.

## Index

|   |       |
|---|-------|
| Abstract .....  | ii    |
| Zusammenfassung .....   | iii   |
| Index.....  | iv    |
| List of figures .....   | viii  |
| List of tables .....  | xiv   |
| List of symbols.....  | xvi   |
| List of Greek symbols .....   | xvii  |
| List of abbreviations .....   | xviii |
| 1 Introduction.....   | 1     |
| 1.1 Scope.....  | 1     |
| 1.2 Engineering geophysics for site characterisation .....                | 5     |
| 1.3 Direct push technologies for site characterisation .....              | 6     |
| 1.4 Outline .....   | 9     |
| 2 Field sites .....   | 11    |
| 2.1 The Löbnitz test site.....  | 11    |
| 2.2 The Taucha test site .....  | 13    |
| 3 Combined geophysical methods for structural site characterisation ..... | 17    |
| 3.1 Introduction .....  | 17    |
| 3.2 Field site .....  | 19    |
| 3.3 Methods .....   | 20    |
| 3.3.1 Electrical resistivity tomography ( <i>ERT</i> ) .....              | 20    |
| 3.3.2 Ground penetrating radar ( <i>GPR</i> ) .....                       | 21    |
| 3.3.3 Refraction seismic ( <i>RS</i> ).....                               | 22    |
| 3.3.4 Multichannel analysis of surface waves ( <i>MASW</i> ) .....        | 23    |
| 3.3.5 Soil sampling ( <i>SS</i> ) .....                                   | 28    |
| 3.4 Results.....  | 28    |
| 3.4.1 Electrical resistivity tomography ( <i>ERT</i> ) .....              | 28    |
| 3.4.2 Ground penetrating radar ( <i>GPR</i> ) .....                       | 29    |
| 3.4.3 Refraction seismic ( <i>RS</i> ).....                               | 29    |
| 3.4.4 Multichannel analysis of surface waves ( <i>MASW</i> ) .....        | 30    |
| 3.4.5 Soil sampling ( <i>SS</i> ) .....                                   | 30    |
| 3.5 Discussion .....  | 31    |

---

|       |   |    |
|-------|---|----|
| 4     | Mobile <i>DP</i> -based seismic travelttime tomography for geotechnical site characterisation | 37 |
| 4.1   | Introduction  | 37 |
| 4.2   | Field site  | 39 |
| 4.3   | Methods   | 39 |
| 4.3.1 | Seismic travelttime tomography ( <i>STT</i> )   | 39 |
| 4.3.2 | Processing and model generation   | 41 |
| 4.3.3 | Calculation of geotechnical parameters from seismic velocities                                | 42 |
| 4.3.4 | Soil sampling ( <i>SS</i> )   | 44 |
| 4.3.5 | Cone penetration testing ( <i>CPT</i> )   | 44 |
| 4.4   | Results   | 45 |
| 4.4.1 | Quality of seismic data   | 45 |
| 4.4.2 | Geotechnical parameters from seismic velocities   | 49 |
| 4.4.3 | Comparison of obtained velocities with soil sampling ( <i>SS</i> ) and <i>CPT</i>             | 54 |
| 4.5   | Discussion  | 56 |
| 5     | Processing of <i>in situ</i> -obtained soil colours ( <i>SC</i> )                             | 59 |
| 5.1   | Introduction  | 59 |
| 5.2   | Background: optical-based site characterisation   | 60 |
| 5.3   | Field site  | 62 |
| 5.4   | Methods   | 63 |
| 5.4.1 | Colour logging tool ( <i>CLT</i> )  | 63 |
| 5.4.2 | Soil sampling ( <i>SS</i> )   | 65 |
| 5.4.3 | Numerical transformation of <i>in situ</i> -obtained <i>SC</i>                                | 65 |
| 5.4.4 | The <i>CIEXYZ</i> -colour space   | 66 |
| 5.4.5 | The <i>CIExyZ</i> -colour space   | 67 |
| 5.4.6 | The <i>CIEL*a*b*</i> -colour space  | 67 |
| 5.4.7 | The <i>CIEL*c*h*</i> -colour space  | 69 |
| 5.4.8 | The <i>RGB</i> -colour space and <i>RGB</i> -indices  | 69 |
| 5.4.9 | Denoising strategies  | 70 |
| 5.5   | Results   | 72 |
| 5.5.1 | Soil sampling ( <i>SS</i> )   | 72 |
| 5.5.2 | Resolution of <i>in situ</i> -obtained <i>SC</i> -data  | 74 |
| 5.5.3 | Colour reduction within <i>sRGB</i> -colour space   | 74 |
| 5.5.4 | Wavelet transformation ( <i>WT</i> )  | 75 |
| 5.5.5 | Comparison of repeated measurements   | 76 |
| 5.6   | Discussion  | 77 |

|       |  |     |
|-------|--|-----|
| 6     | <i>In situ</i> -obtained soil colours ( <i>SC</i> ) for geotechnical site characterisation .....                 | 83  |
| 6.1   | Introduction .....   | 83  |
| 6.2   | Methods .....  | 84  |
| 6.2.1 | Cone penetration testing ( <i>CPT</i> ).....   | 84  |
| 6.2.2 | Electrical conductivity logging ( <i>DPEC</i> ) .....  | 84  |
| 6.2.3 | Soil moisture probing ( <i>SMP</i> ) .....   | 85  |
| 6.2.4 | Colour logging tool ( <i>CLT</i> ) .....   | 86  |
| 6.2.5 | Soil sampling ( <i>SS</i> ) .....  | 86  |
| 6.3   | Results.....   | 87  |
| 6.3.1 | Comparison of <i>CLT</i> -data with cone penetration testing ( <i>CPT</i> ) and soil sampling ( <i>SS</i> )..... | 87  |
| 6.3.2 | Comparison of <i>CLT</i> -data with soil moisture probing ( <i>SMP</i> ).....                                    | 93  |
| 6.3.3 | Comparison of <i>CLT</i> -data with electrical conductivity logging ( <i>DPEC</i> ) .....                        | 93  |
| 6.4   | Discussion .....   | 94  |
| 7     | Conclusion.....  | 97  |
|       | References .....   | 101 |
|       | Contributions .....  | 111 |
|       | Acknowledgment.....  | 113 |
|       | Appendix A .....   | 115 |
|       | Appendix B .....   | 117 |
|       | Curriculum Vitae.....  | 119 |

---

---

## List of figures

|  |    |
|--|----|
| Figure 1-1: Flow chart for two-phase site investigation adopted from KNÖDEL ET AL. (2007), supplemented by exemplary actions (right column); * <i>DP</i> -methods allow on-site decision-making.....   | 3  |
| Figure 2-1: A) Recent Mulde valley close to Löbnitz in northern Saxony (Germany); composition of surface waters, drainage channels, and indications of abandoned river channels condensed from aerial photos; B) Detailed section with the test site location (recorded profile), which follows the dike path by crossing an oxbow structure (HAUSMANN, ET AL., 2013; modified). .....   | 12 |
| Figure 2-2: A) Location of the mining area close to Taucha in northern Saxony (Germany) condensed from aerial photos; B) Detailed section of the test site location (recorded probing cluster), which is located in a sand pit; C) Probing cluster at 80- m position along the profile with locations of the applied <i>DP</i> -probing (→ Chapter 4, Appendix B). .....   | 14 |
| Figure 3-1: Assumed cross section (NE-SW) of the internal geomorphological structure of the abandoned oxbow in the study area according to EISSMANN (1994) and field observations with geological set-up; HAUSMANN, ET AL. (2013). .....   | 20 |
| Figure 3-2: Measurement principle of a multi-electrode WENNER-configuration for D.C. <i>ERT</i> (KNÖDEL ET AL., 1997; modified). .....   | 24 |
| Figure 3-3: Measurement principle of <i>ground penetrating radar (GPR)</i> (KNÖDEL ET AL., 1997; modified).....  | 24 |
| Figure 3-4: Measurement principle of <i>refraction seismic (RS)</i> . .....  | 24 |
| Figure 3-5: Measurement principle of <i>multichannel analysis of surface waves (MASW)</i> . .....  | 25 |
| Figure 3-6: Processing scheme of bidirectional <i>MASW</i> profiling exemplarily illustrated for 49.5- m mid-spread position of the Löbnitz profiles; shooting is performed from NW and SE direction for the same mid-spread position. The resulting dispersion curves for 4 and 8- m offsets are combined and then inverted via genetic algorithm (PAROLAI ET AL. 2005; PICOZZI ET AL. 2005; PILZ ET AL. 2010; BOXBERGER ET AL. 2011); from STEINEL ET AL. (SUBMITTED). ... | 27 |
| Figure 3-7: A) <i>ERT</i> electrical resistivity $\rho$ [ohm-m]; B) <i>GPR</i> reflection pattern; C) <i>RS</i> refraction seismic P-wave velocity $v_p$ [m/s]; D) <i>MASW</i> S-wave velocity $v_s$ [m/s]; Soil cores (L/SON-1 – L/SON-5; Appendix B; colour-coded according to the occurring dominant grain size component) in comparison with results from geophysical surveys, five times (5x) super-elevated (HAUSMANN ET AL., 2013; modified). .....                   | 32 |
| Figure 3-8: Depth distribution and joint interpretation of the geomorphological structures based on <i>MASW</i> S-wave velocity $v_s$ [m/s]; also included isoline of refraction seismic ( <i>RS</i> ) P-  |    |

List of figures

---

|   |    |
|---|----|
| wave velocity $v_p$ [m/s], <i>ERT</i> electrical resistivity $\rho_s$ at $\sim 200 \Omega\text{-m}$ , and <i>GPR</i> reflections; five times (5x) super-elevated (HAUSMANN ET AL., 2013). .....   | 33 |
| Figure 4-1: Location of the <i>DP</i> -based mobile crosshole seismic experiment; A) General site location ( $\rightarrow$ Figure 2-1); B) Location of the temporarily installed boreholes (S1 = 82 m, S2/R2/R4 = 92 m, R2/S4/S3 = 102 m, R3 = 112 m) and L/CPT-1.....  | 38 |
| Figure 4-2: Experimental design, components, and exemplary shot gather of <i>DP</i> -based seismic travelttime tomography developed in the framework of the <i>MuSaWa</i> -project.....   | 40 |
| Figure 4-3: Example of recorded seismic traces from 82–92- m profile section (reversely polarized shots); geophone B1 position = shot position +0.2 m ( $\rightarrow$ Figure 4-2).....  | 46 |
| Figure 4-4: Source-to-receiver travelttime analyses for P-wave $v_p$ and S-wave velocity $v_s$ ; two times (2x) super-elevated.....   | 47 |
| Figure 4-5: P-wave velocity $v_p$ model ensemble from <i>PSO</i> ; A) Q1; B) Q2; C) Q3; D) relative error $f$ ; all plots are two times (2x) super-elevated. ....   | 48 |
| Figure 4-6: S-wave velocity $v_s$ model ensemble from <i>PSO</i> ; A) Q1; B) Q2; C) Q3; D) relative error $f$ ; all plots are two times (2x) super-elevated. ....   | 48 |
| Figure 4-7: Velocity ratio $v_p/v_s$ model ensemble from <i>PSO</i> ; A) Q1; B) Q2; C) Q3; D) relative error $f$ ; all plots are two times (2x) super-elevated. ....  | 50 |
| Figure 4-8: Solid weight $\gamma_p$ model ensemble from <i>PSO</i> ; A) Q1; B) Q2; C) Q3; D) relative error $f$ ; all plots are two times (2x) super-elevated.....  | 50 |
| Figure 4-9: P-wave modulus $M$ model ensemble from <i>PSO</i> ; A) Q1; B) Q2; C) Q3; D) relative error $f$ ; all plots are two times (2x) super-elevated. ....  | 51 |
| Figure 4-10: Shear modulus $\mu$ model ensemble from <i>PSO</i> ; A) Q1; B) Q2; C) Q3; D) relative error $f$ , all plots are two times (2x) super-elevated. ....  | 51 |
| Figure 4-11: Young’s modulus $E$ model ensemble from <i>PSO</i> ; A) Q1; B) Q2; C) Q3; D) relative error $f$ ; all plots are two times (2x) super-elevated. ....  | 52 |
| Figure 4-12: Bulk modulus $K$ model ensemble from <i>PSO</i> ; A) Q1; B) Q2; C) Q3; D) relative error $f$ ; all plots are two times (2x) super-elevated. ....   | 52 |
| Figure 4-13: Poisson’s ratio $\sigma$ model ensemble from <i>PSO</i> ; A) Q1; B) Q2; C) Q3; D) relative error $f$ ; all plots are two times (2x) super-elevated. ....   | 53 |
| Figure 4-14: Gravimetric water content $\omega$ model ensemble from <i>PSO</i> ; A) Q1; B) Q2; C) Q3; D) relative error $f$ ; all plots are two times (2x) super-elevated.....  | 53 |
| Figure 4-15: Results from <i>CPT</i> (L/CPT-1) and <i>SS</i> (L/SON-5); A) Dynamic pore water pressure $u_2$ , sleeve friction $f_s$ , corrected cone resistance $q_t$ , and friction ration $R_f$ (color coded to interpretation in B) and core results (green = silt, orange = dominantly sandy, white = core |    |

|  |    |
|--|----|
| loss/no data); groundwater level in borehole at 2.48 m depth; B) Colour coded lithological interpretation from ratio between corrected cone resistance $q_t$ and friction ratio $R_f$ according to ROBERTSON ET AL. (1986); 1 - sensitive fine grained, 2 - organic material, 3 - clay, 4 - silty clay to clay, 5 - clayey silt to silty clay, 6 - sandy silt to clayey silt, 7 - silty sand to sandy silt, 8 - sand to silty sand, 9 - sand, 10 - gravelly sand to sand, 11 - very stiff fine grained*, 12 - sand to clayey sand* [*over-consolidated or cemented]. .....   | 54 |
| Figure 4-16: A) L/CPT-1-log (friction ratio $R_f$ ) and core results from sonic drilling (L/SON-5) indicating the found layers (Table 4-1); B) One-dimensional profiles of geotechnical parameters calculated from jointly inverted P/-waves ( $PSO$ ) given as $Q2$ (black line), $Q1$ and $Q3$ (grey lines): P-wave velocity $v_p$ ; S-wave velocity $v_s$ ; velocity ratio $v_p/v_s$ ; unit weight from P-wave velocity $\gamma_p$ ; gravimetric water content $\omega$ ; P-wave modulus $M$ ; shear modulus $\mu$ ; Young's modulus $E$ ; Bulk modulus $K$ ; Poisson's ratio $\sigma$ ;  | 55 |
| Figure 5-1: Comparison of raw data from vertical $SC$ -profiles (T/CLT-80/1; T/CLT-80/3; T/CLT-80/5) to core pull (T/DT-1), investigation depth 9.54–10.76 m (total length: 1.22 m); core pull shows high vertical and lateral variation in the mm-scale (stretched to $x$ -direction by factor 2.5 for better visualisation); <i>in situ</i> $SC$ -measurements are given in $RGB$ .  | 60 |
| Figure 5-2: $CLT$ -components applied on $DP$ -rig.  | 64 |
| Figure 5-3: Conjunctural figure transforming colorimeter tristimuli data $XYZ$ in norm standardised colour systems; a) Normal distribution of the three colour matching functions $x_\lambda$ , $y_\lambda$ , $z_\lambda$ (CIE, 1931); b) $CIEXYZ$ -colour system (CIE, 1931) with the proportions of the tristimuli $XYZ$ gained by conversion of the colour matching functions; c) CIE (1931) 2°-degree standard colorimetric observer and CIE 1964 10°-supplementary standard colorimetric observer within the $CIE_{xy}Y$ -system with added wavelength in nm ; d) Cubic $RGB$ -colour system as a mixture between $R$ – red, $G$ – green, and $B$ – blue base colours; e) Cartesian $CIEL^*a^*b^*$ -colour system with $L^*$ - luminosity (0 – 100), green-red ratio $a^*$ , and blue-yellow ratio $b^*$ ; f) Cylindrical $CIEL^*c^*h^*$ -colour system with chroma $c^*$ and hue $h^*$ . | 64 |
| Figure 5-4: Processing flowchart from field data acquisition, numerical transformation of the raw data into a standardised colour system and associated denoising steps for enhanced data interpretation either using median filtering and colour reduction within the $RGB$ -colour space or wavelet transformation ( $WT$ ) approach. All symbols are explained in Table 5-1.....  | 70 |
| Figure 5-5: Stratigraphic interpretation and sieve analyses according to DIN 18123 for T/SON-1 at Taucha test site.....  | 73 |
| Figure 5-6: Distribution of $\Delta y$ for repeated colour logs.....   | 74 |
| Figure 5-7: Comparison of $RGB$ -data of T/CLT-80/1-colour profile (false coloured plots), median filter and colourreduction; A) Continuously increasing vertical median filter (window size in parenthesis as pixel values, e.g., 10 pixel (1 cm), 50 pixel (5 cm), etc.) and constant  |    |

|  |    |
|--|----|
| colour reduction to five colours; B) Constant median filtering (100 pixel = 10 cm) with increasing colour reduction (number in parentheses) from zero colour reduction (all), 30 to 5 colours.....   | 75 |
| Figure 5-8: Comparison of luminosity data from $CIEL^*a^*b^*$ -colour space from profile T/CLT-80/1; light grey = raw data; black = X-level(s) 50 % threshold HAAR-denoise.....  | 78 |
| Figure 5-9: Comparison of luminosity data from $CIEL^*a^*b^*$ -colour space from profile T/CLT-80/1; light grey = raw data; black = X-level(s) 50 % threshold DAUBLET4 denoise.....  | 78 |
| Figure 5-10: Comparison of raw and smoothed data for a set of $SC$ -surrogates using 6-level 50 % threshold DAUBLET4-denoise (T/CLT-80/1) to the found three major stratigraphic units (T/SON-1) 1 – alluvial sand, 2 – till, 3 – clay; Figure 5-5); $sRGB$ -colour space: $BI$ – brightness index, $SI$ – saturation index, $HI$ – hue index, $CI$ – colouration index, $HRGB$ – decorrelated hue, $IRGB$ – decorrelated light intensity, $SRGB$ – decorrelated saturation; $CIE_{xyY}$ -colour space: $x \cdot y$ – product of colorimetric values; $CIEL^*a^*b^*$ -colour space: $a^* \cdot b^*$ - product of red-green-ratio and blue-yellow-ratio, $L^*$ - luminosity, $\Delta E_{ab}^*$ - Euclidian distance between the colour values in this colour space; $CIEL^*c^*h^*$ -colour space: $c^*$ - chroma, $h^*$ - hue angle, $\Delta H_{ab}^*$ - Euclidian distance between the colour values in this colour space..... | 79 |
| Figure 5-11: Comparison of luminosity data from $CIEL^*a^*b^*$ -colour space from profiles T/CLT-80/1–5; light grey = raw data; black = using 6-level 50 % threshold HAAR-denoise to the found three major stratigraphic units (T/SON-1) 1 – alluvial sand, 2 – till, 3 – clay; Figure 5-5).<br>.....  | 80 |
| Figure 5-12: Comparison of luminosity data from $CIEL^*a^*b^*$ -colour space from profiles T/CLT-80/1–5; light grey = raw data; black = using 6-level 50 % threshold DAUBLET4-denoise to the found three major stratigraphic units (T/SON-1) 1 – alluvial sand, 2 – till, 3 – clay; Figure 5-5).<br>.....  | 80 |
| Figure 6-1: Results from $CPT$ (T/CPT-1) and $SS$ (T/SON-1); A) Dynamic pore water pressure $u_2$ , sleeve friction $f_s$ , corrected cone resistance $q_t$ , and friction ration $R_f$ (color coded to interpretation in B) and core results (green = silt, orange = dominantly sandy, white = core loss/no data); groundwater level in borehole at 8.48 m depth; B) colour coded lithological interpretation from ratio between corrected cone resistance $q_t$ and friction ratio $R_f$ according to ROBERTSON ET AL. (1986); 1 - sensitive fine grained, 2 - organic material, 3 - clay, 4 - silty clay to clay, 5 - clayey silt to silty clay, 6 - sandy silt to clayey silt, 7 - silty sand to sandy silt, 8 - sand to silty sand, 9 - sand, 10 - gravelly sand to sand, 11 - very stiff fine grained*, 12 - sand to clayey sand* [*over-consolidated or cemented]. .....  | 88 |
| Figure 6-2: Comparison smoothed $SC$ -data (luminosity $L^*$ ; chroma $c^*$ ) using 6-level 50 % threshold DAUBLET4-denoise (T/CLT-80/1) to grain size distribution and core photos results from $DT22$ (T/DT-1) for selected profile sections. ....   | 90 |

List of figures

---

Figure 6-3: Comparison of smoothed *SC*-surrogates using 6-level 50 % threshold DAUBLET4-denoise (T/CLT-80/1) to results from *CPT* (T/CPT-1) and *SS* (T/SON-1) (Figure 6-1);  $R_f$  – friction ratio; *sRGB*-colour space: *BI* – brightness index, *SI* – saturation index, *HI* – hue index, *CI* – colouration index, *HRGB* – decorrelated hue, *IRGB* – decorrelated light intensity, *SRGB*–decorrelated saturation; CIEL\**c\*h\**-colour space:  $L^*$  - luminosity,  $c^*$  - chroma,  $h^*$  - hue angle...  
 .....91

Figure 6-4: Comparison of volumetric water content  $\theta$  from *SMP*-data (T/SMP-1; T/SMP-2) and gravimetric water content  $\omega$  from *SS* (T/DT-2) (both from VIENKEN ET AL., 2013) to *SC*-surrogate luminosity  $L^*$  (CLT-80/6, raw data).....92

Figure 6-5: Mapped profile (layers, oxidative boundary) at Taucha test site obtained from joint interpretation of *CLT* and *DPEC*-data (supported by *CPT* and *SS*; Figure 6-3); plot is two times (2x) super-elevated.....92

Figure 0-1: Overall concept illustrating the linkage of the subprojects and project partners as well as the spatial scale covered by the proposed project (PAASCHE ET A., 2011). ..... 116

---

---

## List of tables

|   |     |
|---|-----|
| Table 1-1: Overview of applied geophysical methods and <i>DP</i> -profiling tools.....  | 8   |
| Table 2-1: Geological setting of the Löbnitz test site; layer thickness from local–regional scale (URL 5) including grain size classification (dominant: Boulder, cobble, Gravel, Sand, Silt, Clay, Organic; minor: bouldery, cobbly, gravelly, sandy, silty, clayey; fine, middle, coarse) according to DIN EN ISO14688-2, 2011(06); Holocene, PI-WG = Pleistocene—Weichselian glacial, MI – Miocene, OL – Oligocene, T-C – Tertiary—Cretaceous, Permian.  | 13  |
| Table 2-2: Geological setting of the Taucha test site; layer thickness from local–regional scale (URL 5) including grain size classification (dominant: Boulder, cobble, Gravel, Sand, Silt, Clay, Organic; minor: bouldery, cobbly, gravelly, sandy, silty, clayey; fine, middle, coarse) according to DIN EN ISO14688-2, 2011(06); Holocene, PI-SG = Pleistocene—Saalian glacial, MI = Miocene, T-C – Tertiary—Cretaceous, Permian.....   | 15  |
| Table 3-1: Geometrical parameters of applied geophysical methods for <i>ERT</i> (WENNER- $\alpha$ ), <i>GPR</i> , <i>RS</i> , and <i>MASW</i> , HAUSMANN, ET AL. (2013).....  | 26  |
| Table 3-2: Predefined start model parameter space for generic algorithm inversion with minimum and maximum S-wave velocities $v_s$ and layer thicknesses $H$ , respectively; density is fixed for all layers at 1.8 g/cm <sup>3</sup> , HAUSMANN, ET AL. (2013). .....  | 26  |
| Table 4-1: Geological setup at Löbnitz test site derived from <i>CPT</i> -log L/CPT-1(interpreted according to ROBERTSON ET AL. (1986) - Figure 4-15).....  | 55  |
| Table 5-1: Summary of applied formulas, key parameters, and citations for <i>SC</i> -surrogates; colour space indicated by letters A) CIEXYZ, B) CIE $xyY$ , C) CIE $L^*a^*b^*$ , D) CIE $L^*c^*h^*$ , E) <i>sRGB</i> , F) <i>RGB</i> .....   | 67  |
| Table 5-2: Regression coefficients $R$ and $R^2$ (bold) from multiple regression of denoised and resampled <i>SC</i> -surrogate values and indices for all profiles (T/CLT-80/1–5). Data was denoised using 6-level 50 % threshold DAUBLET4-wavelet and re-sampled to a constant vertical distance of 1 cm. <i>sRGB</i> -colour space: $BI$ – brightness index, $SI$ – saturation index, $HI$ – hue index, $CI$ – colouration index, $HRGB$ – decorrelated hue, $IRGB$ – decorrelated light intensity, $SRGB$ – decorrelated saturation; CIE $xyY$ -colour space: $x \cdot y$ – product of colorimetric values; CIE $L^*a^*b^*$ -colour space: $a^* \cdot b^*$ - product of red-green-ratio and blue-yellow-ratio, $L^*$ - luminosity; CIE $L^*c^*h^*$ -colour space: $c^*$ - chroma, $h^*$ - hue angle. $F$ = number of pairs with an $\alpha = 0.05$ ; $N = 1349$ . ..... | 77  |
| Table 6-1: Geological setup at Taucha test site derived from <i>CPT</i> -log T/CPT-1 (interpreted according to ROBERTSON ET AL. (1986) -Figure 5-7); *end of log. ....  | 88  |
| Table 0-1: Related affiliations in the <i>MuSaWa</i> -project and titles of the subprojects. ....   | 115 |

## List of tables

---

|   |     |
|---|-----|
| Table 0-1: Investigation depths of DP-measurements at the Löbnitz test site including ground water levels. .... | 117 |
| Table 0-2: Investigation depths of DP-measurements at the Taucha test site including ground water levels. ....  | 117 |

---

## List of symbols

---

| Symbol                           | Denotation   |
|----------------------------------|--|
| $a$                              | coefficient  |
| $a^*$                            | green-red ratio  |
| $B, b$                           | blue   |
| $b$                              | coefficient  |
| $b^*$                            | blue-yellow ratio                                      |
| $BI$                             | brightness index                                       |
| $b_j$                            | horizontal distance                                    |
| $c^*$                            | chroma   |
| $CI$                             | colouration index                                      |
| $d_{10}; d_{30}; d_{60}; d_{85}$ | diameter of the grains in the numbered quantile        |
| $e$                              | pore number  |
| $E$                              | Young's modulus  |
| $\Delta E_{ab}^*$                | Euclidian distance between $a^*$ and $b^*$             |
| $EC$                             | electrical conductivity                                |
| $f$                              | relative error   |
| $f_s$                            | sleeve friction  |
| $G, g$                           | green  |
| $g$                              | gravitational acceleration, const. 9.81 m/s            |
| $H$                              | layer thickness  |
| $h^*$                            | hue angle  |
| $\Delta H_{ab}^*$                | hue distance between $a^*$ and $b^*$                   |
| $HI$                             | hue index  |
| $H_{RGB}$                        | decorrelated hue                                       |
| $I$                              | current  |
| $I_{RGB}$                        | decorrelated intensity                                 |
| $K$                              | Bulk modulus   |
| $k$                              | coefficient  |
| $L^*$                            | luminosity   |
| $M$                              | P-wave modulus / transformation matrix                 |
| $n$                              | coefficient / pore percentage                          |
| $p$                              | number of interfaces                                   |
| $q_c$                            | measured cone resistance                               |
| $q_t$                            | corrected cone resistance                              |
| $Q1; Q2; Q3$                     | quantile   |
| $R, r$                           | red  |
| $R_f$                            | friction ratio   |
| $R(\lambda)$                     | reflectance factor                                     |
| $SI$                             | saturation index                                       |
| $S_{RGB}$                        | decorrelated saturation                                |
| $S(\lambda)$                     | transmission   |
| $t$                              | time   |
| $T$                              | temperature  |
| $T_0$                            | temperature minimum (298.15 K)                         |
| $T^{CWT}$                        | continuous wavelet transformation                      |
| $T^{DWT}$                        | discontinuous wavelet transformation                   |
| $u_2$                            | pore pressure measured at position 2 (behind the cone) |
| $v$                              | transformation matrix ( $rgb$ )                        |
| $V$                              | transformation matrix ( $RGB$ )                        |
| $\Delta V$                       | potential difference                                   |

---

continued on next page

## List of symbols

| Symbol                   | Denotation                  |
|--------------------------|-----------------------------|
| $v_p$                    | P-wave velocity             |
| $v_s$                    | S-wave velocity             |
| $x$                      | value                       |
| $x_j$                    | horizontal location         |
| $\tilde{x}$              | median                      |
| $X_{10}; x_{10}; X; X_0$ | colorimetric coordinates    |
| $\bar{x}(\lambda)$       | colour matching function    |
| $y$                      | depth                       |
| $Y_{10}; y_{10}; Y; Y_0$ | colorimetric coordinates    |
| $\bar{y}(\lambda)$       | colour matching function    |
| $z$                      | depth                       |
| $z_0$                    | average depth of interfaces |
| $\Delta z_j$             | vertical throw              |
| $Z_{10}; z_{10}; Z; Z$   | colorimetric coordinates    |
| $\bar{z}(\lambda)$       | colour matching function    |

## List of Greek symbols

| Symbol                  | Denotation  |
|-------------------------|---|
| $\alpha$                | coefficient   |
| $\gamma$                | unit weight / coefficient of gamma correction                       |
| $\gamma_s$              | solid weight  |
| $\gamma_0$              | empirical unit weight according to TEZCAN ET AL. (2006)             |
| $\gamma_p$              | unit weight calculated from $v_p$ according to TEZCAN ET AL. (2006) |
| $\epsilon_c$            | dielectric permittivity   |
| $\epsilon_s$            | dielectric number of the solid phase                                |
| $\epsilon_w$            | dielectric number of the aqueous phase                              |
| $\epsilon_a$            | dielectric number of the gas phase                                  |
| $\theta$                | volumetric water content / soil moisture                            |
| $\lambda$               | wave number/length  |
| $\mu$                   | shear modulus   |
| $\Pi$                   | Pi  |
| $\rho$                  | density   |
| $\rho_s$                | specific electrical resistivity                                     |
| $\sigma$                | Poisson's ratio / electric conductivity                             |
| $\varphi$               | father wavelet function   |
| $\phi$                  | porosity  |
| $\phi_\lambda(\lambda)$ | colour stimulus function  |
| $\psi$                  | mother wavelet function   |
| $\omega$                | gravimetric water content   |

## List of abbreviations

---

| <b>Abbreviation</b> | <b>Denotation</b>  |
|---------------------|--|
| <i>CPT/CPTU</i>     | <i>cone penetration testing</i>                            |
| <i>CLT</i>          | <i>colour logging tool</i>                                 |
| <i>DP</i>           | <i>direct push</i>   |
| <i>DPT</i>          | <i>direct push technologies</i>                            |
| <i>DT</i>           | <i>dual-tube coring</i>                                    |
| <i>DPEC</i>         | <i>direct push electrical conductivity logging</i>         |
| <i>EG</i>           | <i>engineering geophysics</i>                              |
| <i>EM</i>           | <i>electromagnetic waves</i>                               |
| <i>ERT</i>          | <i>electrical resistivity tomography</i>                   |
| <i>GPR</i>          | <i>ground penetrating radar</i>                            |
| <i>L</i>            | <i>Löbnitz</i>   |
| <i>LIF</i>          | <i>laser-induced fluorescence</i>                          |
| <i>MASW</i>         | <i>multichannel analysis of surface waves</i>              |
| <i>NSG</i>          | <i>near surface geophysics</i>                             |
| <i>PSO</i>          | <i>particle swarm optimisation</i>                         |
| <i>RS</i>           | <i>refraction seismic</i>                                  |
| <i>SC</i>           | <i>soil colour</i>   |
| <i>SeismicCPT</i>   | <i>cone penetration testing including seismic receiver</i> |
| <i>SMP</i>          | <i>soil moisture probe</i>                                 |
| <i>SONIC/SON</i>    | <i>sonic drilling</i>                                      |
| <i>SS</i>           | <i>soil sampling</i>                                       |
| <i>STT</i>          | <i>seismic travelttime tomography</i>                      |
| <i>T</i>            | <i>Taucha</i>  |
| <i>VSP</i>          | <i>vertical seismic profiling</i>                          |
| <i>VisCPT</i>       | <i>visible cone penetrometer</i>                           |
| <i>WT</i>           | <i>wavelet transformation</i>                              |

---

---

---

“The truth is a curve.”

Terry Prachett

---

# 1 Introduction

## 1.1 Scope

*Engineering geology* is a complex and wide-ranging interdisciplinary science that describes both unconsolidated and solid rocks (either individually or in terms of their ground-mass). This science helps us to understand genetically-determined material properties with regard to their geological development, with the aim of developing a holistic approach to solving both engineering and environmental problems (PRINZ UND STRAUß, 2006). Investigations must therefore provide explanations about the subsurface – in particular, concerning the impact on constructions – and how it affects the nature of a site and condition of the nearby soil, bedrock, and groundwater (DACHROTH, 2002). Measurement-specific geotechnical site exploration can help reduce geological risk. Survey results moreover can help minimize the impact of any uncertainties relating to the subsurface and allow site-users to make more informed site usage decisions – helping to avoid unnecessary costs, preventing structural damage, and achieving a preferable/optimal economic solution (DACHROTH, 2002).

Thus, knowledge of the spatial distribution of geotechnical parameters in the near surface is essential for a thorough assessment of construction sites, e.g., for large building sites. According to the specific geotechnical issue to be addressed, different traditional geotechnical surveying and analysis tools are typically used at selected locations. However, the high spatial heterogeneity of near-surface unconsolidated sediments is usually not reliably captured by sparse geotechnical measurements. Hence, additional geophysical explorations are carried out. Thus, auxiliary geophysical methods and appropriate tomographic reconstruction techniques provide data and models, e.g., seismic velocities that describe the distribution of physical parameters of the ground at different scales in one, two, and three dimensions.

The investigation scale (distance between exploration sites) depends on geological conditions, constructional scope, and structural issues. Thus, geotechnical categories define the investigation. For example, DIN 4022 (German standard for geotechnical site investigation) defines the specific scales used for building and industrial constructions, large-scale or elongated constructions, and location lines (according to prior knowledge of the terrain and subsurface conditions) as being 20–40 m, 50 m, and 50–200 m, respectively.

The minimal investigation depth amounts to 4–6 m starting from the bottom of the foundation or excavation floor (depending on the nature of the construction). By definition, the ground (subsoil where construction takes place) is the part of the subsurface where a construction is founded, or which is influenced and stressed by constructions measures. In

this respect, we can distinguish between natural ground (including bedrock), bottom-up soils, masses, or fillings.

The nature of the ground can be described by clearly confined homogeneous sections (composed of similar mineral content) that can be furthermore distinguished by thickness and distribution. Specific soil and rock physical properties characterise the aforementioned homogeneous sections or layers. Four major groups classify these categories, including a properties subset, e.g., PRINZ AND STRAUß (2006):

- (1) soil type: grain size, grain distribution, liquid limit, plastic limit, shrinkage limit, plasticity index, water absorptive capacity, lime content, organic or other constituents, clay mineralogy
- (2) status: water content, density, porosity, bulk density, stiffness
- (3) behaviour under mechanical stress:
  - plasticity, compressive strength, tensile strength, brittleness, shear strength
- (4) behaviour under hydraulic stress

The laboratory techniques used to gather the relevant soil properties for soil type classification, e.g., sieve analysis, are *state-of-the-art*. Field measurements support this data, helping to assign this information to homogeneous sections of the ground (layers). Data interpretation however becomes challenging because actual field conditions (*in situ*) differ from those appropriated in the laboratory. Moreover, results from geotechnical site investigation are site-specific. Thus, the impact of changing conditions at the field scale, e.g., oscillating ground water levels, must also be considered.

In *engineering geology*, the joint acquisition and joint interpretation of data has become a central issue. Nowadays, geotechnical engineers use interdisciplinary methods to describe the ground. Indirect exploration methods (field mapping, analysis of aerial photos, geochemical monitoring of gases, geophysical methods) initially help with large-scale characterisation of the ground. In contrast, direct exploration methods (soil sampling of different quality classes, test pittings, investigation galleries, drillings, field investigations, e.g., by *direct push technologies – DPT*) deliver pointwise, rapid, efficient, and reliable data. These sample and lithological logs (and the determination of groundwater conditions) allow site characterisation according to soil and rock types. Subsequently, well logging (borehole probing, water sampling, inclination measurements, geophysical logging, etc.) provides additional information which can also be used for monitoring. *Engineering geophysics (EG)* enhances the spectrum of available site information by recording parameters of particular physical properties which are related to lithology. Thus, a general concept for site investigation is required integrating the aforementioned methods and techniques (Figure 1-1). Accordingly,

geotechnical site investigation provides information, which can be used to verify the safety of construction sites and various terrains (distribution of bearing pressure, proof of bearing capacity, structural safety, etc.). Thus, this methodology is consequently applied to ensure safe construction practices and remediation or prevention of any hazards (e.g., for ground settlements due to increased load).

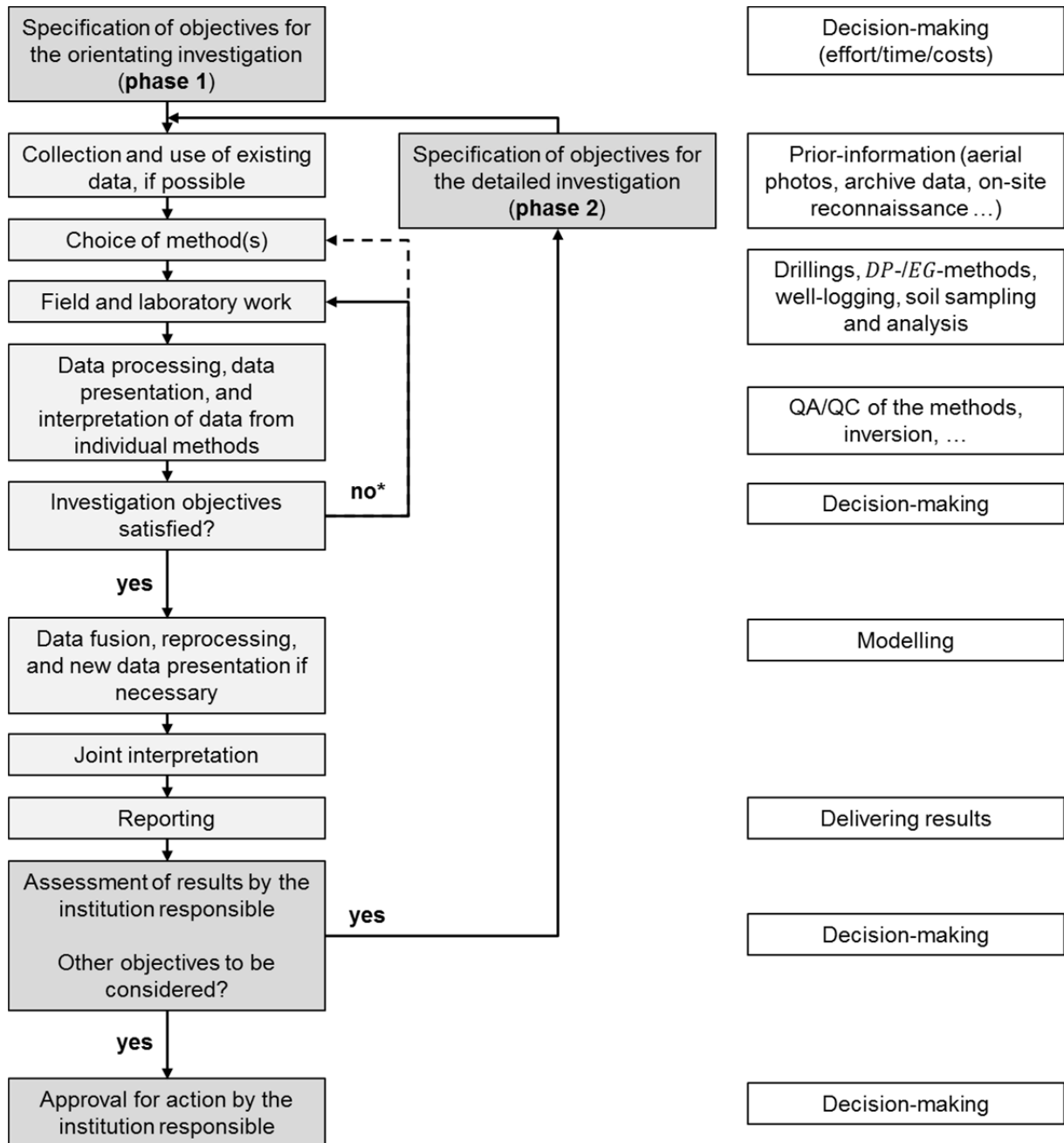


Figure 1-1: Flow chart for two-phase site investigation adopted from KNÖDEL ET AL. (2007), supplemented by exemplary actions (right column); \* DP-methods allow on-site decision-making.

The past few decades have seen the rapid development of *EG* and *DPT*, addressing parameter characterisation for geotechnical site investigation (→ Chapter 1.2 and 1.3). Thus, according to the general trend of interdisciplinary application of direct and indirect exploration of the near surface, this thesis focuses on a joint application and further development of such technologies and data processing.

Consequently, we tested this integrated site investigation approach at selected test sites. This helps to expose unconsolidated sediments, which represent typical construction grounds in Central Germany. At the (a) Löbnitz test site, alluvial sediments are present (silt, sand, gravel); at the (b) Taucha test site, examples of alluvial–glacial sediments (sand, silt, till), and Miocene clay could be found.

At test site (a), intensive fieldwork was conducted such as a multi-method geophysical investigation including *ground penetrating radar (GPR)*, *electrical resistivity tomography (ERT)*, *refraction seismic (RS)*, and *multichannel analysis of surface waves (MASW)* (methods that have been proven to deliver valuable information) and, furthermore, application of *DPT*. The structural information obtained from this survey is useful for interpretation of results from newly developed mobile *DP*-based *seismic travelttime tomography (STT)*, additionally tested at the Löbnitz test site. Here, structural information about the near surface is not only of great interest for explaining geomorphological evolution but also for geotechnical site assessment. At the study site, we assume a subsurface hydraulic connection caused by cut-off oxbows that cross a dike structure beneath ground level. This allows a base flow in both the direction of the river and the land along those channel structures, which is controlled by stream gauge fluctuations and ground water level. Therefore, these subsurface streams along the abandoned channel structure have a severe impact on the protection capacity of the dike in the case of a flood event.

At test site (b), we found a tripartite layer structure (sand, till, clay) that provides excellent conditions for testing the *colour logging tool (CLT)* as a new approach for site characterisation e.g., for oxidative conditions in the vadose zone. This data (from repeated measurements) is compared with data obtained from other *DPT*, such as *cone penetration testing (CPT)*, *electrical conductivity logging (DPEC)*, *soil moisture probing (SMP)*, and *soil sampling (SS)*. The *CLT* shows great potential for: (1) enlarging the spectrum of classical soil colour measurement methods and therefore (2) delivering extra information for geotechnical engineering purposes in an unconsolidated rock environment. This proxy is applicable for soil classification, while being directly associated with the vertical distribution of lithological properties such as differing grain sizes, an indication of oxidative or reductive conditions, or micro-stratification. Hence, a need exists to develop an appropriate data processing method, following the idea of downscaling (smooth) high-resolution data, so that resultant interpretation certainty increases.

This thesis applies a number of methods from *EG* and *DPT* tackling issues such as:

- How does a combination and joint interpretation of *state-of-the-art EG*-methods help to increase qualitative interpretation of subsurface features?
- How does geotechnical site characterisation benefit from *DP*-based joint acquisition of P- and S-waves (seismic traveltime tomography – *STT*)?
- Do *in situ*-obtained soil colours provide additional information for geotechnical site characterisation?

The application and technical developments of *EG* and *DPT* in this thesis used for *in situ* prediction of geotechnical parameters for geotechnical site investigation, encourage the reliable characterisation of the near-surface ground, especially for appraising information uncertainty which remains a challenge for achieving objective geotechnical risk analysis. Any disadvantages of a single method can be compensated for by using a combined interpretation. Thus, we expect a significant positive impact for near-surface imaging.

This thesis was prepared within the framework of the MUSAWA-project (2011–2013) – *Multi-scale S-wave tomography for exploration and risk assessment of development sites* (PAASCHE ET AL., 2011, 2013; APPENDIX A).

## 1.2 Engineering geophysics for site characterisation

*Engineering geophysics (EG)* can be described as being: “*The application of geophysical methods to the investigation of subsurface materials and structures which are likely to have (significant) engineering implications*” (REYNOLDS, 1997). In general, *EG* are the part of *applied geophysics* that covers everything investigated (usually to an investigation depth of less than 100 m), such as determination of crustal thickness, studies of shallow structures (engineering site investigation, groundwater–mineral–resource exploration), location of mine shafts or other buried cavities, pipes and cables, mapping archaeological remains (REYNOLDS, 1997). Thus, geophysical methods are used to develop a model of the geology below the site detecting, locating, and delineating anomalies such as fracture zones, groundwater, landfills, contamination plumes, and furthermore, obtaining information on lithology and physical parameters of the ground (KNÖDEL ET AL., 2007).

The geophysical methods used for surface investigations (so-called *near surface geophysics – NSG*) are based on tracing boundaries (contrasts) of particular physical properties. The main requirement is that the ground is not too complex and, furthermore, that the homogeneous sections (layers) differ considerably in those geophysical properties (e.g., KNÖDEL ET AL., 2007). In this process, density is the most important parameter (others are magnetisation, susceptibility, electrical resistivity, and seismic velocities). Groundwater also exerts sig-

nificant influence upon the surveys. Hence, the parameter values to be expected at the site must be considered before conducting a geophysical survey (KNÖDEL ET AL., 1997, 2007; REYNOLDS, 1997). Geophysical methods have the important advantage of enabling ground characterisation (linearly or raster-like, one-two-three-dimensional) with relatively little effort. In general, non-invasive surface-based and invasive borehole-based investigations, e.g., crosshole tomography, subdivide the geophysical methodological spectrum in two major application families. The general tendency in the application of *EG* is usually to combine several different commonly-used approaches - mostly seismic, geoelectric, and electromagnetic methods, such as *refraction seismic (RS)*, geoelectric D.C. methods (e.g., *electrical resistivity tomography – ERT*), and *ground penetrating radar (GPR)*; considering the parameters to be expected (see above). To date, geotechnical engineers notably use other high-sensitivity geophysical methods (gravimetry, radiometry, geothermal investigations, etc.) and, in particular, tomographic methods (seismic, electromagnetic, etc.) only for specific problems (PRINZ AND STRAUß, 2006). This is because of the requirement for experience in analysis and evaluation of the obtained data. In particular, seismic surface wave methods (e.g., *multichannel analysis of surface waves*) are, nowadays, a relatively new tool used for geotechnical site investigation. However, these seismic methods provide information about elastic behaviour (ratio between density and P-/S-wave velocity), which is of great importance in geotechnical engineering, e.g. TURESSON (2007). Besides surface methods, tomographic approaches are of great interest because they allow us to decrease uncertainties caused by depth inversion, e.g., ANGIONI ET AL. (2003), GRANDJEAN ET AL. (2012), LINDER ET AL. (2010) and DIETRICH AND TRONICKE (2009). For detailed information on applied (near-surface, engineering, and hydro) geophysics, the reader is referred to widely available relevant literature, such as, e.g., BURGER ET AL. (2006), BUTLER D.K. (2005), KNÖDEL ET AL., (1997, 2007), MILTITZER AND WEBER (1987), REYNOLDS (1997), RUBIN AND MARINO (1979), TELFORD ET AL., (1990), and WERBAN AND DIETRICH (2008). Table 1-1 lists all *EG*-methods used in this thesis.

### 1.3 Direct push technologies for site characterisation

The US Environmental Protection Agency EPA defines the *DPT* as part a growing family of tools used for performing subsurface investigations by driving, pushing, and/or vibrating small-diameter hollow steel rods into the ground (EPA, 1997). Attaching multiple tools at the end of the rod allows for soil, soil-gas, and groundwater sampling. Furthermore, for continuous or discontinuous measurement of subsurface properties sensor probes or tools are also attachable that provide *in situ* high-resolution data, such as electrical, dielectrical, textural, and hydraulic properties, as well as soil colours or contaminant distribution. Moreover, a set of parameters can be derived that is related to these *in situ* measurements.

In general, *DPT* are a very promising because of their minimally-invasive nature and high-resolution data measured by a broad variety of available sensors and probes. The most common application is the recording of vertical profiles (DIETRICH AND LEVEN, 2006). Considering small-scale variability, experience of using *DPT*-applications has shown that measured, sampled, and logged data are reproducible (LEVEN ET AL., 2010). Here, *in situ*-measured data provides many advantages over common drilling methods, due to avoidance of compaction or contamination effects during soil removal. This supplements the existing general advantages of *DPT* – namely speed of measurement, time/cost effectiveness, field site accessibility, and on-site decision-making. *DPT* are most applicable in unconsolidated sediments that are typically less than 30 m below the ground surface (EPA, 1997). However, sediment properties, e.g., grain size and stiffness, generally limit depth. Therefore, absolute operational depth may differ depending to on-site conditions. Several attachable tools and probes allow for logging of geophysical, geotechnical, hydrological and geochemical data (DIETRICH AND LEVEN, 2006). Moreover, the *DPT* can also be used for temporary installation of boreholes such as groundwater or soil gas monitoring wells. Latest developments combine several common tools to multi-parameter probes. In recent years, the amount of literature on *DPT* has increased, such as EPA (1997, 2005), BUTLER J.J. (2005), MCCALL ET AL. (2005), DIETRICH AND LEVEN (2006), LEVEN ET AL. (2010, 2011), and KÄSTNER ET AL. (2012). Table 1-1 lists all *DPT* used in this thesis.

Without a doubt, investigative drillings and *DPT* (direct exploration methods applicable in unconsolidated sediments) help to supplement (or create) geophysical data sets and increase interpretation certainty for geotechnical site characterisation. HOFFMANN ET AL. (2008) used shear wave seismic and *DP*-methods for investigation of an urban aquifer. GRANDJEAN ET AL. (2012) investigated a landslide using a combination of P-wave seismic and *CPT*. PAASCHE ET AL. (2009) used *DPT* (contained the seismic source) and surface-planted geophones for near-surface *STT*. SCHMELZBACH ET AL. (2011) combined *GPR*-images with one-dimensional *in situ* physical-property estimates from *DP*-logging for three-dimensional modelling of hydrostratigraphic conditions.

The *DPT*-methods are especially promising for future investigations, owing to the broad variety of available sensors and probes, their minimally invasive nature, and the high-resolution data they provide (geophysical, geotechnical, hydrological, geochemical). In this context, we recognise *in situ*-obtained soil colour as a promising proxy for (geotechnical) site characterisation (→ Chapter 5).

Table 1-1: Overview of applied geophysical methods and *DP*-profiling tools.

| <b>Method</b>   | <b>Detected Parameter</b>   | <b>Information Content</b>                               | <b>Modus</b>                    | <b>Reference (e.g.)</b>   |
|---|---|--|---------------------------------|---|
| <i>electrical resistivity tomography (ERT)</i>                            | electric resistivity / conductivity                               | lithology, structure                                     | continuous                      | HOFFMANN AND DIETRICH (2004), REIN ET AL. (2004), SCHROTT AND SASS (2008)   |
| <i>ground penetrating radar (GPR)</i>                                     | dielectric properties   | water content, porosity, permeability, structure         | continuous                      | KNIGHT (2001), NEAL (2004), SLOB ET AL. (2010), VAN DAM (2012)  |
| <i>refraction seismic (RS)</i>  | velocity  | structure, elastic behaviour                             | continuous                      | KNÖDEL ET AL. (1997, 2007), MILTITZER AND WEBER (1987)  |
| <i>multichannel analysis of surface waves (MASW)</i>                      | velocity  | structure, elastic behaviour                             | continuous                      | PARK ET AL. (1999, 2007), LOU ET AL. (2009), SOCCO AND STROBBIA (2004) XIA ET AL. (2000)  |
| <i>seismic traveltime tomography (STT)</i>                                | velocity  | structure, elastic behaviour                             | discontinuous                   | KNÖDEL ET AL. (1997, 2007), LEHMANN (2007)  |
| <i>electrical conductivity logging (DPEC)</i>                             | electrical conductivity (soil)                                    | variation of soil types                                  | continuous / high               | CAMPANELLA AND WEEMES (1990), CHRISTY ET AL. (1994), BECK ET AL. (2000), BUTLER ET AL. (1999), EPA (1997), HARRINGTON AND HENDRY (2006), SCHULMEISTER ET AL. (2003, 2004), SELLWOOD ET AL. (2005), ZSCHORNACK AND LEVEN-PFISTER (2012A) |
| <i>cone penetron testing (CPT)</i>  | cone resistance, sleeve friction, pore water pressure             | soil type, variation of bulk density and stiffness       | continuous / medium (push only) | BROUWER (2007), DOUGLAS AND OLSEN (1981), EPA (1997), JEFFERIES AND DAVIES (1991), LUNNE ET AL. (1997); MEIGH (1987), ROBERTSON ET AL. (1983, 1986), ROBERTSON (1990, 2009), SCHMERTMANN (1978)   |
| <i>soil moisture probing (SMP)</i>  | electrical conductivity (soil), relative dielectric number (soil) | variation of soil types, water content                   | continuous / medium (push only) | EVETT ET AL. (2006), HILHORST (2000), KIM ET AL. (2007) SHINN ET AL. (1998)   |
| <i>soil sampling – SS (sonic Drilling – SONIC, dual-tube coring – DT)</i> | soil sample   | soil type (any related analysis)                         | quasi-continuous / high         | EPA (1997, 2005), DIETRICH AND LEVEN (2006), LEVEN ET AL. (2011), MCCALL ET AL. (2005), ZSCHORNACK AND LEVEN-PFISTER (2012B)  |
| <i>colour logging tool (CLT)</i>  | colour data   | stratigraphic information, oxidation indicator, moisture | continuous / medium             | this thesis, HAUSMANN ET AL. (SUBMITTED)  |

## 1.4 Outline

Chapter 1 introduced the scope of the thesis and the research questions presented, plus also provided a general description and outline of the fundamental literature relevant to the applied methods from *engineering geophysics (EG)* (→ Chapter 1.2) and *direct push technologies (DPT)* (→ Chapter 1.3). Detailed description of the single applications is provided in the method sections of the following chapters.

We performed intensive fieldwork at two test sites (Löbnitz and Taucha), which represent typical construction grounds in Central Germany. Chapter 2 describes their location and geological setup.

The application part of the thesis has been organised in the following way:

Chapter 3 describes the combined application of geophysical methods (*electrical resistivity tomography – ERT*, *ground penetrating radar – GPR*, *refraction seismic – RS*, and *multichannel analysis of surface waves – MASW*) and core samples which are used for investigating the subsurface structures at the Löbnitz test site based on published work (HAUSMANN ET AL, 2013). We discuss the advantages of a multi-method approach and how this improves the reliability of data interpretation. This was tested to image the subsurface features of an abandoned meander. The chapter concludes by discussing the advantages of joint interpretation of a set of geophysical methods (validated by core samples) for site investigation. These results provide detailed information about the subsurface structures, which was used for interpretation of results from *seismic traveltime tomography (STT)*.

Chapter 4 begins by describing the experimental design of a mobile *DP*-based *seismic traveltime tomography* device tested at the Löbnitz test site. This novel experimental design allows simultaneous acquisition and recording of P- and S-waves. The constructed velocity pattern from the recorded P- and S-waves using *particle swarm optimisation (PSO)* delivers reliable data for geotechnical site characterisation. This also allows an uncertainty appraisal of such data. *DP*-probing tools (such as *cone penetration testing – CPT* and soil sampling – *SS*) validate the geophysical results. Thus, the results provide detailed information about geotechnical properties of the subsurface structures at the Löbnitz test site. Comparing *DP*-based *in situ* data (*CPT*) to the cross sections gathered from *STT*, highlights the high potential of such techniques for high-resolution geotechnical parameterisation at the local-scale. In this context, we recognise *in situ*-obtained soil colour (gathered with the *DP*-based *colour logging tool – CTT*) as a promising proxy for (geotechnical) site characterisation.

Chapter 5 presents a new methodology for *DP*-based *in situ* soil colour detection and processing of such data for rapid, precise, and in-depth characterisation of the near surface. This chapter begins with a description of colour measurements, showing that the rapid and

high-resolution *DP*-based *in situ* colorimeter fills the gap between classical soil sampling and *ex situ* colour determination using colour charts, handheld colorimeter, and laboratory methods. Then, we describe the numerical transformation of *in situ*-obtained soil colours into colour surrogates for selected colour spaces. This new approach allows data analysis of such data. Observing high data variability, the chapter discusses the application of *wavelet transformation* and *cluster algorithms* as data denoising strategies, with regard to increasing interpretation certainty of colour log data. Thus, the results of this chapter deliver a processing technique for *in situ*-obtained soil colours.

Chapter 6 presents results from joint interpretation of *in situ*-obtained soil colour data and *state-of-the-art* geotechnical *DP*-based profiling tools, discussing the additional benefit of such data for geotechnical site characterisation of the near surface. The chapter partly deals with a comparison of colour data to *CPT*, *SS*, *soil moisture probing (SMP)*, and *electrical conductivity logging (DPEC)*, showing that this data provides additional information on small-scale lithological changes, chemical states (oxidative/reductive conditions), soil moisture, and allows enhanced profiling.

Chapter 7 presents a summary and final conclusion.

## 2 Field sites

### *Chapter Outline*

*This chapter describes the location and the geological setup of the selected test sites (Löbnitz and Taucha) representing typical construction grounds in Central Germany.*

### 2.1 The Löbnitz test site

For our investigation, we pre-selected an abandoned meander oxbow structure, which we chose using aerial imaging and on-site reconnaissance. The abandoned meander is located in the northern Saxony, Germany, close to the village of Löbnitz (Figure 2-1A). The entire length of the River Mulde is characterised by a vast number of meanders and their typical point bar and cut bank dynamic (Figure 2-1B). Due to embankment creation during the 1970's, many of these have now been abandoned. Nowadays, intensive agriculture operations use the former floodplain area.

Rhyolites (pyroxene–quartz porphyry) of the Lower to Middle Permian (Rotliegend, Northwest Saxony Eruptive Complex) form the geological basement (PÄLCHEN AND WALTER, 2008). The lowest layer of the Tertiary complex is the Rupel Clay (Lower Oligocene), which is composed of clay and silt. The overlying Bitterfeld Mica Sand (middle to fine sands) refers to the transition of Oligocene to Miocene stage. The upper layers are part of the Vetschau Formation (Vetschau Member of the Miocene stage) composed of clay, silt, and sand. In this formation, the main lignite coal seams (e.g., Bitterfelder Oberbank) are developed. The quaternary package covers these marine–continental sediments.

The valley of the River Mulde was recently formed in the lower gravel terrace, which originates from the end of the Weichselian glacial period and began to meander later on. The subsurface is therefore composed of Holocene haugh (alluvial clayey and loamy material), which overlays fluvial gravelly sands, changing sand, and the gravel layers of the lower terrace (Weichselian glacial), e.g., KATER AND KOCH (2007). Since the active meander is cut off from the river's course, dead meanders were created and developed limnic conditions that lead to the accumulation of organic matter and the generation of peaty sediments in the abandoned channels. Finally, shifted masses of alluvial clay and fluvial sands filled the structure as an embankment was constructed. Table 2-1 provides general information about the site's geology.

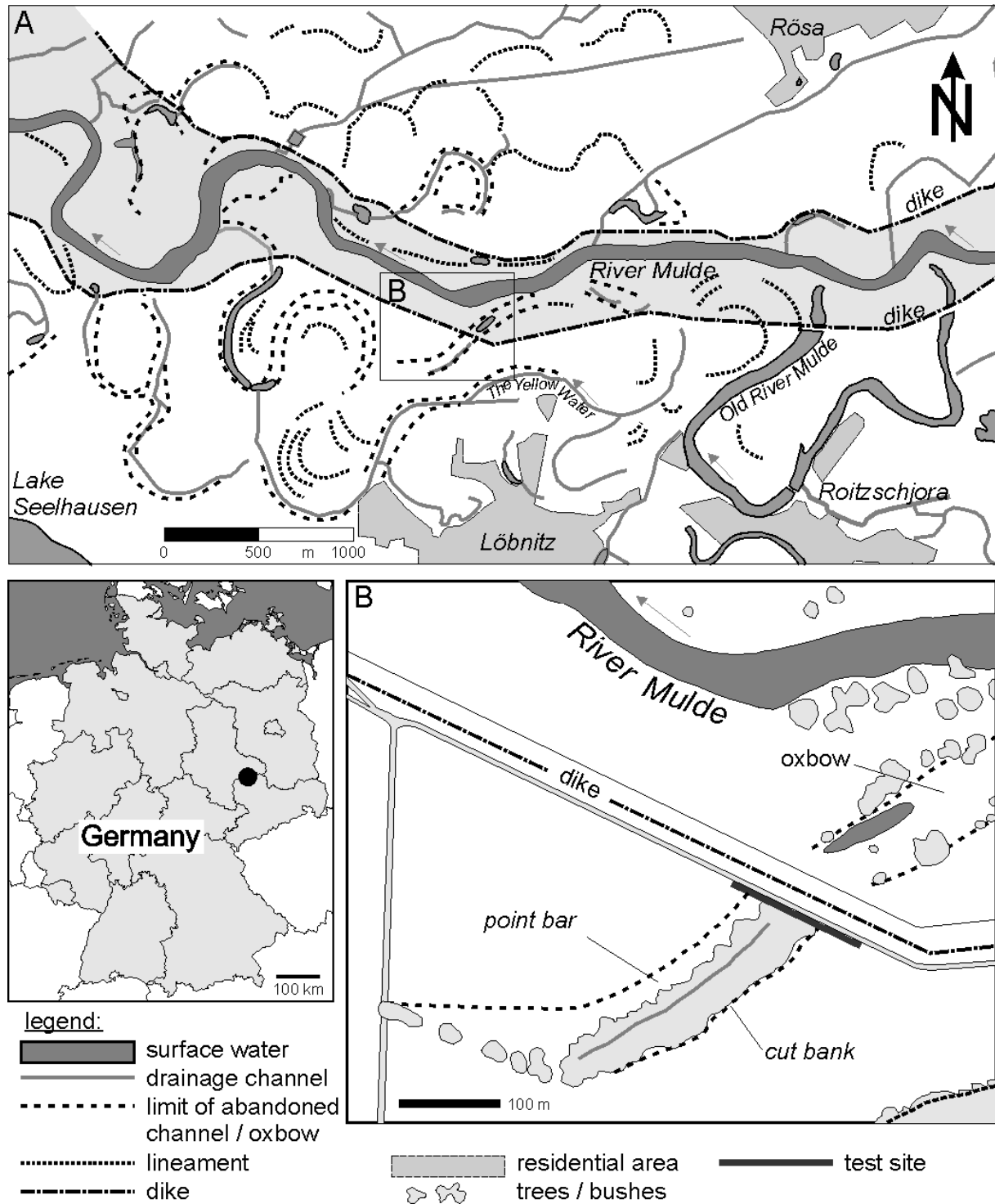


Figure 2-1: A) Recent Mulde valley close to Löbnitz in northern Saxony (Germany); composition of surface waters, drainage channels, and indications of abandoned river channels condensed from aerial photos; B) Detailed section with the test site location (recorded profile), which follows the dike path by crossing an oxbow structure (HAUSMANN ET AL., 2013; modified).

Table 2-1: Geological setting of the Löbnitz test site; layer thickness from local–regional scale (URL 5) including grain size classification (dominant: Boulder, cobble, Gravel, Sand, Silt, Clay, Organic; minor: bouldery, cobbly, gravelly, sandy, silty, clayey; fine, middle, coarse) according to DIN EN ISO14688-2 (2011/06); Holocene, PI-WG = Pleistocene—Weichselian glacial, MI – Miocene, OL – Oligocene, T-C – Tertiary—Cretaceous, Permian.

|     | <b>Stratigraphic Unit</b>  | <b>Classification</b>                   | <b>Thickness [m]</b>        |
|-----|--|---|-----------------------------|
| (1) | topsoil (H)  | saclSi                                  | 0 – 0.3                     |
| (2) | alluvial sediments (younger haugh) (H)   | fsa*msclSigr'or' –<br>cl*fsaSigr'or'    | 0.3 - 3                     |
| (3) | alluvial haugh gravels (H)   | fsaMSagr' –<br>msa*FSacl' –<br>gr*Sacl' | 2 – 9                       |
| (4) | lover bench gravel (PI-WG)   | sa*Gr [csa*CGr-MGr-<br>FGmsa]           | 0 – 4                       |
| (5) | Bitterfeld Seam Complex [Vetschau Member, including lignite coal seams: Bitterfelder Oberbank 1, Bitterfelder Unterbank] | Cl,Si,Sa,Or                             | approx. 40<br>(alternating) |
| (6) | sand [Bitterfeld Mica Sand] (MI-OL)  | fsaMSa - FSa                            | approx. 30<br>(alternating) |
| (7) | Rupel Clay (OL)  | si*Cl – cl*Si                           | < 14 (alternating)          |
| (8) | kaloninitic clay (T-C)   | saCl                                    | > 1                         |
| (9) | rhyolites (P)  | bedrock                                 | > 100                       |

## 2.2 The Taucha test site

For our second test site, we selected an active clay and gravel pit. This is located in northern Saxony, Germany, close to the city of Taucha (Figure 2-2). Here, local mine operators extract marine clay and alluvial deposits for construction material production.

Rhyolites (pyroxene-quartz porphyry) of the Lower to Middle Permian (Rotliegend, Northwest Saxony Eruptive Complex) form the geological basement (PÄLCHEN AND WALTER, 2008). The crystalline bedrock outcrops linearly close to the surface and forms hill and basin structures. The basins are filled with tertiary sediments of the Miocene stage mainly composed of clay with small interbedded silt and sand layers. The tertiary basin opens to the north, which implies increased layer thickness and the occurrence of lignite coal seams. These marine-continental sediments are covered by a quaternary package. This is mainly composed of alluvial sand to gravel and till deposits from Saale glaciation. The sediments are deposited stepwise at the edges of the former glacier in an end moraine facies. A mixed layer structure of inserted alluvial sands in till deposits can be observed. Hence, these deposits are not uniformly layered. The deformed sediments may vary in thickness - even at the local scale - because of clinching, squeezing, and pushing processes during the accumulation of the tills at the former crystalline hill barrier and the braided water flow, which deposited coarse alluvial fans of highly unsorted sediments. We kindly refer the reader to BECKER (2010) for more detailed information, who further investigated the local geology as part of the framework of this thesis.

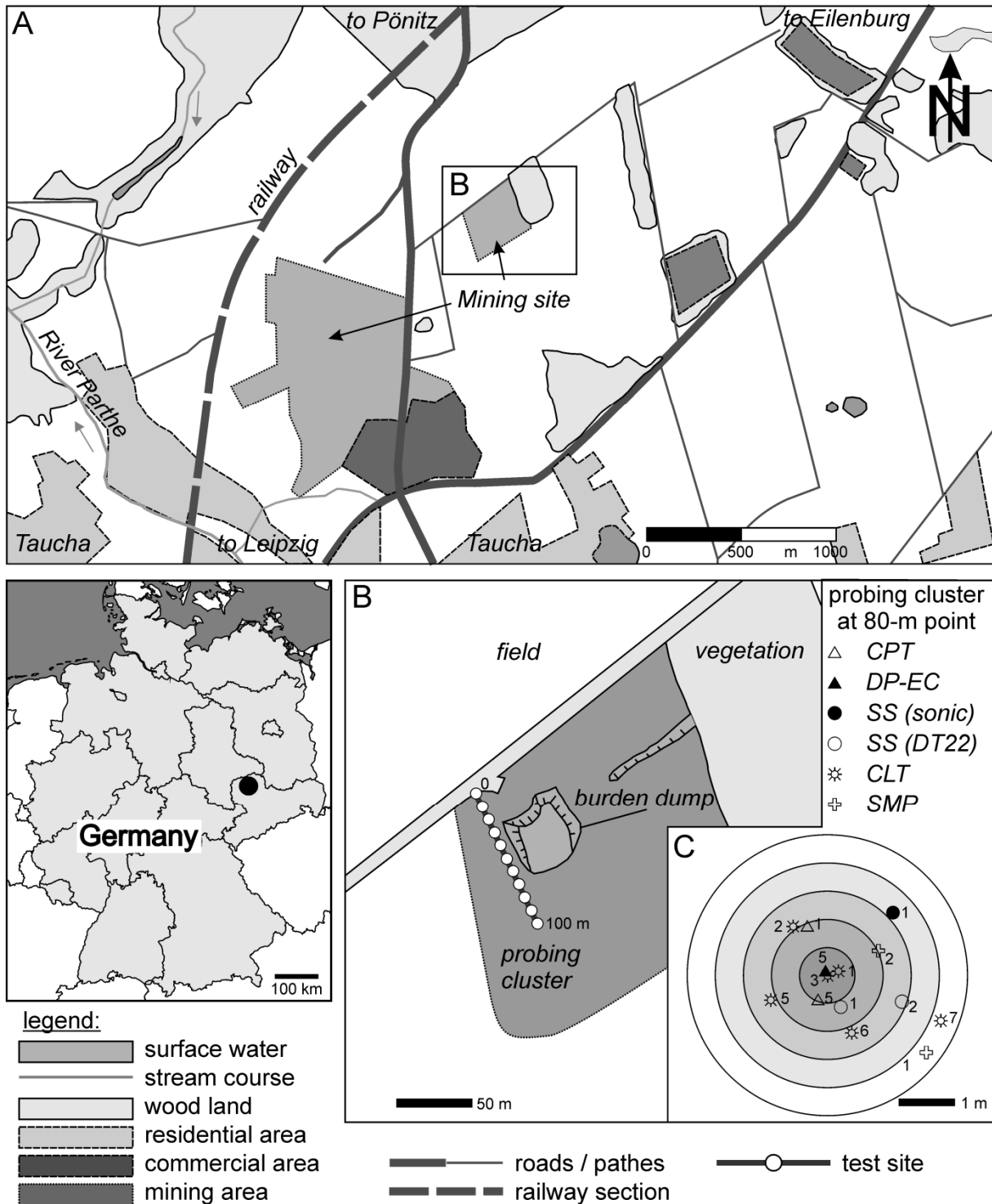


Figure 2-2: A) Location of the mining area close to Taucha in northern Saxony (Germany) condensed from aerial photos; B) Detailed section of the test site location (recorded probing cluster), which is located in a sand pit; C) Probing cluster at 80-m position along the profile with locations of the applied DP-probings (→ Chapter 4, Appendix B).

We conducted intensive fieldwork in a local sand pit (Figure 2-2B), which is part of a small hill dipping slightly to the north. The local geological setting can be described as a quaternary top layer (alluvial sand - I) over glacial till (II) over tertiary marine clay (III),- involving the layers (2), (5), and (8) presented in Table 2-2.

Table 2-2: Geological setting of the Taucha test site; layer thickness from local–regional scale (URL 5) including grain size classification (dominant: Boulder, cobble, Gravel, Sand, Silt, Clay, Organic; minor: bouldery, cobbly, gravelly, sandy, silty, clayey; fine, middle, coarse) according to DIN EN ISO14688-2 (2011/06); Holocene, PI-SG = Pleistocene—Saalian glacial, MI = Miocene, T-C – Tertiary—Cretaceous, Permin.

|      | <b>Stratigraphic Unit</b>                       | <b>Classification</b> | <b>Thickness [m]</b> |
|------|---|-----------------------|----------------------|
| (1)  | topsoil (H)                                     | saclSi                | 0 – 0.3              |
| (2)  | upper alluvial sand (PI-SG)                     | fgr-cgrFSa-MSa        | < 10                 |
| (3)  | upper till [Leipzig phase] (PI-SG)              | clsagrcoSi (bo)       | 0 – 6                |
| (4)  | lower alluvial sand [Bruckdorf Horizon] (PI-SG) | msaFSa - fsaMSafgr    | < 10                 |
| (5)  | lower till [Zeitz phase] (PI-SG)                | clsagrSico (bo)       | < 8                  |
| (6)  | Main Terrace Complex – River Mulde (PI-SG)      | saGr                  | < 13                 |
| (7)  | sand (MI)                                       | clsiFSa               | < 4                  |
| (8)  | clay [Deckton beds] (MI)                        | Cl                    | < 27                 |
| (9)  | Bitterfeld Seam Complex                         | Cl,Si,Sa,Or           | approx. 50           |
| (10) | kaloninitic clay (T-C)                          | saCl                  | > 1                  |
| (11) | rhyolites (P)                                   | bedrock               | > 100                |



## 3 Combined geophysical methods for structural site characterisation

### Chapter Outline

*This chapter describes the combined application of geophysical methods and core samples investigating the subsurface structures at the Löbnitz test site basing on published work (HAUSMANN ET AL., 2013). The chapter follows this text as a modified author's version fully acknowledged to all co-authors, adjusted to BE, and expanded in the method section. The chapter highlights are:*

- *The ERT, GPR, RS, and, MASW identify subsurface features of an abandoned meander.*
- *The multi-method approach improves the reliability of data interpretation.*
- *The MASW delivers best structural information.*
- *Core samples are indispensable for validation of geophysical results.*

*However, the method section was enlarged providing more information on the state-of-the-art of the used methods. The chapter concludes discussing the advantages of joint interpretation of a set of geophysical methods for site investigation.*

### Preface

*The data set was gathered during the field works for the diploma and master thesis of Hannes Steinel (former at Institute of Geography, University of Leipzig) and Manuel Kreck (former Institute of Geosciences and Geography, Martin-Luther-University Halle-Wittenberg) (KRECK, 2011; STEINEL, 2012).*

## 3.1 Introduction

The use of shallow geophysical methods for the geomorphological characterisation of subsurface features has become very popular in recent years. SCHROTT AND SASS (2008) and VAN DAM (2012) provided examples of how geophysical methods can be utilised for multidimensional identification, distinction, and characterisation of glacial, fluvial, aeolian, volcanic, and tectonic landforms in relation to different survey aims.

Non-invasive geophysical investigation techniques map the contrasts between certain physical properties of the subsurface, which can limit the application range of a particular

method. Over the last decade, *ground penetrating radar (GPR)*, *electrical resistivity tomography (ERT)*, and *refraction seismic (RS)* methods have been proven to deliver valuable information on the dielectric, resistivity, and density properties of subsurface sedimentary structures and compositions for their characterisation (SCHROTT AND SASS, 2008; VAN DAM, 2012). In addition, seismic surface wave techniques, e.g., *multichannel analysis of surface waves (MASW)*, have been recently applied in geomorphological studies, showing that it is possible for this method to complement these techniques, precisely because the same seismic data set can be analysed with regard to surface and refraction waves (SOCCO ET AL., 2010; YAMAKAWA ET AL., 2012). Even though the applied surface wave method delivers more detailed results in comparison with *RS*, it however failed to accurately estimate soil thickness (YAMAKAWA ET AL., 2012). Although increased computational power and light-weight equipment help to improve user-friendliness and time/cost-efficient gathering and processing of high resolution two- and three-dimensional subsurface data, every method has its drawbacks and limitations. These are mainly caused by a lack of contrast between the physical properties of the subsurface to which each technique is sensitive (SCHROTT AND SASS, 2008). Furthermore, the measurement parameters are proxies for several mechanical and physical subsurface characteristics (YAMAKAWA ET AL., 2012). Multiple *GPR*-reflections can occur in gravelly sediments without achieving the main aim of a particular survey, e.g., measuring thickness distribution. The electrical resistivity is mainly dependent on the water content, the fluid composition of the subsurface, and the grain size, thereby leading to the problem of equivalence in two-dimensional resistivity interpretation (HOFFMANN AND DIETRICH, 2004). Methodical difficulties of refraction seismic surveys become apparent with increasing density and therefore increasing velocity with depth. As such, measurements for low velocity and *hidden layers* cannot be registered by the seismogram.

As a result, combining different geophysical methods has become *state-of-the-art* for geomorphological studies, making it possible to overcome the limitations of each technique and to cross-check the results, as well as to determine which method is most suitable for a particular environment (OTTO AND SASS, 2006; SCHROTT AND SASS, 2008; SOCCO ET AL., 2010). Although applied for many geomorphological investigations with various geological settings, studies have shown that *GPR*, *ERT*, and *RS* often yield uncertain results (OTTO AND SASS, 2006; SOCCO ET AL., 2010; YAMAKAWA ET AL., 2012). The *MASW*, as a surface-wave method, is a very powerful tool for the near-surface characterisation of shallow layers and is able to accurately reflect, e.g., the soil–bedrock interface more appropriately than the refraction seismic method, even though larger variations in lateral directions of the one-dimensional profiles also occur (SOCCO ET AL., 2010; YAMAKAWA ET AL., 2012). We considered data acquisition with two different source-offsets to recognise the near-field effects (DIKMEN ET AL., 2010). Furthermore, we combined the resulting dispersion curves of both off-

sets to increase the bandwidth frequency and to resolve shallower and deeper subsurface layers (PARK AND SHAWVER, 2009). This allows increased resolution to be achieved for near-subsurface characterisation. Thus, a validation and a comparison of these resolutions are necessary in order to understand the capabilities, advantages, and limitations of each method.

In this chapter, we present results from applied *GPR*, *ERT*, *RS*, and *MASW* for the delineation of geomorphological features of a filled abandoned meander of the River Mulde in northern Saxony, Germany (Löbnitz test site). We conducted a multi-method investigation to cross-check and verify the results of each individual method. In addition, we compared the findings with data obtained from core samples to evaluate the aforementioned geophysical techniques to establish their ability to provide imaging of fluvial–morphological features.

Structural information about the near surface is not only of great interest in explaining geomorphological evolution, but is also important for geotechnical site assessment. At the study site, we assume a subsurface hydraulic connection given by cut off oxbows that cross a dike structure beneath ground level. This allows a base flow in the direction of the river and in the landside along those channel structures, which is controlled by stream gauge fluctuations and groundwater level. Therefore, these subsurface streams along the abandoned channel structure have a severe impact on the protection capacity of the dike in the case of a flood event.

## 3.2 Field site

For our investigation, we chose an abandoned meander oxbow structure, pre-selected using aerial imaging and on-site reconnaissance. We kindly refer the reader to chapter 2.1 for a general site description (Figure 2-1).

In the foreland of the dike, we can follow the course of the meander up to the River Mulde. At the dike itself, a path crosses the meander. Due to the route of the abandoned meander, we assume a point bar and a cut bank in the northeast and southwest, respectively (Figure 3-1). During field operations, the groundwater table fluctuated between 2–3 m below ground surface level depending on the river level. We performed a multi-method geophysical investigation along the path (including *GPR*, *ERT*, *RS*, and *MASW* surveys) in order to establish the ability of the different methods to provide images of the structure.

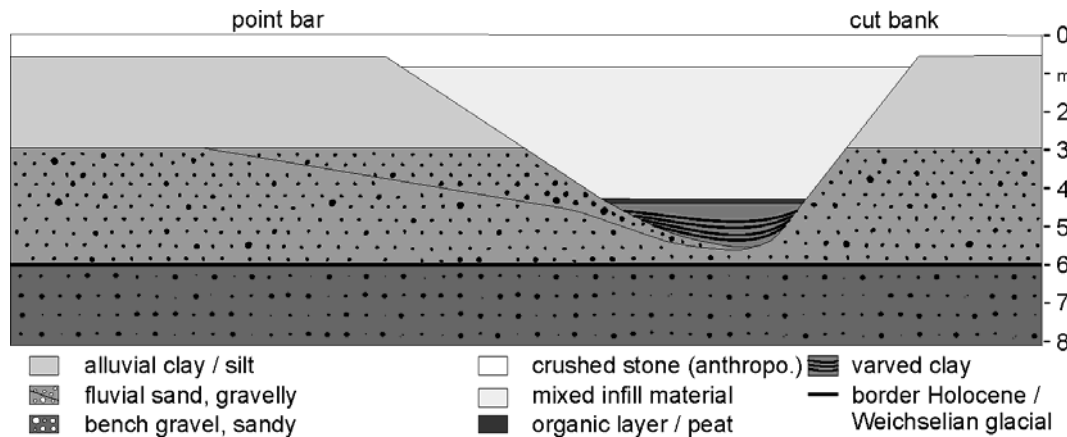


Figure 3-1: Assumed cross section (NE-SW) of the internal geomorphological structure of the abandoned oxbow in the study area according to EISSMANN (1994) and field observations with geological set-up (HAUSMANN, ET AL., 2013).

### 3.3 Methods

#### 3.3.1 Electrical resistivity tomography (ERT)

*ERT* detects apparent specific electrical resistivity/conductivity that relate to lithology. The *ERT*-methods themselves are based on the fundamentals of geoelectric D.C. methods. Thus, inducing a current into a medium (soil) at a pair of electrodes (A–B) creates an electrical potential field that can be analysed. The measurement electrodes (M–N) detect this potential. As such, spatially distributed specific electrical resistivity  $\rho_s$  (and the reciprocal, the electrical conductivity  $\sigma$ ) allows us to obtain information about the media.

Multi-electrode resistivity systems allow two-dimensional images of the subsurface conductivity distribution to be rapidly obtained. A set of electrodes is mounted to the ground with regular spacing (Figure 3-2). A control unit changes the 4-point electrode array to any possible configuration in the profile increasing the spacing  $a$  between the electrodes. Thus, the centre  $x$ -coordinate (located between M–N) is combined with the recorded resistivity values at depth  $y$ . The *ERT* detects two-dimensional resistivities in both vertical and horizontal directions. However, this is a virtual or pseudo-depth that represents the recorded level  $n$  of the electrode array. Thus, values of a number of depths levels are obtained along the profile. The array length defines the maximum investigation depth of the survey. WENNER, SCHLUMBERGER, and DIPOLE-DIPOLE are the most commonly used electrode geometries, e.g., KNÖDEL ET AL. (2007). Subsequently, this data needs to be inverted according to certain initial constraint conditions (starting models). This inversion achieves a depth-truth pattern for the electrical resistivities/conductivities. The combination of linear arrays also allows inversion of three-dimensional resistivity patterns. The configuration of the electrodes determines the spatial resolution of the measurement.

Equation (3-1) describes the calculation of the apparent specific resistivity  $\rho_s$  [ $\Omega\text{m}$ ], where  $k$  [m] is the geometry factor,  $\Delta V$  [V] is the potential difference between electrodes M/N, and  $I$  [A] is the current between electrodes A/B.

$$\rho_s = k \frac{\Delta V}{I} \quad [\Omega\text{m}] \quad (3-1)$$

The electrical conductivity depends on several subsurface properties, e.g., sediment type, water content, grain size, or fluid composition (HOFFMANN AND DIETRICH, 2004; REIN ET AL., 2004; SCHROTT AND SASS, 2008). However, sediment (rocks, soil texture) only exerts a minor influence on the electromagnetic field (except for clay). Thus, the ion-content of the fluid composition is most relevant and influential, e.g., saltwater saturation takes precedence over lithological information.

*ERT* is a commonly-used tool for site investigation. As such, the amount of available relevant literature describing this method is vast. CHAMBERS ET AL. (2012), CLIFFORD ET AL. (2010), CROOK ET AL. (2008), and GOURRY ET AL. (2003) used *ERT* for the characterisation of alluvial deposits. Good examples for geotechnical site investigation are CARDARELLI ET AL. (2010) investigating buried cavities, de LOLLO ET AL. (2011) characterising collapsible soils, NIEDERLEITHINGER ET AL. (2012) inspecting the stability of dikes, MALEHMIR ET AL. (2013) mapping quick clay landslides and SOCCO ET AL. (2010) investigating rock avalanche deposits.

Given our relatively shallow target investigation depth of 10 m, we chose the WENNER- $\alpha$  configuration (Table 3-1) to gain a high-resolution image of the electrical resistivity of the subsurface. This especially enabled us to make distinctions between various lateral subsurface features. The *ERT*-distributions measured across the filled abandoned meander reflected the transition from alluvial clay/silt and gravelly sand to the saturated gravel of the lower terrace. In this respect, a delineation of the assumed point bar, the channel, and the cut bank should be possible (Figure 3-1). At the Löbnitz test site, we acquired *ERT* data using the *Geoserve Resecs* multi-electrode system (URL 7) in WENNER-configuration (Figure 3-2; Table 3-1). To obtain the two-dimensional spatial distribution of the electrical resistivity, we then subsequently inverted the measured apparent resistivity data using *DC2DInvRes* software (RÜCKER ET AL., 2006; GÜNTHER ET AL., 2006; URL 1). Based on the gathered data, we generated a subsurface model by statistical estimation of the electrical resistivity distribution. We continued the inversion procedure until the root mean square value reached its minima.

### 3.3.2 Ground penetrating radar (*GPR*)

*GPR* is based on changes in the dielectric properties of the substrate and provides high-resolution three-dimensional images of the subsurface of the earth. This imaging method utilises the transmission and reflection of high-frequency electromagnetic (*EM*) waves within

the earth to obtain this data (interaction between the transmitted *EM*-energy and the spatial variation in the layer (KNIGHT, 2001).

*GPR*-surveys are conducted by pulling an antenna along the earth's surface and measuring at various frequencies (10 Hz–1 GHz). As such, any inhomogeneities or layer boundaries reflect the emitted electromagnetic signal (Figure 3-3). The receiver antenna subsequently registers the reflected signal. Dielectrical contrasts originate from changes of material texture, water content and the electrical conductivity of the pore fluids. Variations of the water content especially affect the dielectrical properties of the subsurface and cause radar reflections. Hence, the penetration depth of *GPR*-investigations is (apart from structural setup) mostly dependent on the frequency of the emitting antenna. Whereas low frequencies sample deeper layers, high frequencies achieve a higher spatial resolution in shallower parts of the subsurface, but at the expense of penetration depth. Thus, radar systems are used for many varied applications such as investigating contaminant plumes, characterising landforms (geologic/geomorphologic structure), and assigning values of hydrogeological properties (water content, porosity, permeability, etc.). This allows the assessment of groundwater resources (BECHT ET AL., 2006), mineral exploration, archaeological studies (BONINGER ET AL., 2010), geotechnical site characterisation (NIEDERLEITHINGER ET AL., 2012) and environmental applications (KNIGHT, 2001). KNIGHT (2001) and SLOB ET AL. (2010) provide examples of the base principles. VAN DAM (2012) and NEAL (2004) showed application of this method in sedimentology and landform characterisation, respectively. Geomorphological applications of *GPR* can be found in numerous environments, but is predominantly used for shallow talus slope (SASS, 2006), dune complex investigations (BENNETT ET AL., 2009; VAN DAM, 2012), and characterisations of rock glaciers (MONNIER ET AL., 2011). Alluvial environments often provide good conditions for the application of *GPR*-methods to detect the architecture of deposits, as demonstrated in several case studies, e.g., ANDERSON ET AL. (2003), BANO ET AL. (2000), BRIDGE ET AL. (1998), FROESE ET AL. (2005), GOURRY ET AL. (2003), AND VANDERBERGE AND VAN OVERMEEREN (1999).

At the Löbnitz test site, we conducted *GPR*-measurements using a 200-MHz antenna *SIR-30<sup>TM</sup>* designed by *Geophysical Survey Systems Inc.*, USA (URL 21; Table 3-1). The acquired data was processed using *ReflexW* software (URL 17). The reflections are associated with depth-based values related to the corresponding travelttime, which was 0.11 m/ns.

### **3.3.3 Refraction seismic (*RS*)**

The *RS*-method detects primary (also longitudinal or compressional) waves (*P*-waves) and shear waves (*S*-waves) that are refracted and reflected at inhomogeneities (layer boundaries) in the subsurface (Figure 3-4). The base principle of seismic methods, and there-

fore also for *RS*, is a controlled generation of elastic waves by a source. This enables an image of the subsurface to be obtained (KNÖDEL ET AL., 1997, 2007). The ray paths of the waves depend on changes in the elastic modulus of soil/rock as a function of density, lithology, material composition, porosity, saturation, and compaction.

Geophones record the reflected P-waves at the surface (or at an *in situ* position, e.g., borehole → *STT*, Chapter 4). The geophones then transform the detected elastic wave into a digital signal which can be analysed. The main information required is the wave amplitude over time (traveltime curves). During analysis, the first arrival time is picked. Combining the selection of several geophones of an array (shot pattern), allows inversion of these first arrival times to be used to obtain a velocity distribution of the medium. An increase in density, and therefore, in P-wave velocity  $v_p$ , is a necessary precondition of this method, preventing the detection of layers with inverse velocity gradients (low velocity layers). Another limitation of *RS* is the inability to resolve thin layers, especially in greater depths. From first arrival traveltime curves, so-called *hidden layers* cannot be distinguished. Nevertheless, *RS* is a commonly used method, e.g., for aquifer characterisation (GE ET AL., 2010A, 2010B), in slope investigations (TRAVELLETTI ET AL., 2010), and for differentiating sediment types and bedrock (SCHROTT ET AL., 2003).

At the Löbnitz test site, we used 4.5-Hz geophones (Table 3-1) designed by *Geospace Technologies*, USA (URL 10) in combination with controlling units (geodes) designed by *Geometrics Inc.*, USA (URL 7), including the software *Seismodule Controller* (URL 18). We used a plastic hammer and a metal plate to induce the signal. The geophone positions remained fixed during acquisition. Measurements were gathered at offset distances of 16, 8, and 4 m on both profiles, every 2 m within the spread and condensed to 1 m while passing the filled channel. We processed the obtained data with *Reflex* (URL 17) and *Ra/TT2dTomo* (GÜNTHER, 2005; URL 18).

### **3.3.4 Multichannel analysis of surface waves (*MASW*)**

The *MASW*-method utilises the dispersive features of surface waves, primarily Rayleigh-waves, for imaging velocity patterns of the subsurface (PARK ET AL., 1999, 2007). Rayleigh-waves make up two-thirds of the induced seismic signal. Depending on the frequency, they propagate through different depths with certain phase velocities, mainly influenced by density and stiffness of the subsurface. We processed the data to obtain dispersion curves, i.e, the ratio between the frequency and phase velocity, which depend on S-wave velocities  $v_s$ . Thus, we can obtain one-dimensional S-wave velocity profiles (separately calculated for each linear spread), whereby each one-dimensional profile is

located relative to the corresponding mid-spread position (XIA ET AL., 2000; LOU ET AL., 2009; Figure 3-5).

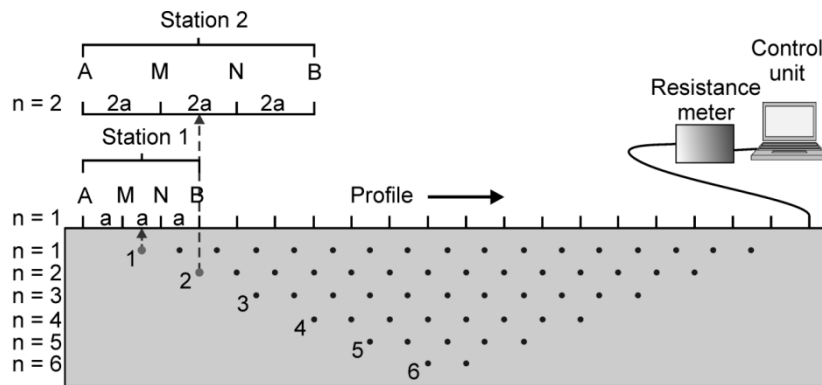


Figure 3-2: Measurement principle of a multi-electrode WENNER-configuration for D.C. ERT (KNÖDEL ET AL., 1997; modified).

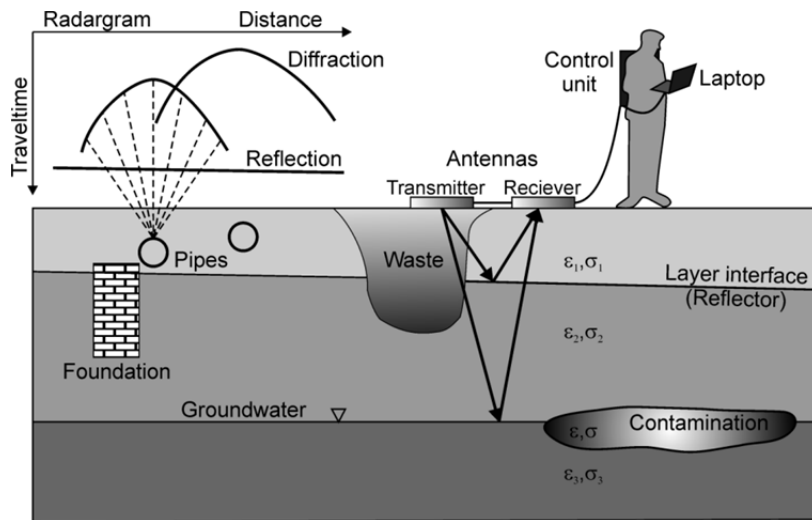


Figure 3-3: Measurement principle of *ground penetrating radar (GPR)* (KNÖDEL ET AL., 1997; modified).

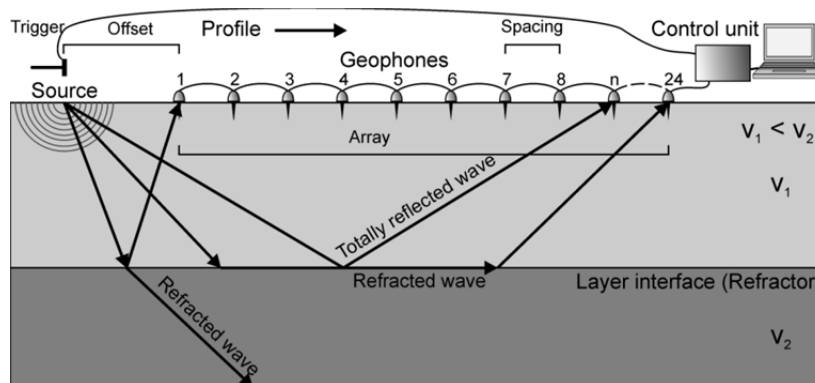


Figure 3-4: Measurement principle of *refraction seismic (RS)*.

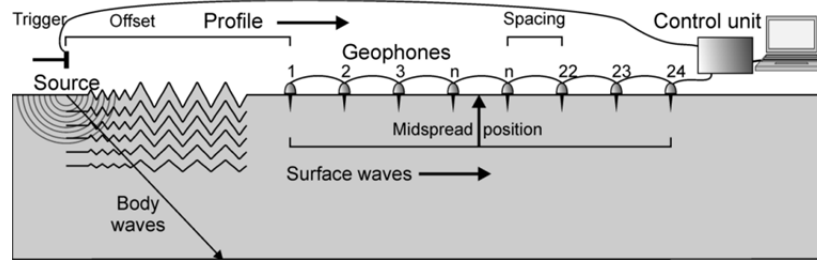


Figure 3-5: Measurement principle of *multichannel analysis of surface waves (MASW)*.

Accordingly, we subsequently inverted the curves in order to estimate a one-dimensional S-wave velocity profile. After this, we arranged the resulting one-dimensional profile results next to each other - generating pseudo-two-dimensional cross-sections according to the methods outlined by XIA ET AL. (2000). However, dispersion analysis along the energy maxima of the fundamental is the most critical point, since the quality directly influences the obtained S-wave velocity to be used for geotechnical parameterisation.

Thus, this approach has become *state-of-the-art* for active surface wave profiling and the qualitative interpretation of subsurface features, due to increased computational power and the availability of *MASW*-software. The *Kansas Geological Survey* (URL 13) originally developed the *MASW*-method. FOTI ET AL. (2011) and SOCCO AND STROBBIA (2004) provided a general introduction to surface wave methods for site characterisation. A considerable number of studies have been published on the application of various near-surface investigation methods in several environments, including for geotechnical purposes, e.g., ISMAIL AND ANDERSON (2007) and SOCCO ET AL. (2008), geophysical surveys, e.g., DEBEGLIA ET AL. (2006) and ROY AND STEWART (2012), and in geomorphological studies, e.g., COULOUMA ET AL. (2012), SOCCO ET AL. (2010), and YAMAKAWA ET AL. (2012). We kindly refer the reader to STEINEL (2012) for more detailed information, who further investigated available geometries and applications of *MASW* in the framework of this thesis.

Contrary to the *RS*-method, inverse velocity structures affect the dispersive characteristics of the Rayleigh-wave. Therefore, the *MASW*-technique could provide more reliable/detailed information of S-wave velocity distribution and its features. Given the similar measurement setup utilised, the seismic record can be analysed according to both *RS* and *MASW*-methods.

We also acquired surface wave data from the *RS*-survey using this identical setup. With an additional 24 geophones, we extended the profile in a northwesterly direction. Taking near-field effects into account, we chose source offsets of 4 and 8 m for every mid-spread position (DIKMEN ET AL., 2010). Furthermore, we combined the resulting dispersion curves of both offsets to increase the bandwidth frequency and to resolve shallower and deeper subsurface layers (PARK AND SHAWVER, 2009). We performed measurements at 2-m intervals, with the source being located northwest of the spread. Afterwards, we reduced the

seismic records, obtaining 49 seismograms with 24 traces and a spread length of 23 m for each shot position and offset (Table 3-1).

For each offset shot position, we extracted the fundamental mode dispersive characteristics of the seismogram using the *SeisImager/SW* software package (*Geometrics Inc.*, USA; URL 18). Then we selected the energy maxima and combined the dispersion curve for the corresponding mid-spread position of the 4- and 8-m offsets. The inversion was performed using a genetic algorithm according to PAROLAI ET AL. (2005), PICOZZI ET AL. (2005), PILZ ET AL. (2010), and BOXBERGER ET AL. (2011); Figure 3-6.

Based on a six-layer starting model and a pre-defined search area (Table 3-2), the algorithm searches for a global solution during each model generation, employing genetic operations (namely crossover, elite selection, and dynamic mutation). The algorithm stopped deriving iterations after 50 generations, resulting in minimum misfits of mostly < 3 % between measured and calculated dispersion curves. Then we interpolated the depth steps of the resulting one-dimensional S-wave velocity profile to an equal thickness of 0.1 m. We subsequently utilised this approach for every mid-spread position. Finally, we applied the topography and plotted the velocity profiles next to each other, generating a pseudo-two-dimensional S-wave velocity section.

Table 3-1: Geometrical parameters of applied geophysical methods for *ERT* (WENNER- $\alpha$ ), *GPR*, *RS*, and *MASW* (HAUSMANN ET AL., 2013).

| Method      | Profile Length<br>[m] | Channel<br>Number | Max. Offset<br>[m] | Spacing<br>[m] | Shot Distance<br>[m] | Stacks<br>[n] |
|-------------|-----------------------|-------------------|--------------------|----------------|----------------------|---------------|
| <i>ERT</i>  | 96                    | 96                | -                  | 1              | -                    | -             |
| <i>GPR</i>  | 88                    | -                 | -                  | const.         | -                    | -             |
| <i>RS</i>   | 96                    | 96                | 16                 | 1              | 1 and 2*             | 3             |
| <i>MASW</i> | 96                    | 24                | 4 and 8            | 1              | 2                    | 3             |

\* Shot distance was set to 1 m inside and 2 m outside of the meander structure.

Table 3-2: Predefined start model parameter space for generic algorithm inversion with minimum and maximum S-wave velocities  $v_s$  and layer thicknesses  $H$ , respectively; density is fixed for all layers at  $1.8 \text{ g/cm}^3$  (HAUSMANN ET AL., 2013).

| $v_{s,min}$ [m/s] | $v_{s,max}$ [m/s] | $H_{min}$ [m] | $H_{max}$ [m] |
|-------------------|-------------------|---------------|---------------|
| 50                | 300               | 0.5           | 1             |
| 50                | 350               | 1             | 1.5           |
| 50                | 350               | 1             | 1.5           |
| 50                | 350               | 1             | 1.5           |
| 80                | 500               | 1             | 2             |
| 100               | 600               |               | half-space    |

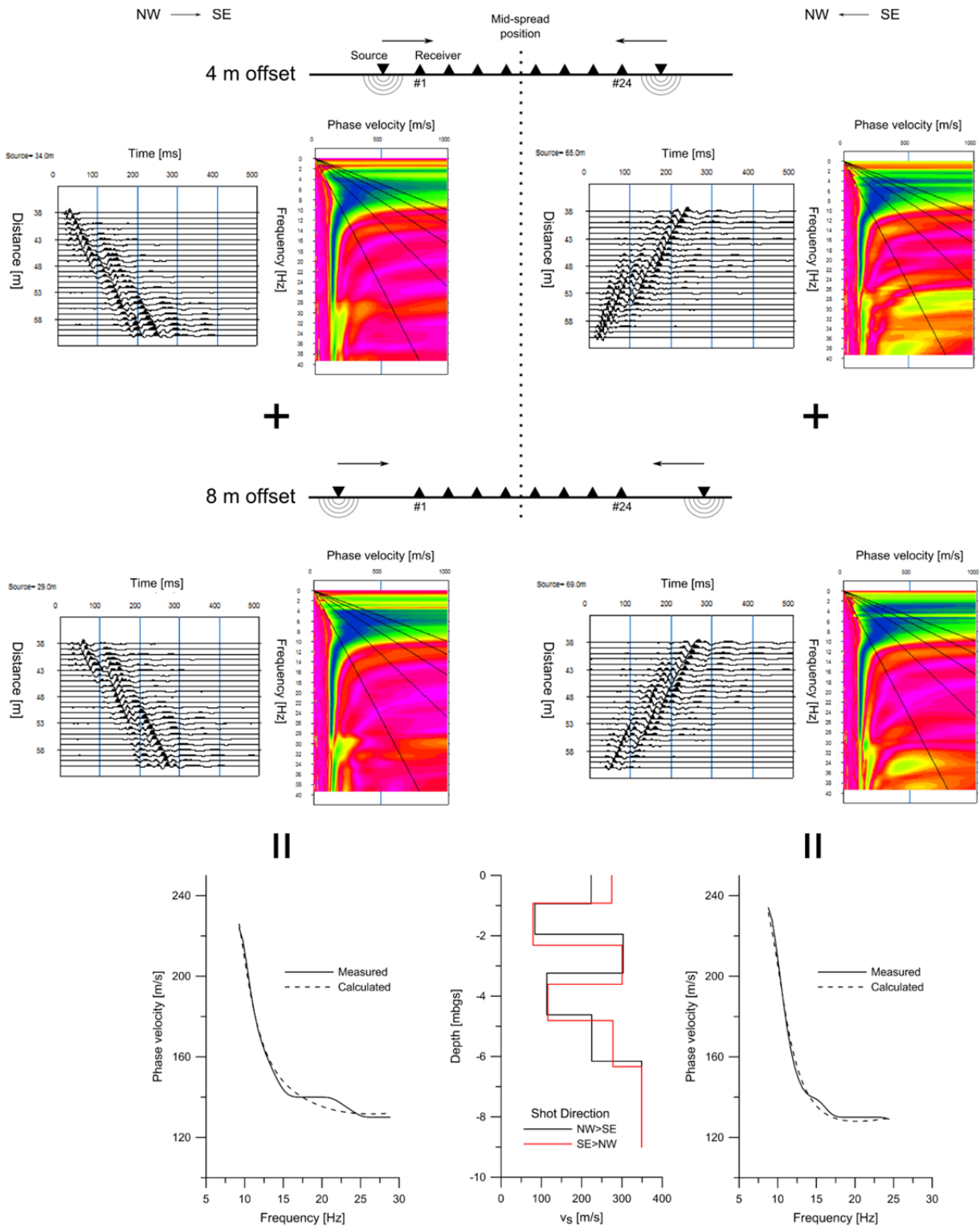


Figure 3-6: Processing scheme of bidirectional MASW profiling exemplarily illustrated for 49.5-m mid-spread position of the Löbnitz profiles; shooting is performed from NW and SE direction for the same mid-spread position. The resulting dispersion curves for 4 and 8-m offsets are combined and then inverted via genetic algorithm (PAROLAI ET AL., 2005; PICOZZI ET AL., 2005; PILZ ET AL., 2010; BOXBERGER ET AL., 2011); from STEINEL ET AL. (SUBMITTED).

### 3.3.5 Soil sampling (SS)

The *DP*-based *soil sampling (SS)* methods are the modern day equivalent to common investigation drillings. These techniques are principally based on the advancement of hollow sampling tool into the ground. Generally, we can distinguish between two major groups of soil sampling tools (open and closed piston samplers), that enable a broad range of soil sampling techniques to be undertaken. Closed piston systems remain shut (in contrast to open piston systems) and do not open until the sample (target) depth is reached. Therefore, these devices allow depth sampling (in sections), which is highly advantageous. Furthermore, *SS* is available in the form of *single rod systems* or *dual-tube-systems* (used here). Both have several advantages and disadvantages, as discussed for example in ZSCHORNACK AND LEVEN (2012B). EPA (1997), DIETRICH AND LEVEN (2006), LEVEN ET AL. (2011), and MCCALL ET AL. (2005) provided an overview of the different *SS*-methods.

We accomplished our drillings using *DP*-procedures, where high frequency vibrations (*SONIC*) and the weight of the mobile platform push the probe devices into the ground (*SonicSampDrill BV.*, The Netherlands; URL 18). As this is taking place, subsurface material fills a plastic tube. Thus, we obtain our probe core that can be subsequently analysed.

We used the core samples for ground truthing and for correlation of the sediment types, so as to highlight any alterations in the measured geophysical properties. Accordingly, we conducted five *DP*-sonic core drillings along the path. Three were located in the area of the channel and the other two in the NW and SE sections of the abandoned meander (Figure 3-7). At each sampling point, we drilled 4 core sections each of 2-m length, resulting in a final depth of 8 m (Appendix B). Then we described the core pull and classified it according to grain size composition. We expect that our results will support the classifications obtained from the *ERT*, *GPR*, *RS*, and *MASW* findings.

## 3.4 Results

### 3.4.1 Electrical resistivity tomography (*ERT*)

The two-dimensional *ERT*-image (Figure 3-7A) implies the existence of an anomalous subsurface structure, which is composed of two layers with laterally high spatial variation. Relatively high resistivity values of about 500–1,000  $\Omega$ -m characterise the upper layer, which reaches a depth of 3 m, after which the resistivity values decrease gradually. The bottom layer sharply limits the anomaly with relatively low resistivities of 0–60  $\Omega$ -m, which reach the surface NW and SE parts of the profile. High resistivity values at shallow depths in the NW part of the profile may be because of the path itself or loamy sediments from the haugh. High resistivities at greater depths in the SE section occur as a result of the abandoned channel

being filled. Low resistivities are associated with highly conductive saturated sediments. This distribution concurs with the geomorphological evidence of the cut bank and point bar, which are observable at the surface. Moreover, we can clearly identify the assumed fluvial–morphological features from the *ERT*-image. Whereas high resistivity values are missing in the SE section of the profile, they are concentrated in the NW area at shallow depths — this represents a point bar limiting the filled channel. Thus, the sharp lateral resistivity contrast in the SE section of the profile represents a cut bank.

### 3.4.2 Ground penetrating radar (*GPR*)

The *GPR*-measurements reveal near-surface-parallel radar reflections along the entire profile that correspond to the path along which the data was gathered (Figure 3-7B). Repeated wave arrivals in depths of 3–4 m are not attributable to geological structures. However, there are strong multiple radar reflections, which start 20 m along the profile at a depth of 2 m. Monitoring these reflections helped indicate the features of the abandoned channel (down to a depth of 3 m in the area 45–65 m along the profile). These reflections are sharply limited at the end of the channel in the SE direction. In the next profile area beside the channel, they are completely absent. We interpret this boundary as being a cut bank. Other sharp reflective layers are not detectable because of the geological setup, which may yield only low dielectrical contrasts. In addition, possible reflective layers such as gravelly sediments in larger depths are not detectable due to the applied antenna frequency. Therefore, *GPR*-results do not provide total coverage of the channel structure because of the lack of penetration depth.

### 3.4.3 Refraction seismic (*RS*)

The profile reveals a two-layer composition with high contrasts (Figure 3-7C). A refracting layer underlies the initial shallow layer with modelled P-wave velocities of 400–600 m/s. This lower layer shows increasing velocities, ranging from 1,000–1,900 m/s at a depth of around 4 m in the area between 0–43 m and at 5 m for distances between 45–60 m along the profile. In this area, P-wave velocities of 500 m/s dominate the upper part of the subsurface, indicating the abandoned channel. The initial shallow layer only occurs in the NW area of the profile, highlighting the presence of a point bar, whereas this layer is missing in the SE section. Here, shallow velocities of 800–900 m/s represent the cut bank. Moreover, we assume that the gravel of the lower layer (bench gravel) acts as a refractor. Therefore, we regard the slow velocities in the upper part of the subsurface in the NW area of the profile to be poorly compacted materials, i.e., loamy sediments from the haugh. In contrast, higher velocities in the area 70–90 m of the profile may represent different sediments, for instance, more highly compacted loam or silt. Inside the channel, loose inward filling may cause the

lowest velocities, which were achieved in this *RS*-section. The profile area before 0 m is negligible, as the traveltimes curves do not overlap. Therefore, the velocity data is erroneous in this area.

#### 3.4.4 Multichannel analysis of surface waves (*MASW*)

As can be seen in Figure 3-7D, the *MASW*-results show a laterally and vertically more heterogeneous spatial velocity distribution than the *RS*-results (Figure 3-7C). This method detected inverse layers with greater velocity than deeper layers. For example, a relatively high-velocity layer at the top covers almost the entire pseudo-two-dimensional section shown, representing the path material and overlying low velocity subsurface features. In the NW section of the profile, a relatively homogenous velocity distribution of 100–200 m/s follows, down to a depth of 5 m between the region -12–23 m along the profile. Here, the S-wave velocity increases from 300 up to 400 m/s at a depth of 5 m down to 6 m. We see a similar velocity distribution at the end of the profile, between the 65- and 83-m points, indicating the same material composition. However, here we detected a velocity boundary >300 m/s at a depth of around 4 m, which describes the cut bank of the abandoned meander that delimits the channel in the SE area of the profile. Within the filled channel between profile points 27–63 m, the  $v_s$ -profile displays a more heterogeneous velocity distribution. Relatively high velocities of 200–300 m/s characterise the uppermost layer, which has an underlying inverse layer with velocities of 50–100 m/s down to a depth of 2.5 m. After repeatedly increasing the S-wave velocity (200–300 m/s), we observed that the velocities of the underlying layer decrease once more (100–200 m/s). At a depth of 6 m, we see a high contrast increase in velocity (>300 m/s). The trend of this velocity boundary corresponds well with that of the refracting layer of the *RS* and is therefore associated with the gravelly sediments of the lower layer (bench gravel), which clearly defines the channel structure. Because of the velocity distribution within the channel, we assume that inward filling occurs down to a depth of 3.5 m; whereas the uppermost layer is composed of anthropogenic sediment materials, and the underlying layer is made up of restored alluvial silt. These sharply contrasting deposits overlay fluvial sediments of the abandoned channel, which reaches down to a depth of 6 m. This depth represents the bottom of the channel.

#### 3.4.5 Soil sampling (*SS*)

The *SS*-results reflect the geological setting of the area (Figure 3-7). We found path-filling material in the uppermost parts of all cores. In the NW and SE areas of the abandoned meander (cores L/SON-1 and L/SON-5), loamy and silty materials represent haugh sediments and alluvial clay, respectively. In the NW section, this layer reaches to a depth of 3.3 m and, in the SE section, to a depth of 3.4 m. Here, more sandy materials characterise

this layer. Sand and gravel mixtures underlay the haugh sediments in the NW region. Sandy layers with various grain sizes characterise the subsurface region in the SE. Within the abandoned meander, we found a similar sediment composition. Sandy and clayey materials of the haugh characterise the uppermost layers of cores L/SON-2 and L/SON-3. An underlying layer (composed of sand with varying grain sizes) initially merges with stream gravel (gravel bars) and then with gravel in the lower terrace at a depth of 5–6 m. This phenomenon is observable in nearly all of the core samples. In the channel region (core L/SON-4), we see a different composition. Inward filling with loamy sand is observable to a depth of 3 m, which corresponds to the haugh boundary of the adjacent sampling points. Beneath a thin organic layer, we drilled a banded sandy loam mixture, indicating limnic conditions inside the channel. The next layer is composed of sand and gravel, merging into gravel of the lower bench at a depth of 6 m.

### 3.5 Discussion

The results reflect the different dependencies of each method on various physical properties of the subsurface. However, we can delineate fluvial–morphological features of the abandoned meander in all images (Figure 3-7). By comparing individual results with each other, some variations could be seen in actual results achieved using the different methods (Figure 3-8). The *ERT*-measurements are mainly dependent on the water content of the subsurface (HOFFMANN AND DIETRICH, 2004). Thus, we have to understand the detected boundaries as resistivity contrasts, from high to low, in unsaturated sediments. Hence, the mapped boundaries of the point bar, channel, and cut bank (from NW to SE) may not match the real boundaries that we recorded or may yield results that vary somewhat (are generally lower) using *RS* and *MASW*-methods. The anomalous resistivity structure at around 20 m along the profile and occurring at a depth of 4 m may be an indicator of gravelly layers. Such layers were also found in the core sample L/SON-2 (Figure 3-7A). While perhaps not representing an inversion artefact, this anomaly shows however that those layers under a depth of 4 m are not detectable using the *WENNER- $\alpha$*  configuration or *ERT* in general because of water saturation. Moreover, the high resistivity boundary (200  $\Omega$ -m) seems to correlate with inward filling in the channel section, as clearly evidenced by the *MASW*-method results (Figure 3-7D). Due to the small-scale resistivity variations of the subsurface, we could not reach the actual target depth. The *ERT*-method delineates the path on which the measurements were conducted as well as the inwardly filled region, as is indicated by the high resistivities (700–1,600  $\Omega$ -m). As a result, the *ERT*-image does not reveal the real depth of the meander structure but can be used to characterise the overall extent and degree of infilling.

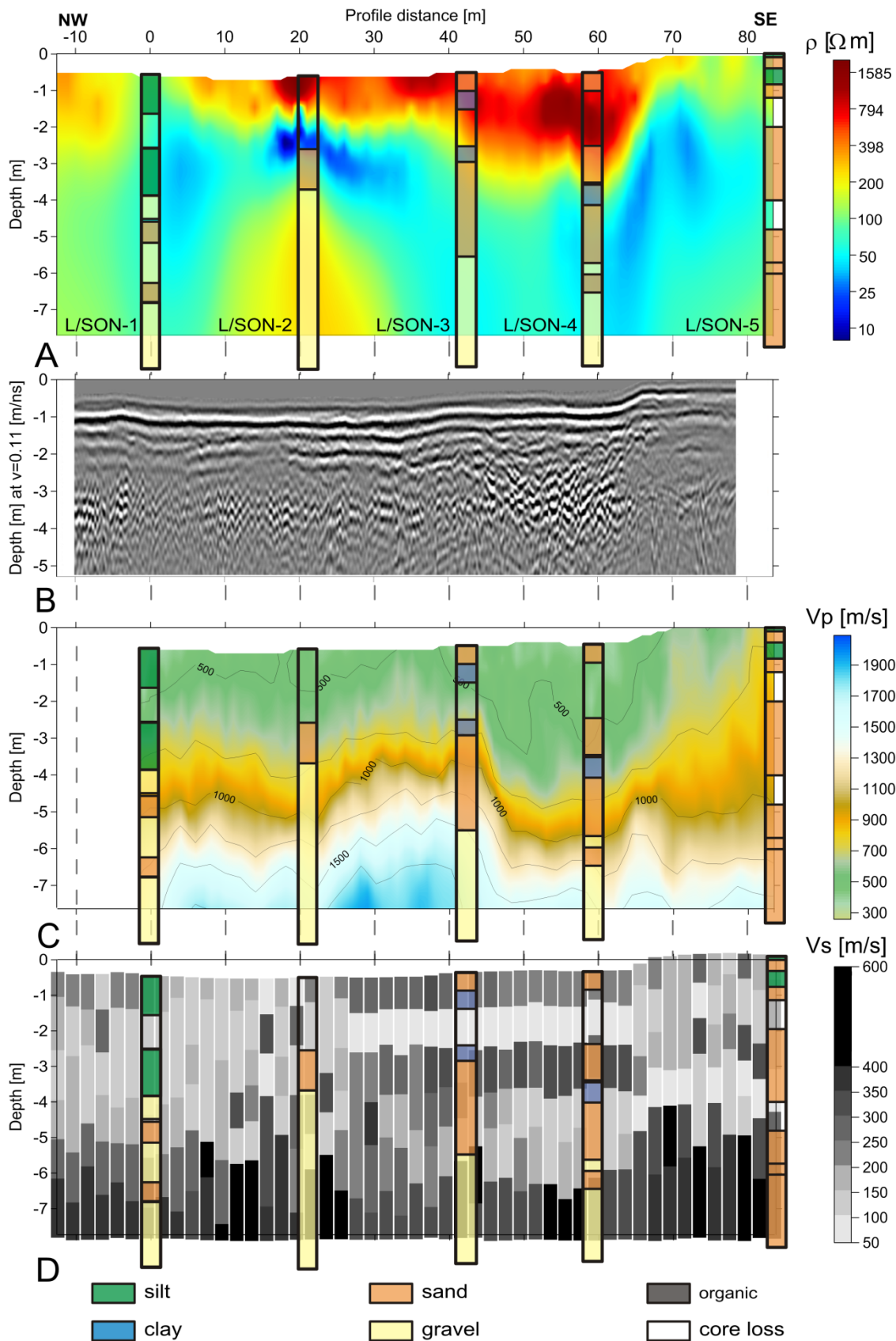


Figure 3-7: A) ERT electrical resistivity  $\rho$  [ohm-m]; B) GPR reflection pattern; C) RS refraction seismic P-wave velocity  $v_p$  [m/s]; D) MASW S-wave velocity  $v_s$  [m/s]; Soil cores (L/SON-1 – L/SON-5; Appendix B; colour-coded according to the occurring dominant grain size component) in comparison with results from geophysical surveys, proportion of horizontal to vertical scale 1:5 (HAUSMANN ET AL., 2013; modified).

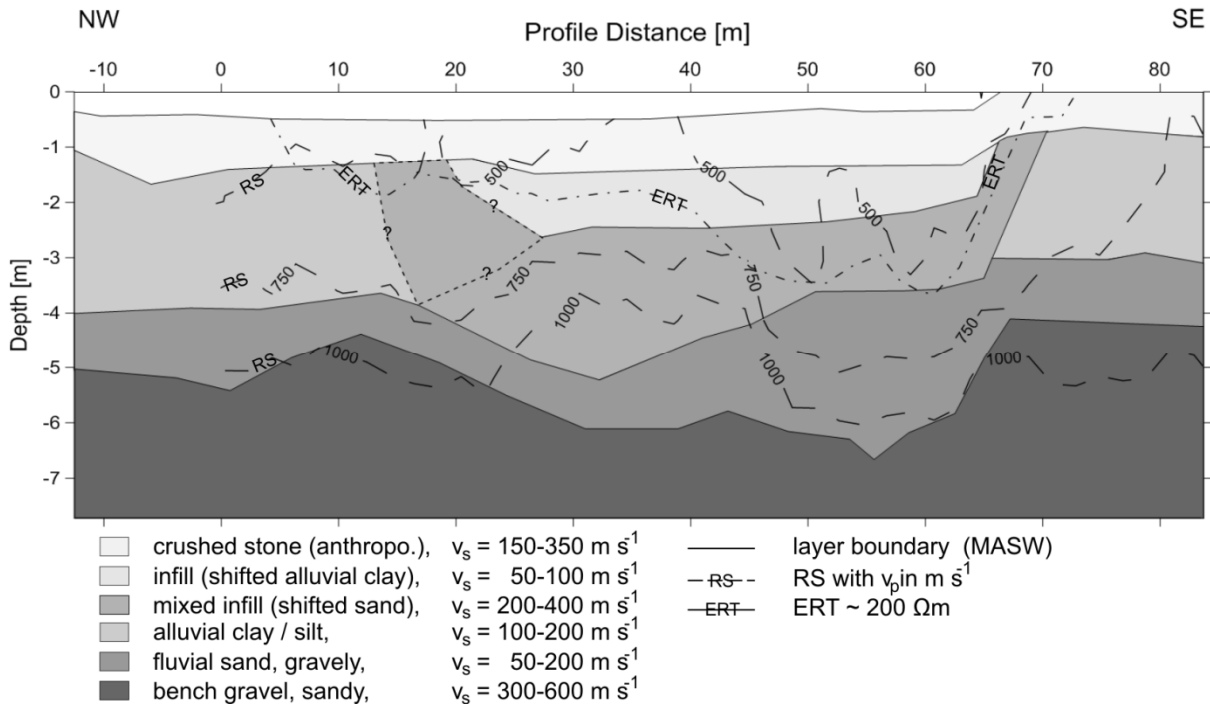


Figure 3-8: Depth distribution and joint interpretation of the geomorphological structures based on MASW S-wave velocity  $v_s$  [m/s]; also included isoline of refraction seismic (RS) P-wave velocity  $v_p$  [m/s], ERT electrical resistivity  $\rho_s$  at  $\sim 200 \Omega\text{-m}$ , and GPR-reflections; proportion of horizontal to vertical scale 1:5 (HAUSMANN ET AL., 2013).

The GPR-results support the ERT-findings and vice versa (Figure 3-7A, B). Here, the investigated reflective layer corresponds well to the high electrical resistivity boundary along the entire profile (Figure 3-8). Therefore, GPR-measurements also seem to map the limits of the infilling, resolving any uncertainties connected with ERT-measurements.

In the RS and MASW-results, high gravel velocities of the lower layer ( $v_p > 1,000 \text{ m/s}$ ,  $v_s > 350 \text{ m/s}$ ) define the abandoned channel structures (Figure 3-7C, D, Figure 3-8). Whereas the P-wave velocities of the RS-measurements increase gradually with depth, the MASW pseudo-two-dimensional cross section shows a vertically and laterally more highly differentiated spatial S-wave velocity distribution. This provides a more detailed insight into internal channel features that could not be obtained in the RS-results. The path and the infilling of the channel in the uppermost layers of the subsurface can be especially well identified by the surface wave method (MASW). These inverse velocity structures cannot be detected with RS because of the aforementioned precondition of this method. In addition, inward filling causes a lowering of the 1,000 m/s boundary in the P-wave velocity image up to a depth of 4 m within the range 30–42 m along the profile (Figure 3-7C, Figure 3-8), which helps highlight the low velocity layer problem of the RS-method. In contrast, the groundwater level does not affect the RS-results, which may be because of an inconsistent subsurface distribution or small-scale level changes. The global influence of the subsurface features underneath the spread causes local anomalies in the one-dimensional S-wave velocity profile of the MASW-section

(Figure 3-7D). This is due to the arrangement of the dispersion characteristics and the inverted S-wave velocity profile to the mid-spread position, according to LOU ET AL. (2009). However, combining the one-dimensional S-wave profiles to a pseudo-two-dimensional cross section helps overcome any misinterpretation of the local anomalies. To conclude, both seismic techniques are able to delineate the point bar, the channel, and the cut bank with high congruence (Figure 3-8), but the surface wave method yielded better layer resolution than the refraction seismic method due to methodological restrictions. Both data sets were acquired in the same seismic survey. Therefore, the *MASW* is seen as a method that delivers more highly detailed information, requiring just a little more data inversion and calculation effort than field work.

The core drillings validate the findings of the geophysical investigations, most notably in the seismic results (Figure 3-7C, D). Given its dependence on water content, electrical resistivity values do not correlate to certain sediment layers (Figure 3-7A). Thus, the low resistivity values of the highly conductive saturated sands make the detection of gravel, as the channel base, impossible. Although P- and S-wave velocities refer to functions of several physical properties of the subsurface, the drilling results fit reasonably well with both images (Figure 3-7C, D). Gravelly layers correspond especially well with high velocities, which define the structural setup of the abandoned meander. Furthermore, the absence of gravelly sediments in the drilling at the SE end of the profile can also be seen in the *RS*-results where P-wave velocities <1,000 m/s dominate the area of the cut bank. However, the *MASW* pseudo-two-dimensional S-wave velocity section represents a more heterogeneous image of the spatial distribution of velocity structures, exhibiting high congruence with the results obtained from core drilling. This provides more information about the channel's internal structure as well as its overall limits. Sediment changes correlate with changes in S-wave velocities. Haugh, sand, and gravel layers are noticeable in the *MASW*-image (Figure 3-7D). Thus, the results provide extra information about the channel's internal structure. However, the *RS*-method is not able to detect the inverse structures of the infilling or any small-scale layer changes, as is indicated by highly variable S-wave velocities (Figure 3-8). Hence, the *MASW*-method provides the most detailed structural information of all four geophysical methods tested with respect to the aim of achieving two-dimensional geomorphological characterisation of an abandoned meander. At the study site, this additional information can be used to provide answers to certain questions, e.g., estimation of base flow in sediments with higher hydraulic conductivity given by subsurface hydraulic connection in cut off oxbows beneath the dike. Therefore, this data is not only of great interest for explaining geomorphological evolution but also for geotechnical site assessment and for evaluating the impact on the protection capacity of the dike in the eventually of a flood event.

*“Notice 1: This is the author’s version of a work that was accepted for publication in Geomorphology. Changes resulting from the publishing process, such as peer review, editing, corrections, structural formatting, and other quality control mechanism may not reflected in this document. Changes may have been made to this work since it was submitted for publication. A definitive version was subsequently published in Geomorphology, published online July 13th, 2013 doi:10.1016/j.geomorph.2013.07.009”*

*Postscript*

*The results of this chapter deliver detailed knowledge about the subsurface structures of the selected profile at the Löbnitz test site. Hence, this structural information is useful for interpretation of results from seismic traveltime tomography (STT) discussed in the next chapter.*



## 4 Mobile DP-based seismic travelttime tomography for geotechnical site characterisation

### Chapter Outline

*This chapter describes the experimental design and results from a mobile DP-based seismic travelttime tomography tested at the Löbnitz test site. The chapter highlights are:*

- *Novel experimental design for seismic travelttime tomography allows simultaneous acquisition and recording of P- and S-waves.*
- *Constructed velocity pattern from of the recorded P- and S-waves using particle swarm optimisation deliver reliable data for geotechnical site characterisation also for uncertainty appraisal.*
- *Cone penetration testing and soil sampling validate of geophysical results.*

### Preface

*Selection/picking of the seismic data obtained from the aforementioned experiment and model generation (P/S-wave quantiles) with particle swarm optimisation (PSO) was performed by Michael Rumpf (Institute of Earth and Environmental Science, University of Potsdam), who also provided the description of the PSO in Chapter 4.3.2. We thank Dr. Thomas Fechner (Geotomographie GmbH, Germany) for providing support when inverting the simple tomograms with GeoTomCG software.*

## 4.1 Introduction

Knowledge of the spatial distribution of geotechnical parameters is essential for a thorough assessment of construction sites, e.g., for large building sites. Geotechnical parameters are usually pointwise measurements, e.g., drill logs from a certain location (one-dimensional data). However, because of the high spatial variability of geotechnical parameters in unconsolidated near-surface sediments, this data cannot reliably assess the heterogeneity of the subsurface. Thus, auxiliary geophysical methods and appropriate tomographic reconstruction techniques provide data and models such as seismic velocities that describe the distribution of physical parameters in one, two, and three dimensions.

Nowadays, P-wave tomography is used exclusively for local high-resolution site assessment. BECHT ET AL. (2007) showed the high potential of such an approach for aquifer

characterisation. However, because determination of the relevant geotechnical parameters (shear modulus, Poisson's ratio, etc.; SCHÖN, 1998) depends on knowledge of both P-wave and S-wave velocities, the benefits are limited. This is especially the case for near-surface crosshole experiments where P- and S-wave crosshole traveltime data is acquired separately (ANGIONI ET AL., 2003; DIETRICH AND TRONICKE, 2009; LINDER ET AL., 2010) using sources which are either designed to generate P-wave or SH-waves. However, existing commercial S-wave sources are capable of generating relatively energy-rich and high-frequency P-waves as well. Simultaneous acquisition of P- and S-wave crosshole traveltimes would increase the cost/time effectiveness and efficiency of seismic surveys.

In this chapter, we present an experimental setup design and provide data examples obtained from a *crosshole seismic experiment* for characterisation of the foreland of a dike at Löbnitz, Germany (Löbnitz test site; Figure 2-1). We developed a method for mobile near-surface P- and S-wave tomography based on *DP*-methods which can be used for installation of temporarily boreholes. The rods of the *DP*-methods contain the seismic components (source and receiver). Thus, the steel rods of the temporary boreholes are used as casing. Hence, these temporarily installed boreholes help to overcome the requirement of permanent on-site boreholes, as shown in previous studies, e.g., PAASCHE ET AL. (2009). After providing background information on our experimental setup design and the data quality, we present jointly inverted P- and S-wave velocity model ensembles that utilises a *particle swarm optimisation (PSO)* approach and we explain the thereof derived geotechnical parameters (elastic moduli, gravimetric water content, etc.). This data allows us to make a description of the subsurface according to stratigraphy and geotechnical purposes (including an uncertainty appraisal). In addition, we used *DP*-probes (*CPT*, *SS*) for *in situ* characterisation of the subsurface and as a ground truthing method for the geophysical results (DIETRICH AND LEVEN, 2006).

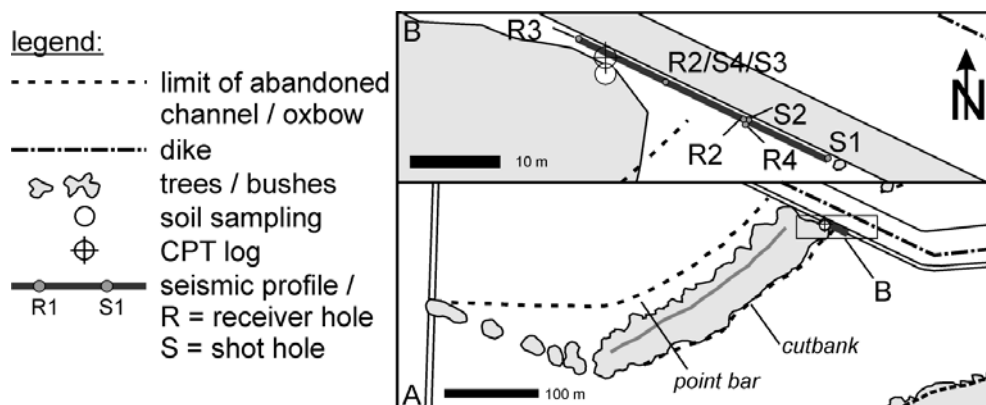


Figure 4-1: Location of the *DP*-based mobile crosshole seismic experiment; A) General site location (→ Figure 2-1); B) Location of the temporarily installed boreholes (S1 = 82 m, S2/R2/R4 = 92 m, R2/S4/S3 = 102 m, R3 = 112 m) and L/CPT-1.

## 4.2 Field site

For our investigation, we chose an abandoned meander oxbow structure, pre-selected using aerial imaging and on-site reconnaissance. We kindly refer the reader to chapter 2.1 for a general site description (Figure 2-1). The results of structural investigation via a combination of several non-invasive geophysical methods were discussed in Chapter 3 (Figure 3-7). We performed the *STT* in 10-m sections along the path (Figure 4-1).

## 4.3 Methods

### 4.3.1 Seismic traveltime tomography (*STT*)

*STT* generates and records elastic waves ( $\rightarrow$  Chapter 3.3.3) at various depths in boreholes or wells. Thus, P- and S-waves are measured between two points, which allows characterisation of the layer properties (LEHMANN, 2007). *STT* is a special application, aside from various other borehole seismic methods, e.g., *vertical seismic profiling (VSP)* or *single well imaging*. Here, the seismic source and the seismic receiver are positioned in two separate boreholes (borehole-to-borehole method). The tomographic approach is used, while simultaneously detecting the shot at depth *A* at different receiver positions  $B_1$ – $B_n$ . Generally, the strength of the source that can be placed in the borehole restricts this method, as it limits the distance over which the signals can be detected (TELFORD, 1990).

For *in situ* data acquisition of seismic signals, we used *DP*-methods to apply the seismic components (source and receiver) in temporarily installed boreholes – with the steel rod used as casing (Figure 4-2). The lateral distance between both locations was 10 m. In total, we performed three measurement sections (the middle part was measured twice in opposite directions), leading to a data set of a 30-m long profile (Figure 4-1).

The steel rods of the sonic sampling equipment used (URL 18) allow the application of a commercial seismic source. The inner diameter of these hollow steel rods is 7.70 cm (3.03 in). Before field operation, we prepared the ending rod (at source position) with vertical slots of 40-cm length in a 2-mm spread, in order to overcome the problems of the rod's rigidity and to transmit enough energy to the surrounding ground. Filling the slots with silicon avoids any backfill (fines) into the rods. For field installation, we pushed the rods with closed tips into the ground. As a source for the seismic experiment, we used an *electrodynamic borehole impactor* source (BIS-SH), manufactured by *Geotomographie GmbH*, Germany (URL 1). This device operates in both dry and water-filled boreholes and can be rotated using a single pipe string that contains all supply cables. A pneumatic clamping system mechanically couples the source to the borehole casing. Besides generation of SH-waves,

this source generates P-waves as well. Thus, S- and P-wave data can be simultaneously acquired.

For the temporary receiver hole, we used a *Geoprobe* hollow steel rod with an inner diameter of 6.67 cm (2.625 in) (URL 5), which was appropriate to utilise because of the smaller diameter of the receiver. We used two three-component borehole geophones, manufactured by *Geotomographie GmbH*, Germany (URL 2), installed with fixed 2-m spacing. Each geophone includes one vertical and two horizontal components, with an azimuthal spacing of 90°. At the geophone position 40 cm along the tip, we prepared the rod with vertical 30-cm slots in a 0.5-cm spread. Similar to the source hole, filling the slots with silicon helps avoid backfilling of fines into the rods. During operation, the receivers were pneumatically attached to the borehole casing to ensure proper coupling. A compass (located in the casing of the geophones) determines the orientation of the geophones in the rods.

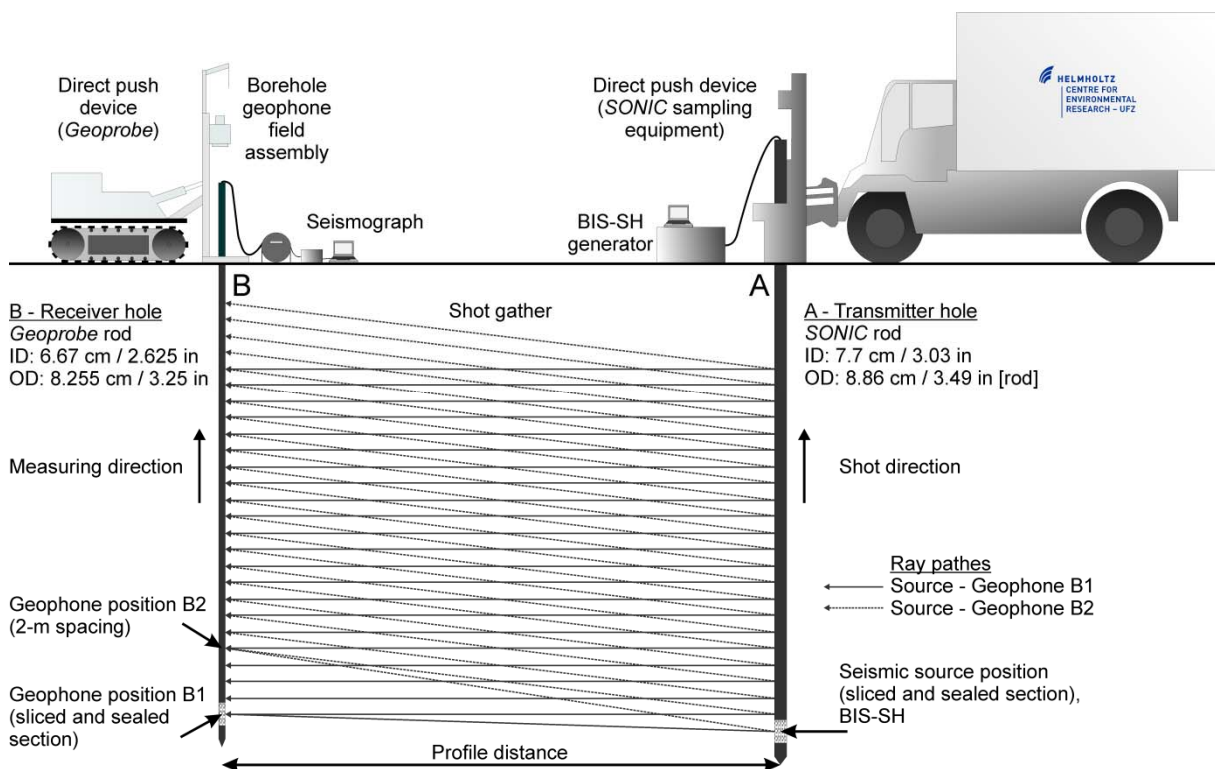


Figure 4-2: Experimental design, components, and exemplary shot gather of *DP*-based seismic travelttime tomography developed in the framework of the *MuSaWa*-project.

For our measurements, we used a 20.833- $\mu$ s sample interval. To reliably identify the first S-wave arrivals, we performed two reversely polarized shots perpendicular to the inter-borehole plane. Rotating the source by 180° achieves the reverse polarization. Polarisation of P-wave energy remains unaffected by this rotation, and thus, first arrivals of S-waves are identifiable in the recorded traces by comparing single polarities observed from both shots. Operating direction was from bottom to surface. After fixing the seismic source at position,

we performed shootings receiving the signals at the geophone positions (2-m spacing). Relocating to next shot position, we than pulled the source and receiver rods towards surface. The vertically shot and receiver spacing was 0.5 m. Thus, both were constantly relocating, which enabled us to take the shot gather, which is illustrated in Figure 4-2. After data acquisition, we pulled out the steel rods. Then we recorded the ground water level in the borehole with an electric contact gauge before sealing the remaining probing channel. The coordinates of the source and receiver borehole locations were measured using a total station, i.e., the accuracy of the positioning data lies in the cm-range.

### 4.3.2 Processing and model generation

We used an automatic picking routine (instantaneous phase follower) to determine P-wave traveltimes, implemented in the open-source software *OpenDTect* (URL 1). In contrast, S-wave traveltimes were obtained manually by comparing the bidirectional shots.

As a first approach, we used *GeoTomCG* software (*GeoTom LLC, USA* - URL 11) to perform simple source-to-receiver traveltimes analysis, calculating velocities for P- and S-waves. Subsequently, we performed a separate analysis for each wave type.

For traveltimes inversion, we used a *particle swarm optimization (PSO)* approach to jointly invert traveltimes (P- and S-wave). For a thorough description of the *PSO*-approach, the reader is referred to TRONICKE ET AL. (2011, 2012) and PAASCHE AND TRONICKE (2013). Here, we used layer-based model parameterisations as explained in the approach of ROY ET AL. (2005), where each interface is defined in two dimensions using a sum of arc-tangent functions (equation 4-1),

$$z(x) = z_0 + \sum_{j=1}^n \Delta z_j \left( 0.5 + \frac{1}{\pi} \tan^{-1} \left( \frac{x-x_j}{b_j} \right) \right) \quad (4-1)$$

where  $z$  is the depth,  $x$  the horizontal distance,  $n$  the number of arc-tangent nodes per interface,  $z_0$  the average depth of the interface,  $x_j$  the horizontal location of an arc-tangent node, and  $\Delta z_j$  the vertical throw attained asymptotically over a horizontal distance of  $b_j$ . The  $n$  was set to a value of 3. This provides enough flexibility to explain our recorded traveltimes data. Considering  $p$  as the number of interfaces defining  $p + 1$  constant velocity layers with two velocities (S- and P-wave), the model vector consists of  $7p + 2$  unknown parameters. In addition to the number of layers  $p$  and the number of nodes per layer  $n$ , we must also define reasonable search limits for each component of the model vector  $m$ , the number of particles, and reasonable stopping criteria for the traveltimes inversion problem. The performance of some initial parameter tests helped to find these parameters. For evaluation, i.e., establishing how well they fit the considered models, we sum the relative root-mean-square (rms) errors calculated between modelled and observed S- and P-wave traveltimes, respectively.

To calculate synthetic traveltimes on a layered velocity model using accurate, fast, and robust methods (such as finite-difference eikonal solvers), we must discretise the interfaces (defined by equation 4-1) on a regular grid. The geometry of the interfaces is accurately represented by the grid node spacing. Here, we used a 0.1-m grid node spacing for the  $x$ - and  $z$ -axis directions. The forward problem of gridded velocity models was solved using the eikonal solver (implemented in the *Madagascar* open-source software package (URL 14), which is based on the fast-marching method, e.g., SETHIAN (1996), FOMEL (1997), and SETHIAN AND POPOVICI (1999).

### 4.3.3 Calculation of geotechnical parameters from seismic velocities

Direct translation of the P- and S-wave models allows the calculation of rock parameter models. Thus, we derived the velocity ratio  $v_P/v_S$ , the P-wave modulus  $M$ , the shear-modulus  $\mu$ , the Poisson's ratio  $\sigma$ , the Young's modulus  $E$ , and the Bulk modulus  $K$  to describe the elastic properties of the homogeneous and isotropic media (SCHÖN, 1998; WITT, 2008). In addition, we calculated the pore percentage  $n$  and the pore number  $e$ , which, furthermore, can be used to calculate gravimetric water content  $\omega$ , e.g., WITT (2008).

All aforementioned parameters depend on the sediment density  $\rho$ . As the density  $\rho$  is unknown, we used the empirical approach of TEZCAN ET AL. (2006) to calculate the unit weight  $\gamma_P$ , which is related to the gravitational acceleration  $g$  and density  $\rho$  by equation 4-2. We can directly calculate the weight using the empirical equation 4-3. The unit weight  $\gamma_P$  is estimated from P-wave velocity  $v_P$  in m/s that we obtained in the traveltimes models. Hence, the calculated values for weight and, therefore, density information refers to each data point in the model.

$$\rho = \frac{\gamma_P}{g} \quad [\text{g/cm}^3] \quad (4-2)$$

$$\gamma_P = \gamma_0 + 0.002v_P \quad [\text{kN/m}^3] \quad (4-3)$$

The unit weight  $\gamma_P$  (related to P-wave velocity by equation 4-3) furthermore reflects *in situ* conditions, since it also considers the water content in saturated sediments. However, we have to distinguish between cohesive and non-cohesive layers, so as to make reliable use of the empirical parameter  $\gamma_0$  by shifting the linear regression on the  $y$ -axis. TEZCAN ET AL. (2006) obtained their reference unit values based on extensive case study investigations and laboratory testing. The authors provide a range of values from 16–20 kN/m<sup>3</sup> that reflect the increase in density of the investigated material. In this thesis, we only have to consider a  $\gamma_0 = 16$  (loose sandy, silty, and clayey soils) and a  $\gamma_0 = 17$  (dense sand and gravel) ( $\rightarrow$  Chapter 3). We used a layer-based approach for weight calculation. Therefore, in order to define a layer boundary, we used P-wave velocity. We assume the upper or first layer, which

is a haugh, to have a P-wave velocity less than 1,500 m/s, whereas all velocities above this value represent the underlying sandy to gravelly (second) layer.

Since the unit weight  $\gamma_p$  is related to density by gravitational acceleration ( $g = 9,81 \text{ m/s}^2$ ), we can insert the form, equation 4-2, of the density  $\rho$  into the equations for P-wave modulus  $M$  (equation 4-4), shear modulus  $\mu$  (equation 4-5), Young's modulus  $E$  (equation 4-6), and Bulk modulus  $K$  (equation 4-7). These moduli are used for measuring the stiffness of materials. All describe the response of the material to certain forms of stress and strain (P-wave modulus to the ratio of axial stress to axial strain in a uniaxial strain state, shear modulus to shearing strain, Young's modulus to linear strain, Bulk modulus to uniform pressure), e.g., SCHÖN (1998). This approach also considers the water saturation of the investigated soils (UYANIK, 2011). All calculations are estimates because they are defined for homogeneous and isotropic materials.

$$M = \gamma_p \cdot \frac{v_p^2}{g} \quad [\text{MPa or GPa}] \quad (4-4)$$

$$\mu = \gamma_p \cdot \frac{v_s^2}{g} \quad [\text{MPa or GPa}] \quad (4-5)$$

$$E = 2 \left( \gamma_p \cdot \frac{v_s^2}{g} \right) \cdot (1 + \sigma) \quad [\text{MPa or GPa}] \quad (4-6)$$

$$K = \frac{\gamma_p}{g} \cdot \left( v_p^2 - \frac{4}{3} v_s^2 \right) \quad [\text{MPa or GPa}] \quad (4-7)$$

Poisson's ratio  $\sigma$  is defined as the negative ratio of transverse to axial strain and varies in the range  $0 \leq \sigma \leq 0.5$ , where  $\sigma = 0.5$  ascribes a volume-resistant material. For normal consolidated sediments, the value varies in a range of 0.25–0.45, and for rocks between 0.15–0.3, e.g., SCHÖN (1998). Hence, the average of Poisson's ratio is 0.33 for  $v_p = 2 \cdot v_s$ . High values of Poisson's ratio ( $\sigma = 0.48$ ) are typical for saturated porous material (SCHÖN, 1998). We calculated Poisson's ratio  $\sigma$  following equation 4-8.

$$\sigma = \frac{v_p^2 - 2v_s^2}{2 \cdot (v_p^2 - v_s^2)} \quad [\text{dimensionless}] \quad (4-8)$$

We can further use the P- and S-wave models to estimate the gravimetric water content  $\omega$ . Therefore, we assume the unit weight  $\gamma_p$ , which is calculated from P-wave velocity, represents the unit weight under saturated conditions  $\gamma_r$ , since we are operating below the ground water table. The assumption  $\gamma_p = \gamma_r$  allows us to calculate the pore percentage  $n$  (equation 4-9) and the pore number  $e$  (equation 4-10). Here, the unit weight of water  $\gamma_w$  is  $9.81 \text{ kN/m}^3$ . An average value of solid weights  $\gamma_s$  of non-cohesive soils is  $26.5 \text{ kN/m}^3$ ,  $26.7 \text{ kN/m}^3$  for weak cohesive soils, and  $27\text{--}27.5 \text{ kN/m}^3$  for strong cohesive soils, e.g., PRINZ AND STRAUß (2006) and WITT (2008). Hence, we can calculate the gravimetric water content  $\omega$  from pore percentage  $n$  (equation 4-11) and/or pore number  $e$  (equation 4-12). These formulas are valid for saturated soils (WITT, 2008).

$$n = \frac{\gamma_s - \gamma_r}{\gamma_s - \gamma_w} \quad [\text{dimensionless}] \quad (4-9)$$

$$e = \frac{\gamma_s - \gamma_r}{\gamma_r - \gamma_w} \quad [\text{dimensionless}] \quad (4-10)$$

$$\omega = \frac{n}{1-n} \cdot \frac{\gamma_w}{\gamma_s} \cdot 100 \quad [\%] \quad (4-11)$$

$$\omega = e \cdot \frac{\gamma_w}{\gamma_s} \cdot 100 \quad [\%] \quad (4-12)$$

#### 4.3.4 Soil sampling (*SS*)

We accomplished drillings using *DP*-procedures, where high frequency vibrations (*SONIC*) and the weight of the mobile platform push the probe devices into the ground. As this is taking place, subsurface material fills a plastic tube. Thus, we obtain our probe core that can be subsequently analysed, e.g., LEVEN ET AL. (2011).

We used the core samples for ground truthing as well as for correlation of the sediment types so as to highlight any alterations in the measured geophysical properties. The core results were obtained from the site characterisation study described in the previous chapter – core sample L/SON-5 (→ Figure 3-7 in Chapter 3). Thus, we drilled four core sections each of 2-m length, leading to a final depth of 8 m. Then we described the core pull and classified it according to grain size composition. We expect that the results support the classification of the *STT* and *CPT*-findings.

#### 4.3.5 Cone penetration testing (*CPT*)

*CPT* detects *in situ* parameter that relate to lithology. While pushing the probe into the ground (at a constant rate of 2 cm/s), the probe measures the cone resistance  $q_c$  and the friction  $f_s$  at the tip and the cone sleeve, respectively. The cone resistance  $q_c$  is defined as being the total force acting on the cone divided by the projected area of the cone (VIENKEN, 2010). The sleeve friction  $f_s$  is defined as being the total force on the sleeve divided by the total area of the sleeve (LUNNE ET AL., 1997). Tip resistance  $q_c$  and sleeve friction  $f_s$  can be used to calculate friction ratio  $R_f$ , which is a proxy to be used for lithological interpretation (equation 4-13). For correction of the tip resistance  $q_c$ , we used data from *in situ* dynamic pore water pressure measurements  $u_2$  (measured behind the tip) to determine the corrected cone resistance  $q_t$  (equation 4-14). Pore pressure resistance correction normally eliminates significant differences that may arise from one cone design to another (LUNNE ET AL., 1997) and therefore the resulting data (the corrected cone resistance  $q_t$ ) can be used for interpretation. In this way, the *CPT*-method obtains high-resolution vertical profiles of different parameters that are related to lithology, e.g., DOUGLAS AND OLSEN (1981), JEFFERIES AND DAVIES (1991), ROBERTSON (1990, 2009), ROBERTSON ET AL. (1983, 1986), and

SCHMERTMANN (1978). BROUWER, (2007), LUNNE ET AL. (1997), and MEIGH (1987) provided a detailed description of *CPT*.

$$R_f = \frac{f_s}{q_t} \cdot 100 \quad [\%] \quad (4-13)$$

$$q_t = q_c + (1 + a) \cdot u_2 \quad [\text{MPa or GPa}] \quad (4-14)$$

The *CPT*-method has long since become a standard application used in geotechnical site characterisation in unconsolidated sediments. Cone penetration testing with pore pressure measurement (*CPTU*) is one of the most commonly used applications (LUNNE ET AL., 1997). Principally, electric *CPT* (including data transfer between probe and field computer) is *state-of-the-art*; however, purely mechanical *CPT*-systems are still available. The method is widely accepted and standardised, e.g., DIN EN ISO22476-1 (2009/10) and DIN EN ISO22476-12 (2009/10) (German Standard).

The *CPT/CPTU* probes can be applied as a stand-alone tool or also be coupled with other *DP*-tools, e.g., *SMP* (KIM ET AL., 2007; SHINN ET AL., 1998; → Chapter 6.2.3) that are likewise used for detecting electrical conductivity (*DP – EC*), *SeismicCPT* (ROBERTSON ET AL., 1992; SUZUKI ET AL., 1998) detecting additional seismic data, and optical sensors such as *VisCPT* (LEE ET AL., 2008). VIENKEN (2010) used *CPTU*-data to address hydraulic conductivity.

We used a heavy-duty subtraction-type piezocone designed by *Geomil Equipment BV.*, The Netherlands (URL 7). The projected tip area and the sleeve area are 15 cm<sup>2</sup> and 225 cm<sup>2</sup> in size, respectively. A data transfer cable connects the probe to the recording unit at the surface. This allows live monitoring of the obtained data and, therefore, onsite control while advancing the probe. For measuring pore water pressure  $u_2$ , the transmission element (foamed metal) which transfers the outer pressure to the sensor element (piezo transducer) must be saturated by a non-solidifiable medium, e.g., silicon oil.

## 4.4 Results

### 4.4.1 Quality of seismic data

The lateral distance between both locations was 10 m. In total, we performed three sections, leading to a data set of a 30-m long profile (Figure 4-1). The recorded traces differ in quality. Figure 4-3 shows the recorded traces of the reversely polarized shots at the lower geophone position (B1 - sliced section) from 82–92-m profile section. In the lower section of the profile, we can obtain good quality data, where P- and S-wave first arrivals are clearly identifiable. Towards the surface, data quality decreases for S-wave arrivals, and also in the

upper section for P-wave arrivals. Generally, data quality differs along the different recorded profile sections.

Figure 4-4 shows the results from simple source-to-receiver traveltimes analysis for (A) P-wave and (B) S-wave velocity along the entire recorded profile. By means of illustration, we chose classed-post-map data to plot the velocity pattern. Areas that represent less than five ray pathes (low coverage) are indicated by triangles. This information is however uncertain. Nonetheless, we managed to obtain good coverage for P-waves along all sections of the profile. However, for S-wave velocities, we obtained lower data density due to selecting fewer arrivals. There was no data available for the upper part (>7 m depth) of the 82–92-m profile section. The tomograms show P-wave and S-wave velocities from 900–2000 and 100–300 m/s, respectively. We can observe a layer structure with layer boundaries at 3 m, 3–6.5 m, and  $\pm 9$ -m depths. However, due to missing data and rough spatial resolution, a detailed interpretation of the layer structure is challenging.

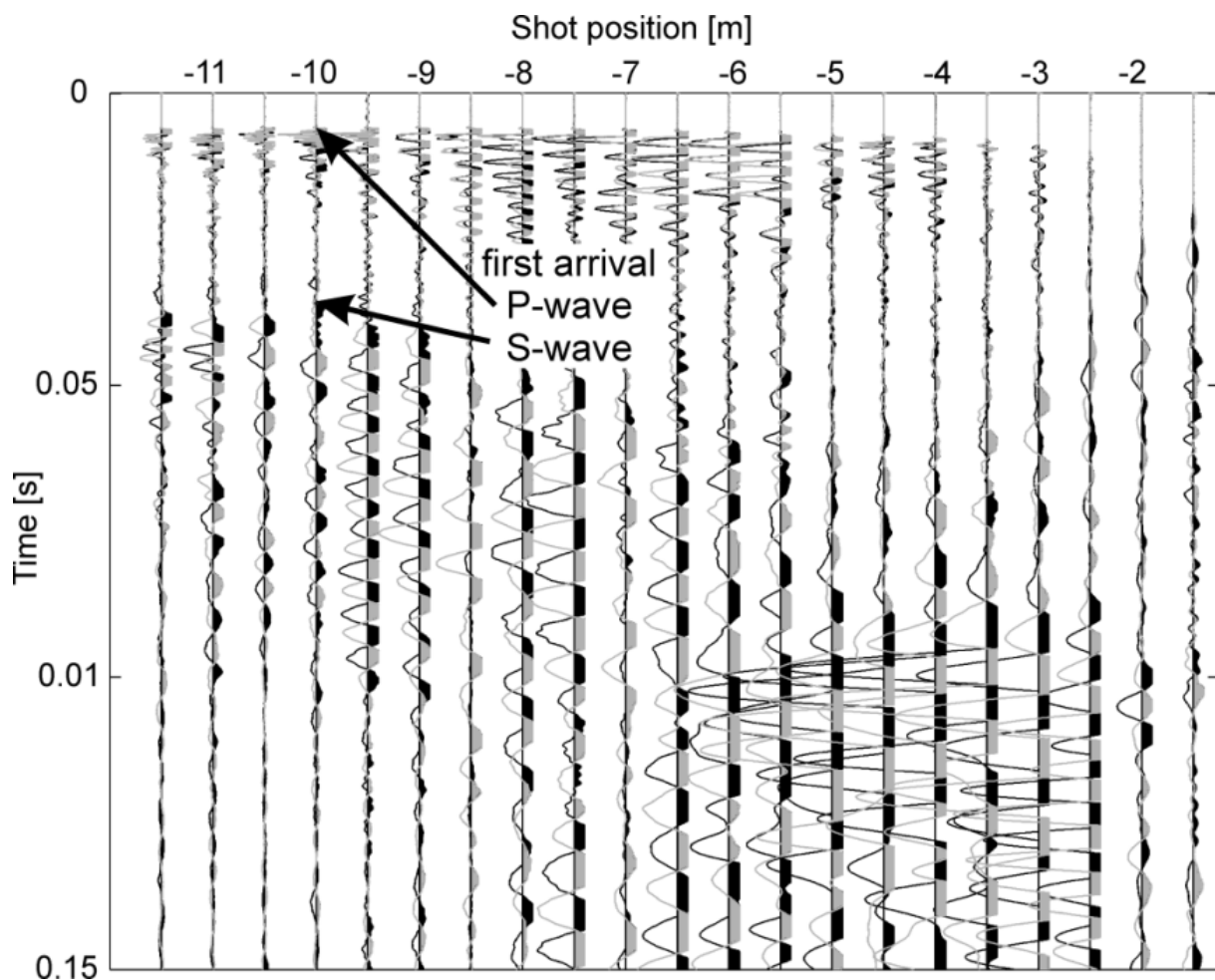


Figure 4-3: Example of recorded seismic traces from 82–92-m profile section (reversely polarized shots); geophone B1 position = shot position +0.2 m ( $\rightarrow$  Figure 4-2).

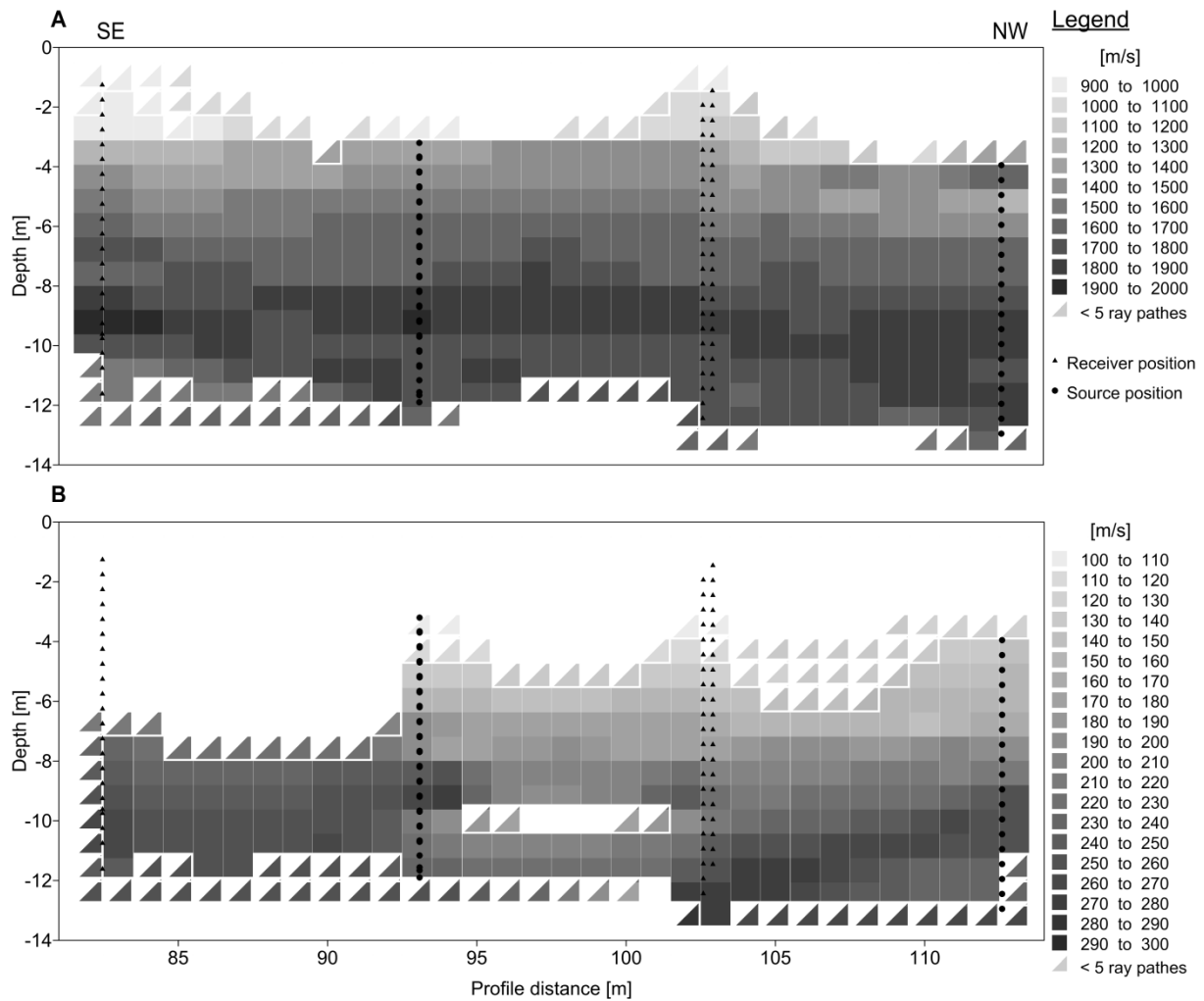


Figure 4-4: Source-to-receiver traveltimes analyses for (A) P-wave  $v_p$  and (B) S-wave velocity  $v_s$ ; proportion horizontal to vertical section 1:2.

Figure 4-5 and Figure 4-6 show the model ensembles from joint *PSO*-inversion for P-wave and S-wave velocity in terms of statistical variations. The subplots A, B, C, and D provide the  $Q1$  ( $Q_{0.25}$  = 25 % of the data), the  $Q2$  ( $Q_{0.5}$  = 50 % = median of the data), the  $Q3$  ( $Q_{0.75}$  = 75 % of the data), and the relative error  $f$  calculated according to equation (4-15), respectively.

$$f = \frac{Q3-Q1}{Q2} * 100 \quad [\%] \quad (4-15)$$

In total, 110 acceptable models were used, where each model explains travel time data equally well. Shot and receiver positions were marked. The data errors obtained vary from between 0.16–0.29 ms ( $v_p$ ) and 1.8–3.3 ms ( $v_s$ ), respectively. Thus, the sum of the relative root-mean-square (rms) errors calculated between modelled and observed S- and P-wave traveltimes is <0.24 ms and <2.613 ms, respectively. Hence, the errors for both seismic velocity models differ by one degree of magnitude.

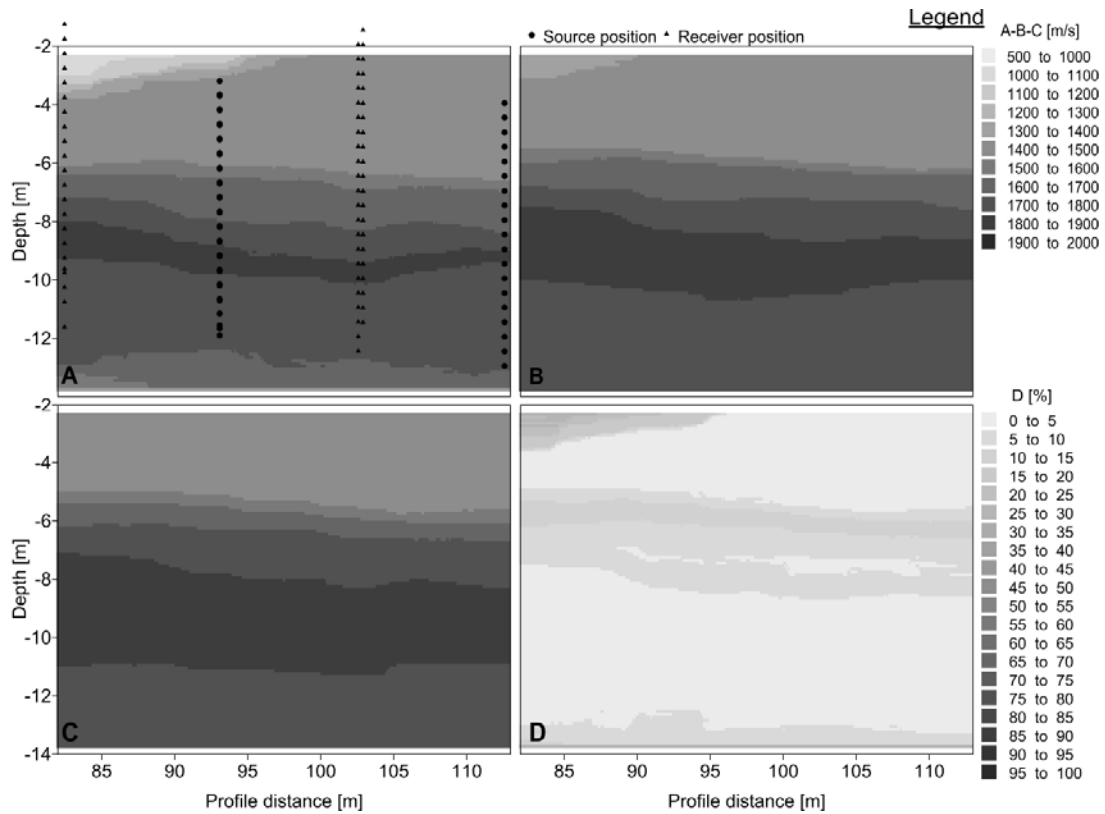


Figure 4-5: P-wave velocity  $v_p$  model ensemble from *PSO*; A)  $Q_1$ ; B)  $Q_2$ ; C)  $Q_3$ ; D) relative error  $f$ ; proportion of horizontal to vertical section 1:2.

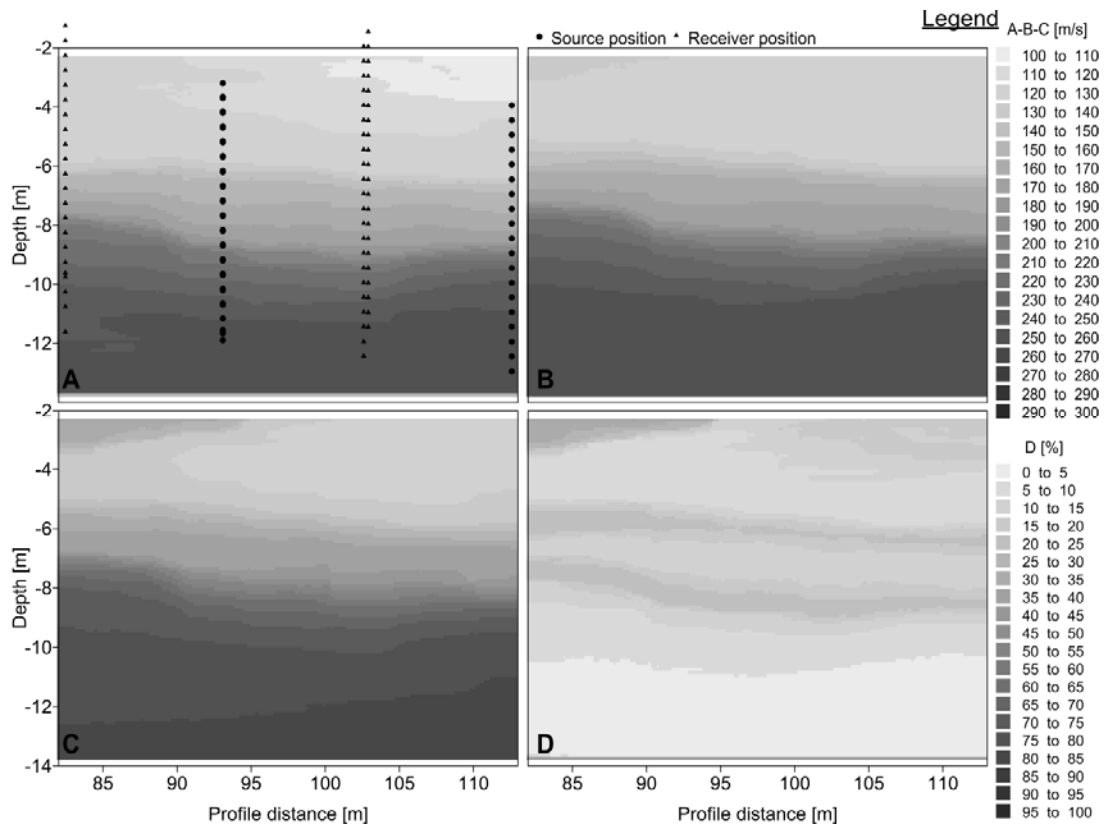


Figure 4-6: S-wave velocity  $v_s$  model ensemble from *PSO*; A)  $Q_1$ ; B)  $Q_2$ ; C)  $Q_3$ ; D) relative error  $f$ ; proportion of horizontal to vertical section 1:2.

The velocity models for P- and S-wave data show a layered structure (Figure 4-5; Figure 4-6). The calculated quantiles ( $Q1$ ,  $Q2$ ,  $Q3$ ) allow us to make an uncertainty appraisal of the data. Thus, the relative error is high at layer boundaries, reflecting this transition zones. In the P-wave velocity ensemble (Figure 4-9), we obtain high variations in the upper part (above 4-m depth) and the lowest part (>12-m depth). Here, the *PSO*-approach reconstructs  $v_p$ -values. However, in the aforementioned sections, data availability is generally low (compare with Figure 4-4). Subsequently, the reconstructed data show higher variations in these sections. Similar to the  $v_p$ -values, also  $v_s$ -data show high variations due to missing coverage in the denoted sections. As shown before, no data is available in the upper part (>7 m depth) of the 82–92-m profile section. Consequently, the S-wave velocities that are observable in the *PSO*-model ensemble are reconstructed. Lack of prior information in this area leads to the creation of artefacts, providing a *false* structure which is characterised by a strong decrease of velocities in this part of the profile. Hence, the jointly inverted P- and S-wave velocities and parameters calculated thereof should be critically analysed in the section above 4-m and below 12-m depths. Figure 4-7 (plotting the velocity ratio  $v_p/v_s$ ) shows the highest variations in the aforementioned sections, therefore supporting the error discussion.

#### 4.4.2 Geotechnical parameters from seismic velocities

For calculation of the unit weight from P-wave velocity  $\gamma_p$  according to TEZCAN (2006), we define the layer boundary between the upper haugh and the alluvial sediments (known from previous study; → Chapter 3), along the 1,500 m/s P-wave velocity (Figure 4-8). Based on the weight distribution, we calculated the elastic moduli from jointly inverted P- and S-waves as two-dimensional cross sections. Figure 4-9, Figure 4-10, Figure 4-11, Figure 4-12, and Figure 4-13 plot the P-wave modulus  $M$ , the shear modulus  $\mu$ , the Young's modulus  $E$ , the Bulk modulus  $K$ , and the Poisson's ratio  $\sigma$ , respectively. The calculated quantiles ( $Q1$ ,  $Q2$ ,  $Q3$ ) allow us to perform an uncertainty appraisal of the data, presenting the lower and upper range of the modelled data. Furthermore, each plot contain an estimation of the relative error  $f$ . In addition, Figure 4-14 presents the calculated gravimetric water content  $\omega$ . As described in the method section, the initial value of the solid weight  $\gamma_s$  differs in dependence of the cohesion of the soil (PRINZ AND STRAUß, 2006). Here, we can calculate this using intermediate value of 27 kN/m<sup>3</sup>.

All plots show layer structures. We obtain transition zones, which can be seen in the relative error and occur in 5–7- m and 7–9-m depths. These vertical shifts are smaller for each quantile, generally increasing from  $Q1$  to  $Q3$ . We obtain the most dominant layer boundary for water content data, representing the transition from upper haugh to lower alluvial sand/gravel. Thus, we can delineate five layers in the cross sections.

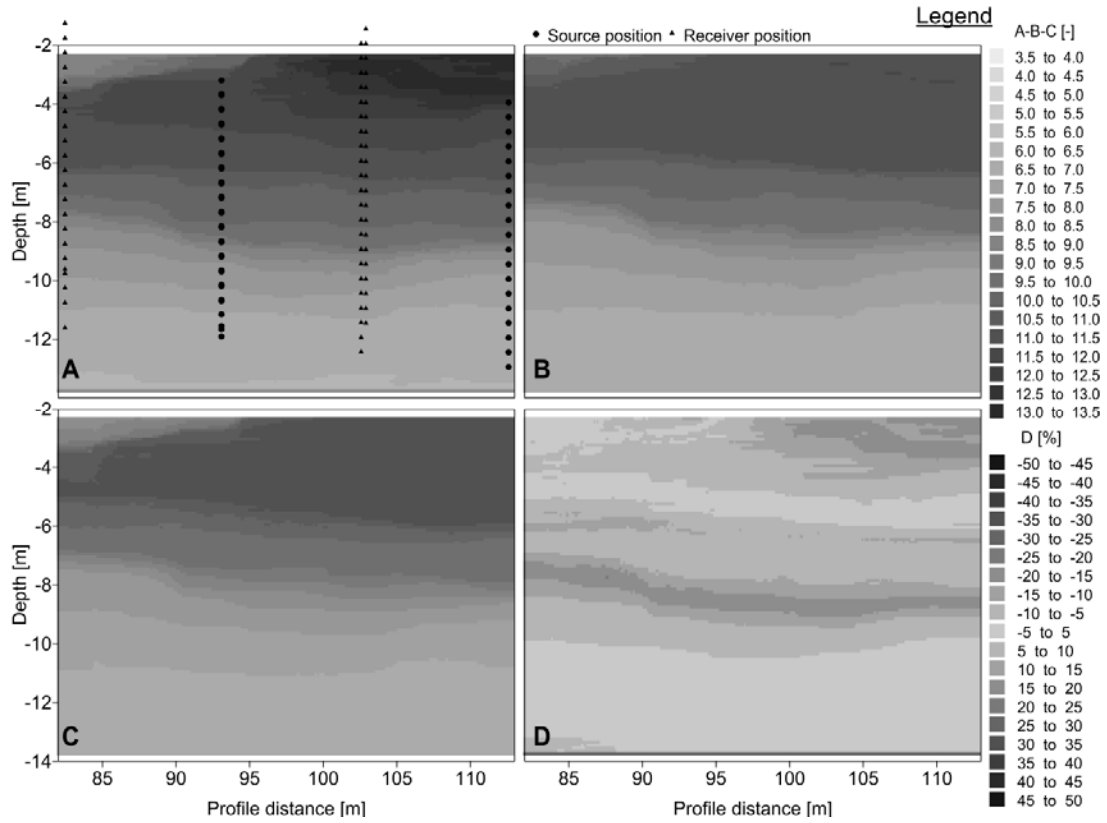


Figure 4-7: Velocity ratio  $v_p/v_s$  model ensemble from *PSO*; A) Q1; B) Q2; C) Q3; D) relative error  $f$ ; proportion of horizontal to vertical section 1:2.

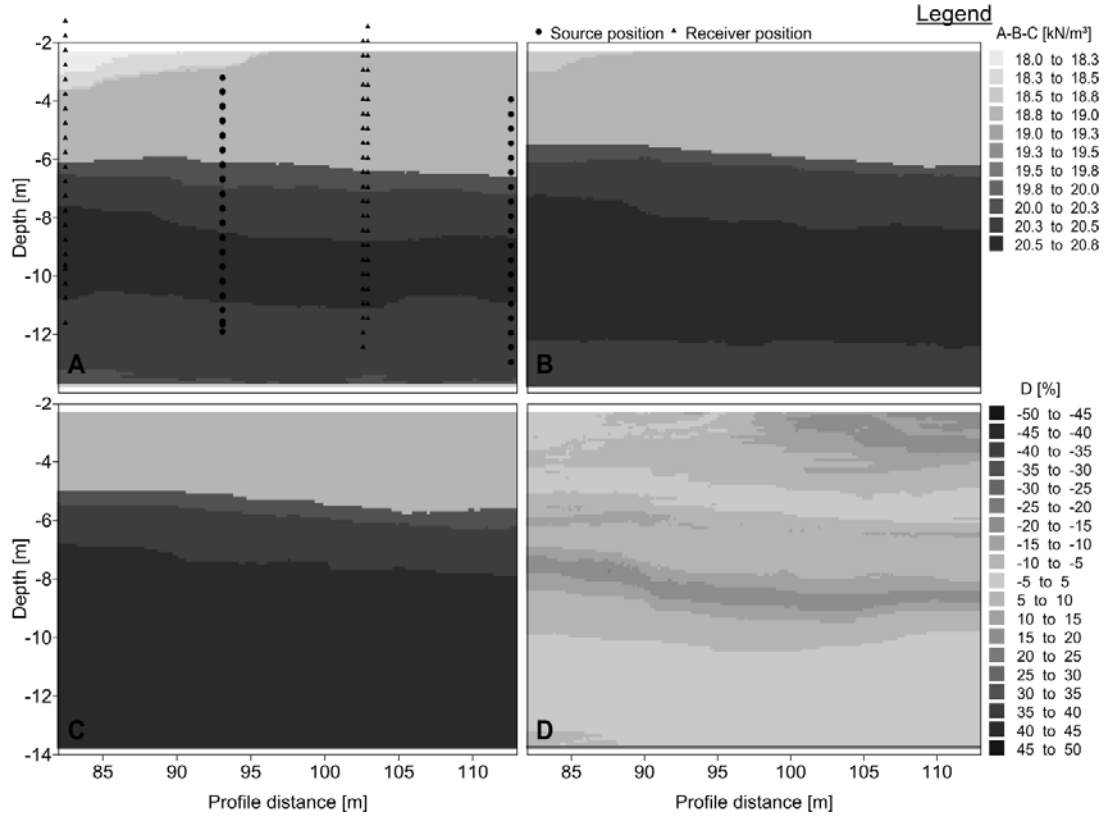


Figure 4-8: Solid weight  $\gamma_p$  model ensemble from *PSO*; A) Q1; B) Q2; C) Q3; D) relative error  $f$ ; proportion of horizontal to vertical section 1:2.

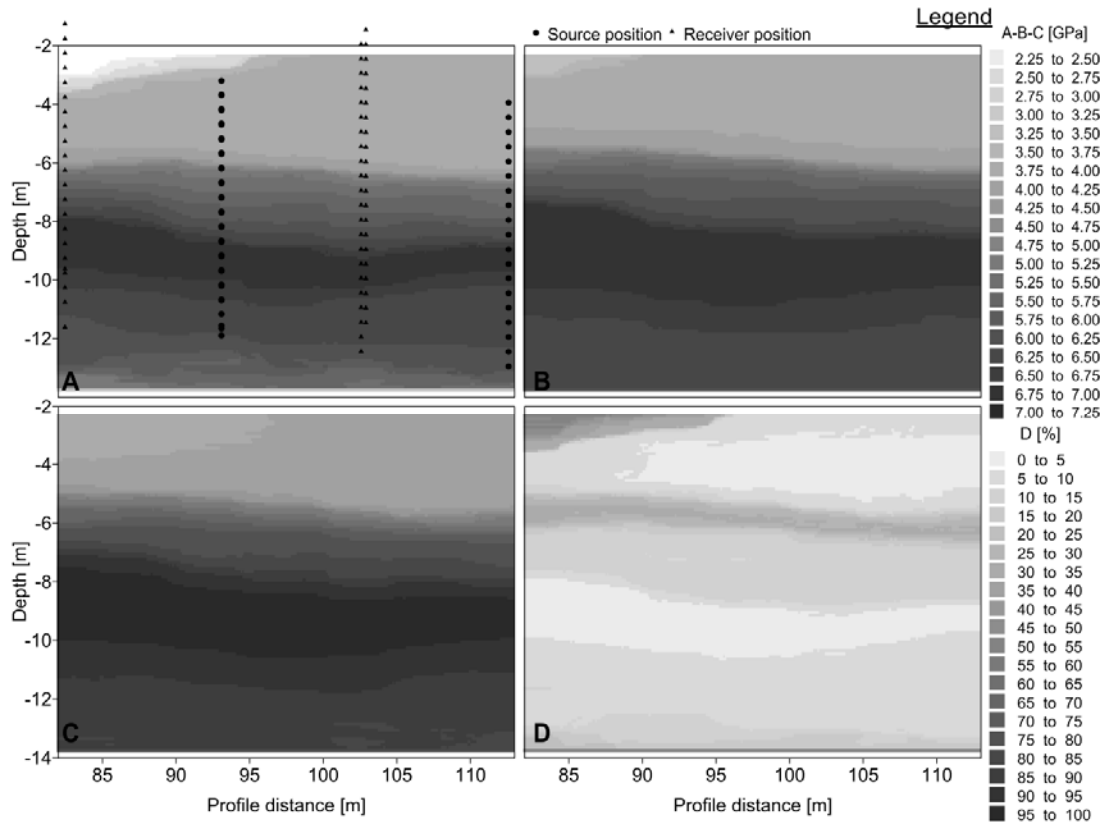


Figure 4-9: P-wave modulus  $M$  model ensemble from  $PSO$ ; A)  $Q1$ ; B)  $Q2$ ; C)  $Q3$ ; D) relative error  $f$ ; proportion of horizontal to vertical section 1:2.

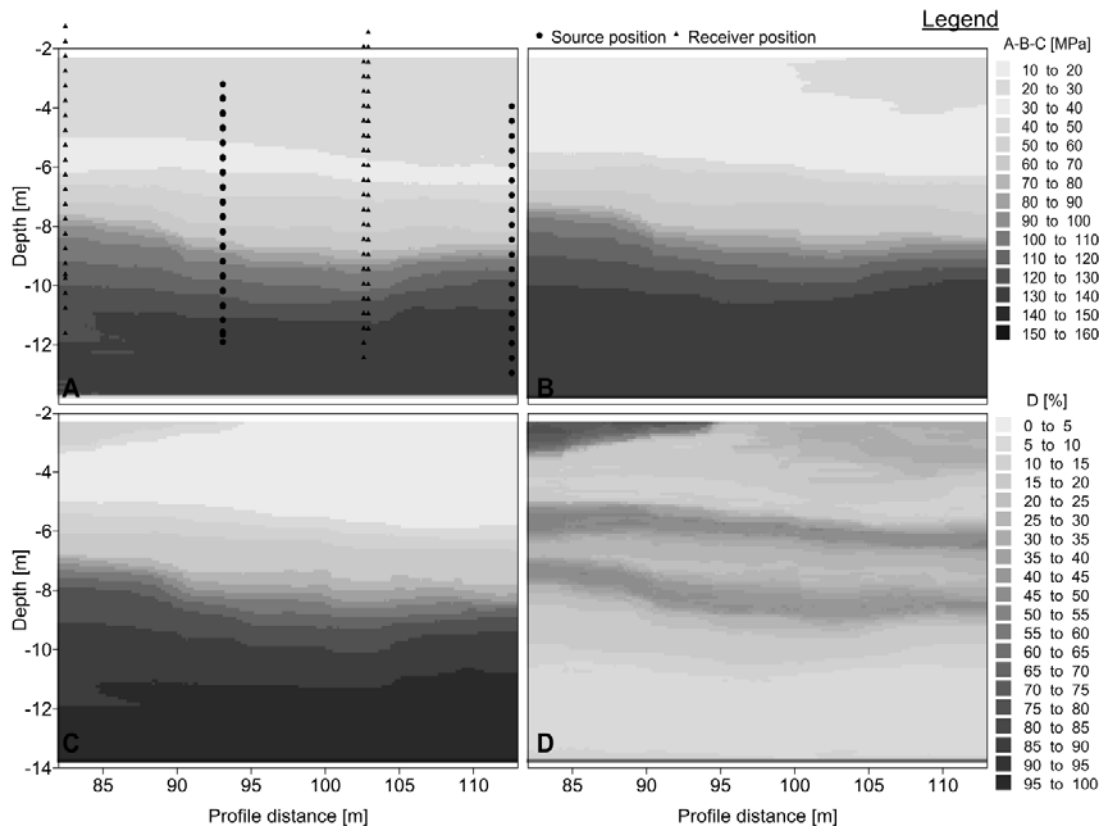


Figure 4-10: Shear modulus  $\mu$  model ensemble from  $PSO$ ; A)  $Q1$ ; B)  $Q2$ ; C)  $Q3$ ; D) relative error  $f$ ; proportion of horizontal to vertical section 1:2.

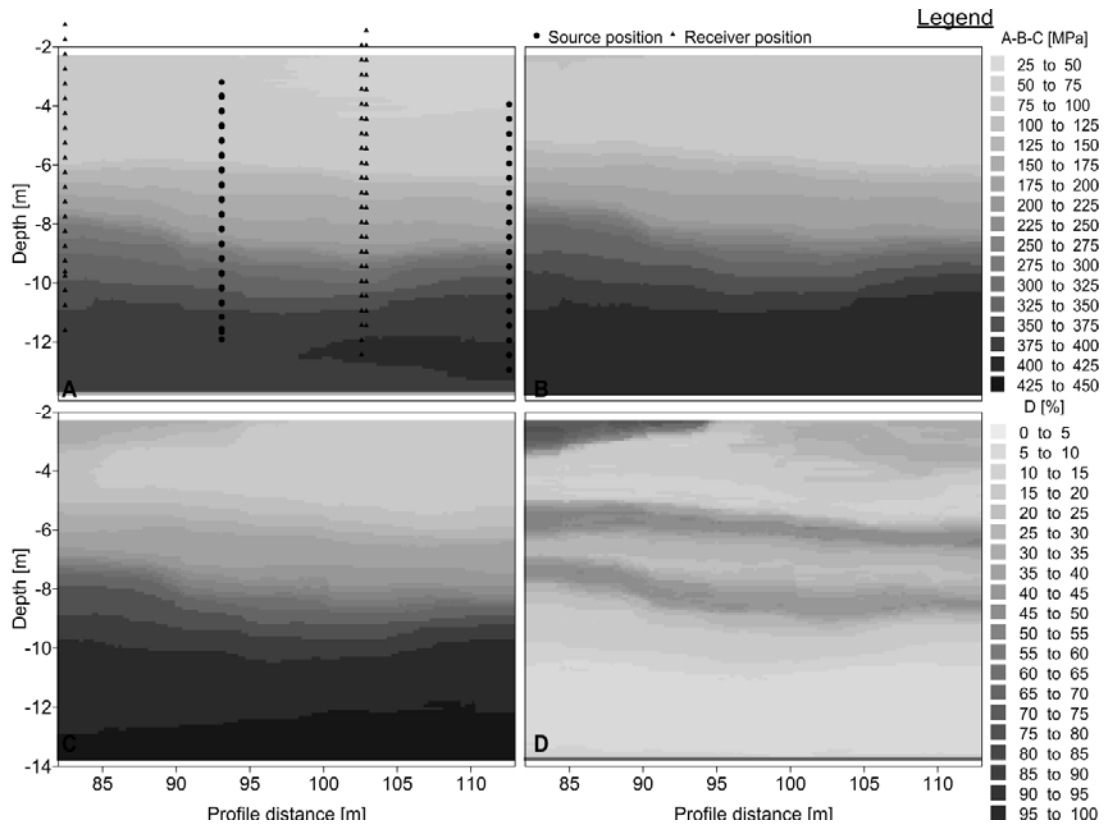


Figure 4-11: Young's modulus  $E$  model ensemble from  $PSO$ ; A)  $Q1$ ; B)  $Q2$ ; C)  $Q3$ ; D) relative error  $f$ ; proportion of horizontal to vertical section 1:2.

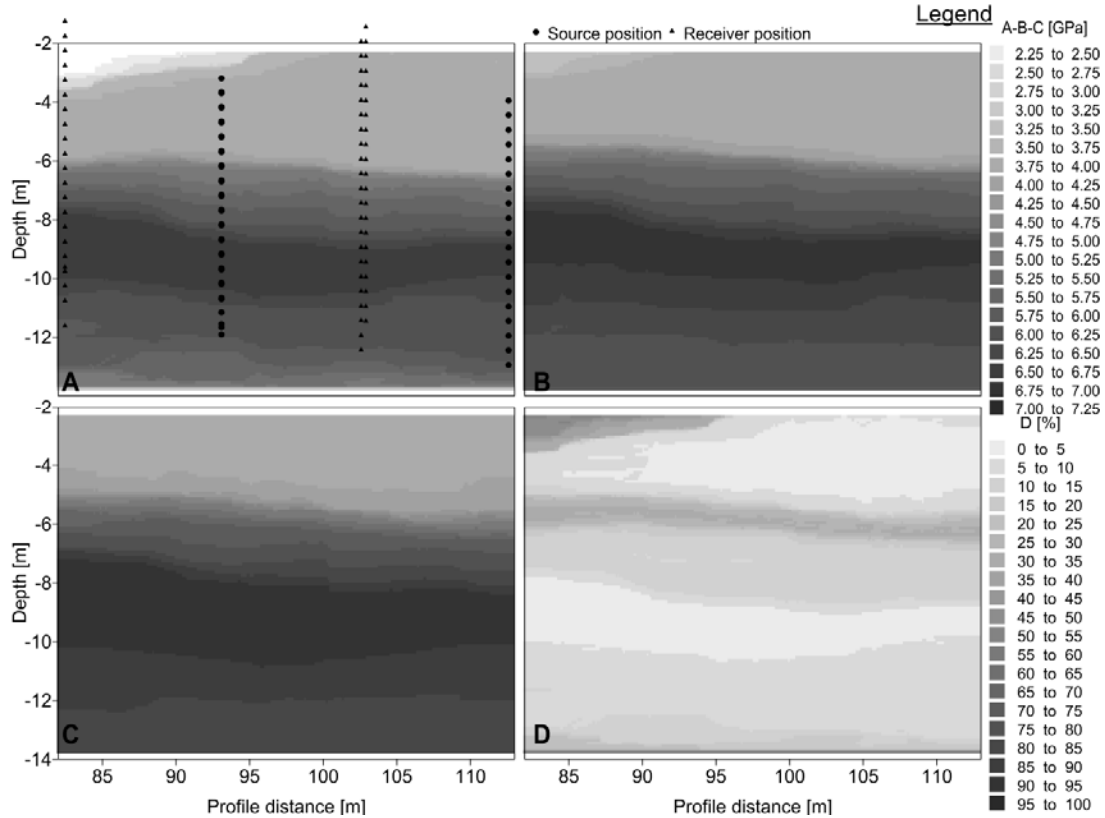


Figure 4-12: Bulk modulus  $K$  model ensemble from  $PSO$ ; A)  $Q1$ ; B)  $Q2$ ; C)  $Q3$ ; D) relative error  $f$ ; proportion of horizontal to vertical section 1:2.

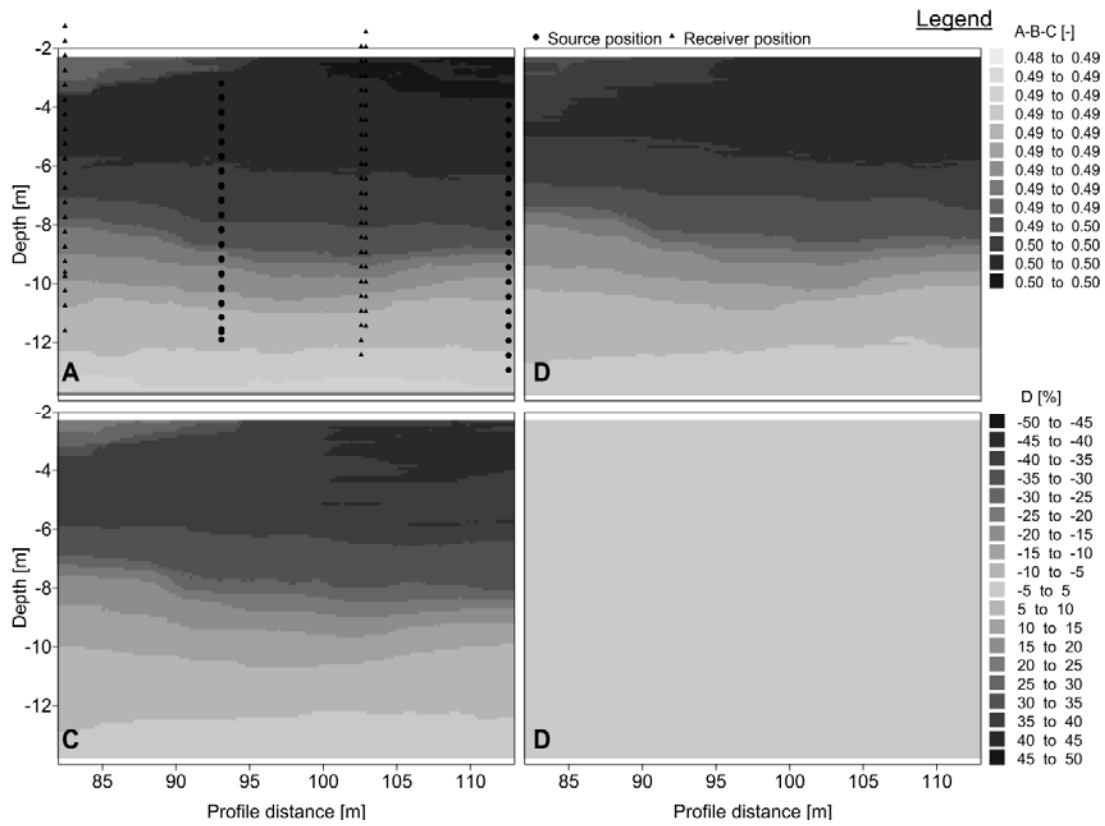


Figure 4-13: Poisson's ratio  $\sigma$  model ensemble from *PS0*; A) *Q1*; B) *Q2*; C) *Q3*; D) relative error  $f$ ; proportion of horizontal to vertical section 1:2.

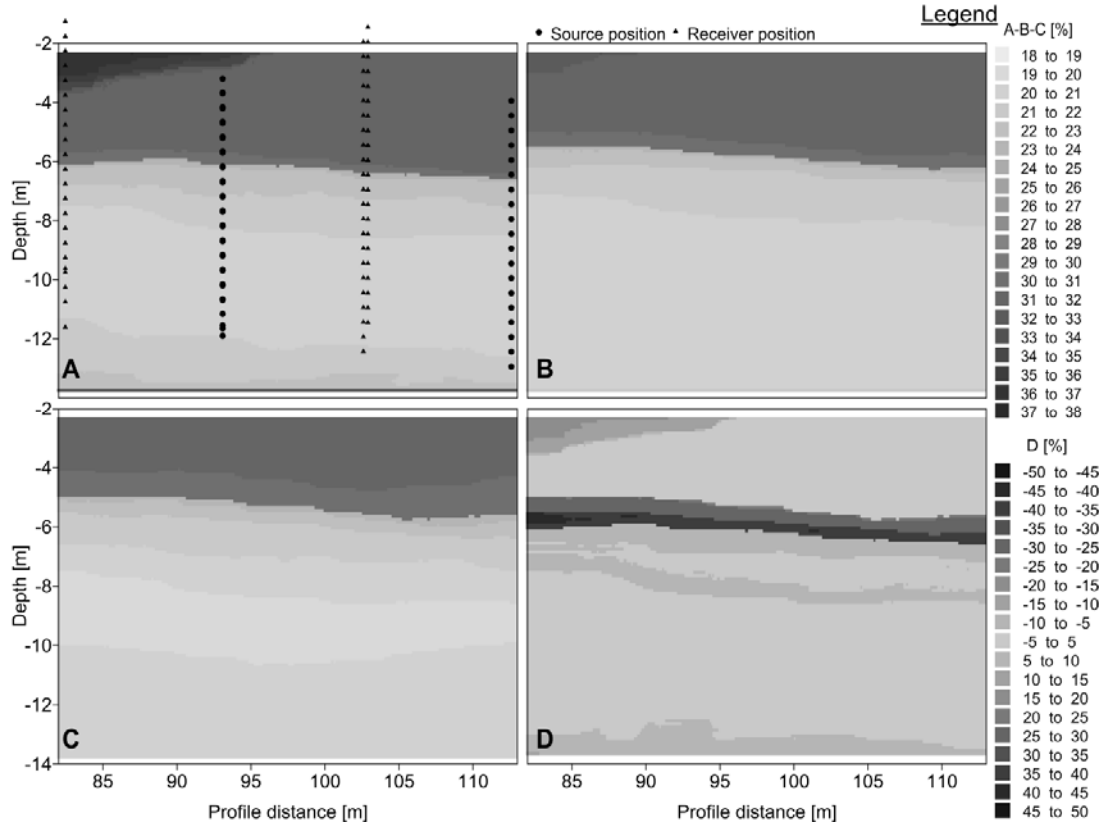


Figure 4-14: Gravimetric water content  $\omega$  model ensemble from *PS0*; A) *Q1*; B) *Q2*; C) *Q3*; D) relative error  $f$ ; proportion of horizontal to vertical section 1:2.

#### 4.4.3 Comparison of obtained velocities with soil sampling (SS) and CPT

We obtained several layers in the soil samples (L/SON-5; Figure 4-15A) for the first 8-m depths. The first 2 m of the profile are dominated by sandy silt to silty sand. From 2-m depth onwards, we have evidence of the presence of silty fine sands. At 3.4-m depth, a boundary between silty fine sand to fine-to-coarse sand can be observed. At 5.7-m depth, a shift from fine sand to gravelly coarse sand is observable, introduced by a 0.3-m thick layer of fine gravel (5.7–6.0 m).

Interpretation of the corresponding CPT-log (L/CPT-1; Appendix B) according to ROBERTSON ET AL. (1986) also shows a clear layering structure (Figure 4-15A,B). We could obtain more precise data in the CPT-log (useful for interpretation with regard to lithology), due to constant logging. In total, five layers are represented and are listed by depth and substrate in Table 4-1. Thus, the results allow a delineation of the geology of the aforementioned five layers. Layers 1 and 2 are mainly composed of weak cohesive soils that are (1) sandy silt to silty clay and (2) sensitive fine-grained material, respectively. The first decimetre of layer 1 represents construction material from the dike path. The lower parts of layers 1 and 2 correspond to haugh sediments.

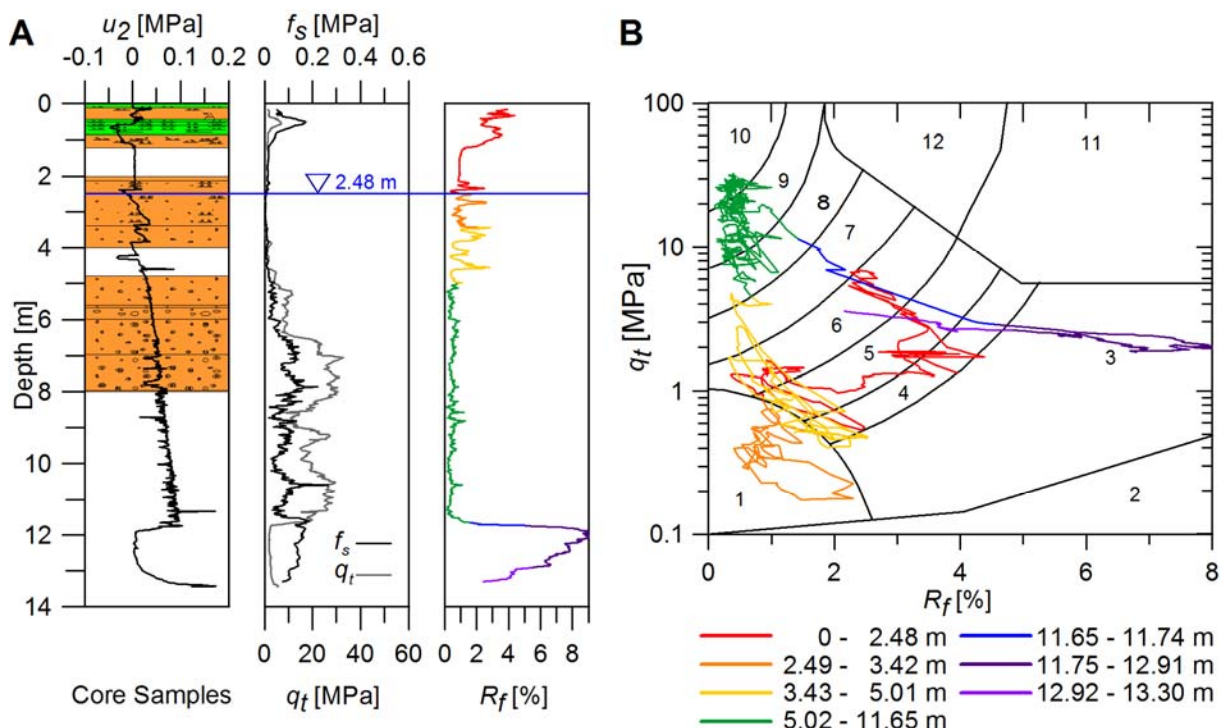


Figure 4-15: Results from CPT (L/CPT-1) and SS (L/SON-5); A) Dynamic pore water pressure  $u_2$ , sleeve friction  $f_s$ , corrected cone resistance  $q_t$ , and friction ratio  $R_f$  (color coded to interpretation in B) and core results (green = silt, orange = dominantly sandy, white = core loss/no data); groundwater level in borehole at 2.48 m depth; B) Colour coded lithological interpretation from ratio between corrected cone resistance  $q_t$  and friction ratio  $R_f$  according to ROBERTSON ET AL. (1986); 1 - sensitive fine grained, 2 - organic material, 3 - clay, 4 - silty clay to clay, 5 - clayey silt to silty clay, 6 - sandy silt to clayey silt, 7 - silty sand to sandy silt, 8 - sand to silty sand, 9 - sand, 10 - gravelly sand to sand, 11 - very stiff fine grained\*, 12 - sand to clayey sand\* [\*over-consolidated or cemented].

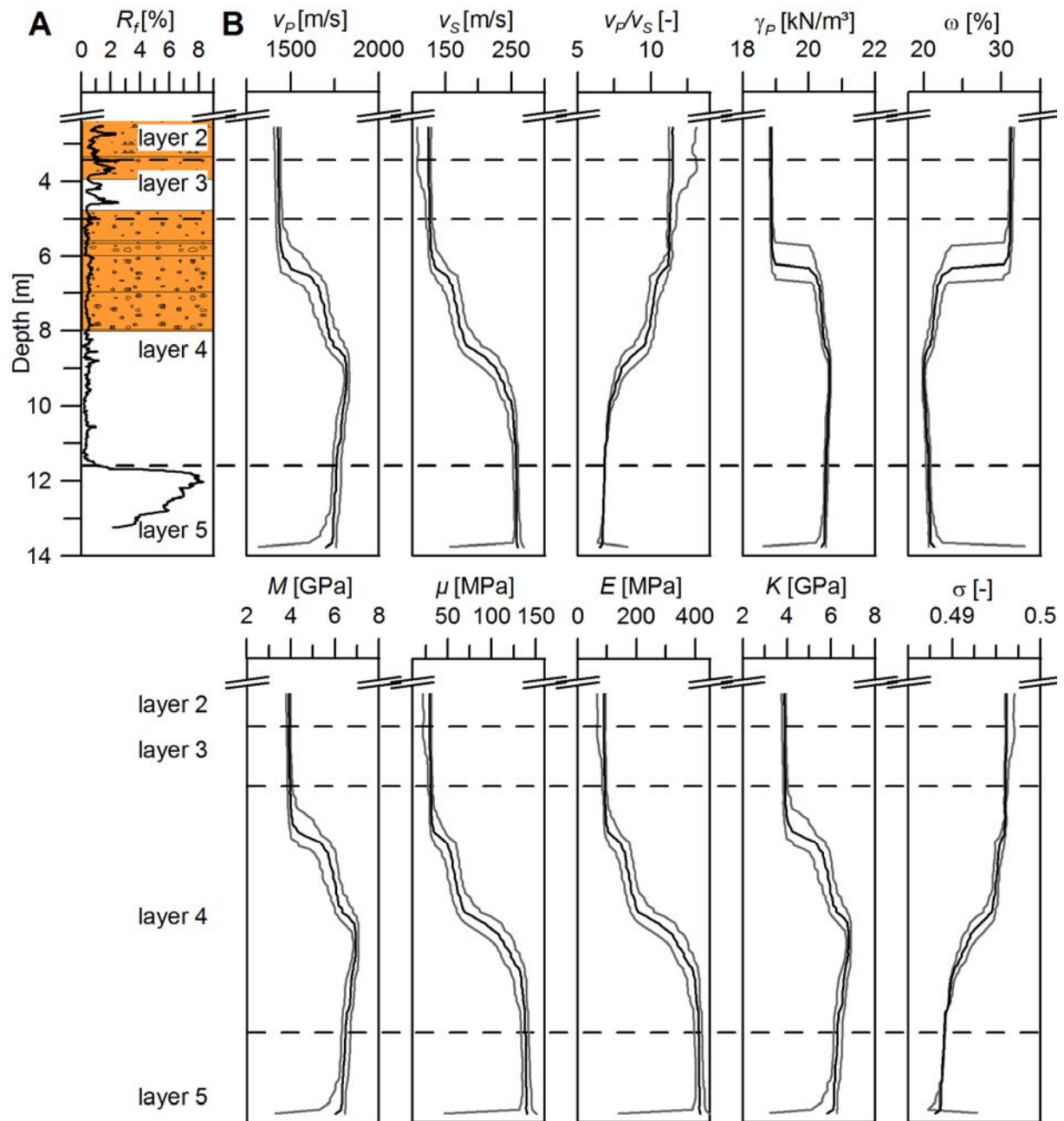


Figure 4-16: A) L/CPT-1-log (friction ratio  $R_f$ ) and core results from sonic drilling (L/SON-5) indicating the found layers (Table 4-1); B) One-dimensional profiles of geotechnical parameters calculated from jointly inverted P/-waves ( $PSO$ ) given as  $Q2$  (black line),  $Q1$  and  $Q3$  (grey lines): P-wave velocity  $v_p$ ; S-wave velocity  $v_s$ ; velocity ratio  $v_p/v_s$ ; unit weight from P-wave velocity  $\gamma_p$ ; gravimetric water content  $\omega$ ; P-wave modulus  $M$ ; shear modulus  $\mu$ ; Young's modulus  $E$ ; Bulk modulus  $K$ ; Poisson's ratio  $\sigma$ ;

Table 4-1: Geological setup at Löbnitz test site derived from CPT-log L/CPT-1(interpreted according to ROBERTSON ET AL. (1986) - Figure 4-15).

| No. | Depth [m]   | Substrate                                 |
|-----|-------------|---|
| 1   | 0-2.48      | sandy silt – silty clay                   |
| 2   | 2.49-3.42   | sensitive fine grained                    |
| 3   | 3.43-5.01   | silty sand – clayey silt                  |
| 4   | 5.02-11.65  | gravelly sand – silty sand                |
|     | 11.66-11.74 | silty sand – silty clay (transition zone) |
| 5   | 11.75-12.91 | clay                                      |
|     | 11.92-13.30 | silty clay – sandy silt (transition zone) |

*CPT*-log interpretation shows a third layer between depths of 3.43–5.01 m that is mainly composed of silty to clayey sand. This sand layer corresponds to alluvial materials with varying amounts of fines present. Beneath this layer, a sharp boundary to layer 4 can be observed. Here, the material is coarser. According to methods outlined by ROBERSON ET AL. (1986), it is possible to describe the material as silty to gravely sand. The sediments of layer 4 span from alluvial sand to bench gravel. However, a sharp boundary between these types of coarse material is not observable in the friction ratio log. Finally, we find very fine material beneath these layers between depths of 11.75–12.91 m. This fifth layer is composed of clay (tertiary clay). The boundary to the aforementioned coarse material is shaped in the form of a transition zone, which shifts from fine to coarse material in a depth range of 8 cm (11.66–11.74 m). Beneath the clay at the end of the log, there are also indications of an opposite shift that can be interpreted as a secondary transition zone, found between depths of 11.92–13.30 m. Groundwater was measured at 2.48 m for both logs (L/SON-5, L/CPT-1; → Appendix B).

For ground truthing of the estimated geotechnical parameters from seismic models (Figure 4-8; Figure 4-9; Figure 4-10; Figure 4-11; Figure 4-12; Figure 4-13; Figure 4-14), we compared the co-located one-dimensional vertical profiles with results from *CPT* and *SS* (Figure 4-16). Here, we observed a good fit for the five soil layers. The presented values of the elastic moduli seem to be in an acceptable range (with regard to the obtained layers, previously known from *CPT*) when compared with those in the relevant literature, e.g., PRINZ AND STRAUß (2006) and WITT (2008). In addition, we see an increase in P- and S-wave velocity within layer 4. This corresponds to the boundary between upper alluvial sand and lower bench gravel. So, we can therefore define this boundary at around 7.6-m depth. However, the tertiary clay is not represented in the seismic velocities because of low data availability in this section of the profile.

## 4.5 Discussion

Mobile *DP*-driven joint acquisition of P-wave and S-Wave crosshole data is straightforward. To date, and especially for near-surface seismic experiments, P- and S-wave crosshole traveltime data has been acquired separately. Using this mobile approach, we are able to overcome the limitations caused by stationary boreholes. Furthermore, we can improve and further develop *state-of-the-art* surveys, e.g., ANGIONI ET AL. (2003) and LINDER ET AL. (2010), acquiring and recording P- and S-wave crosshole traveltimes in one single step.

Joint inversion using a *PSO*-approach helps to appraise uncertainties and ambiguities in data interpretation, due to the generation of various models, which explain traveltime data

equally well. However, visualization and interpretation of such model ensembles that are (or may be) comprised of several hundred plausible solutions is still challenging. Thus, analysis of data quality is essential and can reveal ray coverage and help delineate critical zones (where velocity data is blurry because of missing initial input data for reconstruction) of the model ensembles from the *PSO*-approach. This helps us to avoid misinterpretation of local high variations and artefacts.

The models (*Q1*, *Q2*, *Q3*) we obtained deliver reliable results with respect to information gathered using *SS* (*SONIC*) and *CPT*. Furthermore, the transformation into geotechnical parameters fits well with regard to the investigated layers, compared with literature values (PRINZ AND STRAUß, 2006; WITT, 2008). Here, we used P-wave velocity for calculation of density/weights according to TEZCAN ET AL. (2006). In combination with the application of layer-based model parameterisation according to ROY ET AL. (2005) for calculation of travelttime models by *PSO* and the approach from TRONICKE ET AL. (2011), we can increase the resolution and span of the calculated parameters.

Thus, minimally invasive *DP*-logs, e.g., core logs from sonic drilling, especially in combination with *CPT*, deliver high-resolution *in situ* information about lithology. This independently measured information allows stratigraphic interpretation to be made which can be used for ground truthing verification, to achieve a more detailed evaluation of the seismic models. Furthermore, *DP*-logs allow a reliability analysis of the calculated elastic moduli and water content to be performed, which is dependent on fixed equations and some preliminary assumptions (cohesion and weight). We assumed fixed solid unit weights to address the cohesive properties of the explored layers. However, this can be adjusted.

Generally, seismic data successfully images the obtained stratigraphy. The results correspond with stratigraphic exploration by geophysical methods (→ Chapter 3; HAUSMANN ET AL., 2013). However, the underlying tertiary clay (layer 5) is not represented in the seismic velocities. We assume that the reason for this is low model resolution in the deeper areas. Here, certain relevant input data is missing due to decreasing ray coverage.

The results of this chapter show that applied mobile *seismic travelttime tomography* (*STT*) for combined acquisition of P- and S-waves delivers very good data. These findings further support the ideas of DIETRICH AND TRONICKE (2009), PAASCHE ET AL. (2009), and GALLARDO (2007) and may be used as part of a detailed analysis such as a cluster analysis. For data acquisition and model generation for the unsaturated and saturated zone, a combination of the applied mobile *STT* with standard reverse vertical seismic profiling (PAASCHE ET AL., 2009) using surface-mounted geophones is suggested. However, data analysis may be more challenging when it comes to deriving data inversion functions and for calculation of geotechnical parameters, owing to scale variations of the methods.

*Postscript*

*The results of this chapter deliver detailed knowledge about geotechnical properties of the layers subsurface structures along a profile at the Löbnitz test site. Comparing DP-based in situ data (CPT) to the cross sections gathered from STT confirms the high potential of such techniques to be used for high-resolution geotechnical parameterisation. In this context, we recognise in situ-obtained soil colour (gathered with the DP-based colour logging tool – CLT) as a promising proxy for (geotechnical) site characterisation, which will be discussed in the next chapter.*

## 5 Processing of *in situ*-obtained soil colours (SC)

### Chapter Outline

*This chapter presents a new methodology for DP-based in situ SC-detection and processing of such data for rapid, precise, and in-depth characterisation of the near surface to be achieved using colour as a proxy basing on the manuscript HAUSMANN ET AL. (SUBMITTED). The chapter highlights are:*

- *The rapid and high-resolution DP-based in situ-colorimeter fills the gap between classical soil sampling and ex situ colour determination using colour charts, handheld colorimeter, and laboratory methods.*
- *Numerical transformation of in situ-obtained SC into colour surrogates for selected colour spaces provides a basis for data analysis.*
- *Wavelet transformation (WT) and cluster algorithm are applicable for data denoising increasing interpretation certainty of colour log data.*

### 5.1 Introduction

The determination of clear, depth-related layer profiles is common in *soil science* (VISCARRA ROSSEL ET AL., 2006). Classical measurements determine soil colours using colour charts, handheld colorimeter, or samples. Samples, for instance, are also in use for *ex situ* colour determination in the laboratory, e.g., BARRETT (2002). Hence, in order to obtain colour records, a need for direct access to the soil (ground) is essential in most cases. However, the location of a test pitting and/or dependence on free faces (either natural outcrops or anthropogenic free faces, e.g., in an open pit, etc.) limit the possibility of data acquisition in regard to investigation depth, accessibility, and acquisition time. On the other hand, soil colour measurements on core pulls may not reflect *in situ* conditions because of disturbed samples and/or changing chemical conditions.

The *colour logging tool (CLT)* (as we have named it) is a minimally invasive DP-based colorimeter device. The tool enables rapid, precise, and deep *in situ* detection. Initially, the CLT gathers high-resolution data. This data is equivalent to classical soil colour (SC) profiles. However, such classic profiles commonly provide less data per depth unit (low-resolution data). However, the CLT has the capacity to replicate certain applications of these classical approaches. Furthermore, the CLT-system combines the advantage of DP-platforms with high data acquisition accuracy. The method is flexible, enabling us to access hard-to-reach

areas of interest. The system was designed for rapid application. Compared with all other *in situ* SC-measurement approaches, this method reaches deeper investigation depths.

Unquestionably, local thin layering structures, inclusions, chemical processes, mineral composition, and other factors may cause high colour variation within the same stratigraphic unit or horizon. Hence, strong variations in detected values due to high-resolution data may lead to a false and/or an over-interpretation of the layering structure in the ground. Since the maximum detection limit we use is in the mm-range, data interpretation therefore becomes more challenging, since this corresponds with geologic parameters, e.g., grain size (2 mm = coarse sand). Against this background, every larger grain or aggregate represents either one or a series of equal values in the data set, as they pass the detection window of the probe. However, these pseudo-layers are not representative of the whole soil horizon or the layer in which they are embedded. Figure 5-1 illustrates this problem. The core pull from SS (T/DT-1; → Appendix B) shows the bandwidth of colours in the ground (related to layers and single grains), that cannot be interpreted from the corresponding vertical soil colour profiles. Hence, a need exists to develop an appropriate method of data processing, with the aim of downscaling (smoothing) high-resolution data so that resulting interpretation certainty increases.

The aim of this chapter is to develop a new data processing method which can be introduced as a reliable tool for characterisation of the near surface, e.g., in the vadose zone. Therefore, we tested the transferability of our raw data into reliable and comparable colour surrogates, applied data reducing strategies, and verified the chosen approach, according to repeatability of *in situ* SC-measurements with related soil sampling.

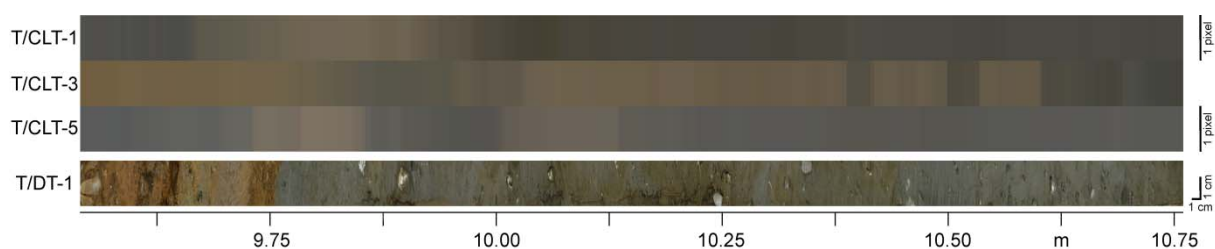


Figure 5-1: Comparison of raw data from vertical SC-profiles (T/CLT-80/1; T/CLT-80/3; T/CLT-80/5) to core pull (T/DT-1), investigation depth 9.54–10.76 m (total length: 1.22 m); core pull shows high vertical and lateral variation in the mm-scale (stretched to  $x$ -direction by factor 2.5 for better visualisation); *in situ* SC-measurements are given in RGB.

## 5.2 Background: optical-based site characterisation

For decades, SC has been used as a proxy for soil classification. This proxy is used as a criterion for stratigraphic differentiation, given its relationship with specific layer properties. Changes in the moisture content, for instance, influence the brightness and saturation of the colour. The chemical environment can also cause SC-changes, e.g.,

reddish-coloured sediments indicate the presence of iron-oxidative conditions, whereas grey colours are associated with reductive conditions. Furthermore, material components directly influence colour, e.g., the mineralogy and organic matter. All of those specifically-listed layer properties exhibit a spectral response in the visible range of the electromagnetic spectrum between wavelength values of 400–700 nm (MATHIEU ET AL., 1998; VISCARRA ROSSEL ET AL., 2006).

SHIELDS ET AL. (1966) and TORRENT AND BARRÓN (1993) have provided a general introduction to *SC*-measurements. SHIELDS ET AL. (1968) discussed the spectrophotometric measurement of *SC* and the relationship of those values to moisture and organic matter. FERNANDEZ AND SCHULZE (1987) developed procedures for soil colour detection of both dry and moist samples. THOMPSON AND BELL (1996) further investigated the influence of seasonal soil moisture on *SC*. EVANS AND FRANZMEIER (1988) described saturation/aeration changes (in loess and till) using *SC*-indices. MOKMA AND SPRECHER (1994) discussed *SC*-patterns, depth, and the duration of water tables in different sediments. BLAVET ET AL. (2000) further investigated these themes, comparing *SC*-changes with water well logs. POST ET AL. (2000) evaluated the influence of *SC* and soil moisture data to soil albedo. VAN HUYSSTEEN ET AL. (1997) used colour information to detect the occurrence of soil processes. PERSSON (2005) developed *SC*-image analysis for estimating surface soil moisture for different soil samples. PERSSON ET AL. (2005) tested soil-colour-photo-analysis techniques imaging the solute transport dynamics of dye tracers. SPERLING AND LAZAROVITCH (2010) used *SC* for the characterisation of water infiltration and redistribution in two-dimensional soil profiles.

HURST (1977) referred to the strong dependence of *SC* to iron content. Because of this, various laboratory studies investigated the influence of Fe-oxides and Fe-hydroxides on *SC* (BARRÓN AND TORRENT, 1986; FERNANDEZ AND SCHULZE, 1992; KOSMAS ET AL., 1984; SCHEINOST ET AL., 1998; SCHEINOST AND SCHWERTMANN, 1999; TORRENT ET AL., 1983). Then, SHUM AND LAVKULICH (1999) applied this knowledge using colour measurements to describe the oxidative processes in local mining.

Many scientists used *DP*-driven sensor systems for optical characterisation of the near surface. HRYCIW ET AL. (1998), HRYCIW AND SHIN (2004) and RASCHKE AND HRYCIW (1997) presented a coupled video camera and geotechnical probe known as a *vision cone penetrometer (VisCPT)*, which was applied by VAN DEN BOOGAART ET AL. (2002). This device records the sediment advancing the probe into the ground, detecting both mineral texture and the presence of hydrocarbon contaminants. For instance, LEE ET AL. (2008) used *VisCPT* to estimate grain sizes and calculate hydraulic conductivities. LIEBERMAN AND KNOWLES (1998) presented a similar system (the so-called *in situ video microscope*). BREUL AND GOURVES (2006) obtained texture information from *geoendoscope* soil images.

COOPER AND MALONE (1992) and GREY ET AL. (1993) presented penetrometer probes for *in situ* detection of hydrocarbon contaminants by spectral means. These types of apparatus have been further developed by several working groups, e.g., BUCHOLTZ ET AL. (1998) and NAU ET AL. (1995) presented a system to detect contaminants by *infrared spectroscopy*. LIEBERMANN (1998) applied a *laser-induced fluorescence (LIF)* system for *in situ* detection of soil contamination with cone penetrometer technology, capable for collecting fluorescence fingerprints of chemical contaminants. Several studies applied *LIF* in the frame of soil remediation (*in situ* detection of organic contaminants). HENGSTERMANN ET AL. (2002) investigated petroleum in the ground. GRUNDL ET AL. (2003) and HAWTHORNE ET AL. (2008) detected *polycyclic aromatic hydrocarbons (PAHs)*. KRAM ET AL. (2001, 2002) measured the amount of *dense non-aqueous phase liquids (DNAPLs)* in the ground, equally so this was investigated for *non-aqueous phase liquids (NAPLs)* by KRAM AND KELLER (2004A, 2004B) and ST GERMAIN ET AL. (2006). SINFIELD ET AL. (2007) detected benzene, toluene, and o-xylene (*BTX*); D’AFFONSECA ET AL. (2008) investigated coal tar remains. Furthermore, MOSIER-BOSS ET AL. (2002) showed a sensor probe for real-time, *in situ* measurement of metals in soils (inorganic contaminant).

In this thesis, we use the *colour logging tool (CLT)* (as we have named it), which was developed in the framework of the aforementioned geochemical *DPT (LIF)*. The tool is based on the same concept, since inducing an optical signal (transferred to the soil) can measure the reflectance response. However, the *CLT* contains a photo-detector to gather the three base spectrum colours (red, green, blue). This data is transferrable into a set of standardised colour systems (CIE, 1931, 1978, 1996). For instance, TKALCIC AND TASIC (2003), VISCARRA ROSSEL ET AL. (2006) and WYSZECKI AND STILES (1982) provided a detailed overview of these colour systems. Previous studies showed the applicability of these types of colour probes for the determination of soil properties. BARRETT (2002) used a hand-held colorimeter for on-site colour measurements at the open face of a soil pit in a sandy environment and compared the results with laboratory measurements. BEN-DOR ET AL. (2008) presented a system, which takes colour measurements in pre-drilled holes at 10-cm depth intervals. However, compared to the existing portable *in situ* field colorimeter, the *CLT* device provides higher resolution vertical log data.

### 5.3 Field site

For the investigation, we selected an active clay and gravel pit located close to the city of Taucha. We kindly refer the reader to chapter 2.2 for a general site description (Figure 2-2). At the test site, we anticipate a tripartite layer structure (sand, till, clay). This provides excellent conditions for testing the *CLT* because of the sharp *SC*-contrasts that occur

between the single layers and given our prior knowledge of the very low ground water table within the sands.

## 5.4 Methods

### 5.4.1 Colour logging tool (*CLT*)

The *CLT*-device is a *DP*-driven piece of apparatus used for real-time *in situ* detection of *SC*. The system is a tristimulus colorimeter, which uses the narrow wavelength bands throughout the spectrum to measure the amount of radiation in the visible spectrum (BARRETT, 2002). Colorimeter and spectro-photometer (in contrast to spectro-radiometer) do not depend on ambient light because they contain an internal light source. Colorimeters use photo detectors to gather the three base colours (red, green, blue), providing this information as tristimuli ratios which can be transferred into standardised colour systems. In contrast, spectro-photometer and spectro-radiometer devices detect spectral data whose scope is in wavelength form (wavenumber). BARRETT (2002) showed that spectro-photometers are widely in use as laboratory-only models and concluded that portable colorimeters are more common, compared to portable spectro-photometers because they cost less.

The *CLT*-system consists of a light source, a spectrometer, a photo sensitive chip (photo detector), and a hollow soil penetrometer which are connected by optical fibres (Figure 5-2). The source induces white light, which is conducted via optical fibres to the probe. In the probe's optical chamber, the incoming light is redirected from the distal ends of the optical fibre by a mirror (in a vertical to horizontal direction). Thus, light passes through a transparent sapphire glass window into the soil. The reflected light from the soil passes back through and is redirected, captured, and transmitted by another optical fibre to a photo sensitive chip (charge-coupled device - CCD) at the surface unit. This detects the *SC* throughout the reflection spectrum from 350–1,000 nm. The highly sensitive and low dark current linear image sensor has 3,648 elements and has a pixel size resolution of 8  $\mu\text{m}$  x 200  $\mu\text{m}$ .

The source and the sensor require calibration before each measurement in order to define the white point within the spectrum (reference value). The data is then measured as an integral value over time. This integration time is calculated automatically from the relation between the dark signal voltage per saturation (voltage given as a per-centage) to the device chip temperature. Generally, the integration time ranges between 100–500 ms and stays fixed during a single log; where 300–350 ms is optimal. Thus, the recorded depth section depends on the probing velocity. This, lower velocity increases the vertical resolution of the log, whereas higher velocity smooths the *SC*-data during measurement.

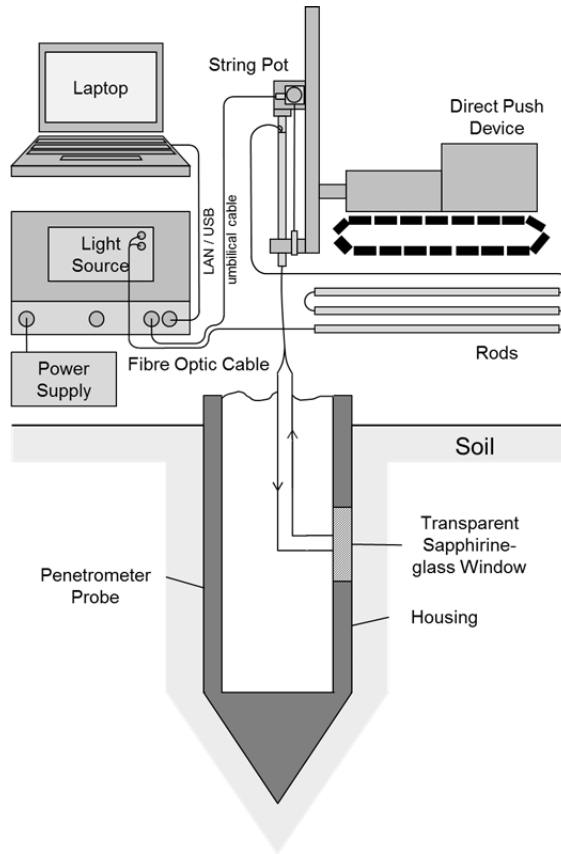


Figure 5-2: CLT-components applied on DP-rig.

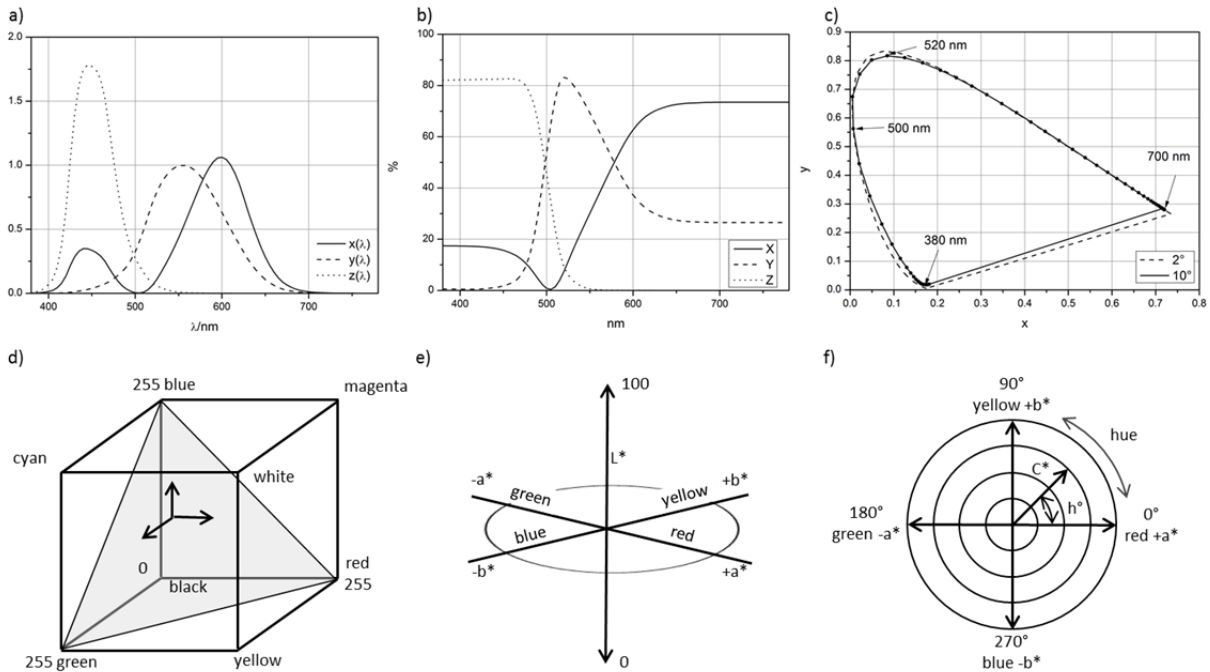


Figure 5-3: Conjunctural figure transforming colorimeter tristimuli data  $XYZ$  in norm standardised colour systems; a) Normal distribution of the three colour matching functions  $\bar{x}(\lambda)$ ,  $\bar{y}(\lambda)$ ,  $\bar{z}(\lambda)$  (CIE, 1931); b) CIEXYZ-colour system (CIE, 1931) with the proportions of the tristimuli  $XYZ$  gained by conversion of the colour matching functions; c) CIE (1931) 2°-degree standard colorimetric observer and CIE 1964 10°-supplementary standard colorimetric observer within the CIE $xY$ -system with added wavelength in nm; d) Cubic RGB-colour system as a mixture between R – red, G – green, and B – blue base colours; e) Cartesian CIEL\*a\*b\*-colour system with  $L^*$  - luminosity (0 – 100), green-red ratio  $a^*$ , and blue-yellow ratio  $b^*$ ; f) Cylindrical CIEL\*c\*h\*-colour system with chroma  $c^*$  and hue  $h^\circ$ .

The spectral response signal is computed as  $XYZ (D_{65})$  CIE 1964 10°-supplementary standard colorimetric observer tristimuli (CIE, 1978). The depth acquisition system automatically adds depth information and the calculated penetration rate to the logged colours. A limiting factor of the system is the probing velocity, which directly influences the data resolution because of integration time.

We used a *CLT* (also known as *soil color optical screening tool*<sup>TM</sup>) designed by *Dakota Technologies Inc.*, USA (URL 3). The gathered vertical colour logs allow soil classification for various purposes. Nowadays, the *CLT* is not widespread in use.

#### 5.4.2 Soil sampling (*SS*)

The basics of *DP*-based *SS* have previously been described. We kindly refer the reader to (→ Chapter 3.3.5) for more detailed information. At the Taucha test site, we used *SONIC*-equipment designed by *SonicSampDrill BV.*, The Netherlands (URL 18) and *DT22* soil sampling system designed by *Kejr Engineering Inc. – Geoprobe Systems*, KS, USA (URL 5).

#### 5.4.3 Numerical transformation of *in situ*-obtained *SC*

The transformation of raw data into certain *SC*-systems allows the creation of vertical layer profiles according to the assumption that soil colour is a proxy for soil classification and a criterion for stratigraphic differentiation. The colour systems, thereof derived surrogates, and indices were chosen to split-up colour data into independent values (colourfulness/ chroma, luminosity/brightness, saturation index, etc.), which can be used as comparable numerical data for analysis of the vertical colour distribution. Key selection criteria of these models are transferability and the possibility to specify colour data as points within coordinate systems, as well as the extent to which they are broadly used in soil science (→ Chapter 5.2).

In general, colour is a three-dimensional psychophysical phenomenon which can be represented in colour space models, whereby individual colours are specified by points in these spaces (VISCARRA ROSSEL ET AL., 2006). The raw data from the presented colorimeter probe is provided in CIE $XYZ$ -tristimuli values (CIE, 1931). These are proportions of the three base colours red, green, and blue (according to human cognition of colours). We transformed the tristimuli data into various trichromatic colour space models. The CIE $XYZ$  and the CIE $xyY$ , CIE $L^*a^*b^*$ , CIE $L^*c^*h^*$  (CIE, 1931; CIE, 1978; CIE, 1996), and *RGB*-colour systems we used are presented in Figure 5-3 and Table 5-1 to be explained in more detail in the next chapters.

We did not use any other existing colour space models for several reasons, i.e., we found *Munsell HVC*-colour space (MUNSELL COLOR COMPANY, 1994) to be inappropriate, because the values hue  $H$ , value  $V$ , and chroma  $C$  do not depend on the quantitative measurement of visible light and, furthermore, the system is cylindrical. The *CIEL\** $c^*h^*$  system also deals with the same terms hue and chroma, denoted by  $h^*$  and  $c^*$ , respectively. However, it is not equivalent to the aforementioned colour system. This was designed to identify the components of colour in terms of correlates of perceived hue, chroma, and lightness (VISCARRA ROSSEL ET AL., 2006). The *HSL*-colour space (hue, saturation, value) as a linear transformation of *RGB*-values was also not used in this work because of the numerous variations of equations stated in the relevant literature, e.g., TKALCIC AND TASIC (2003) and VISCARRA ROSSEL ET AL. (2006).

#### 5.4.4 The CIEXYZ-colour space

The CIEXYZ-tristimuli data are standardised values (CIE, 1931) representing the colour ratio of the three defined and normalized base colours red, green, and blue. The measured data correspond to the  $D_{65}$ -white point (CIE, 1996). This normal light is defined as normalised middle daylight with a colour temperature of 6,500 K, a light yield of 35 lm/W and a colour rendering index of 94 (KLEIN, 2004).

In general, all colours can be ascribed with XYZ-values. Standardized tristimuli curves were introduced by CIE (1931). These refer to the wavelength values, which were detected in the ranges of 20, 10, 5, or 1 nm from the source. The  $\bar{x}(\lambda)$ ,  $\bar{y}(\lambda)$ ,  $\bar{z}(\lambda)$ -values obtained are colour-matching functions of the ground colours. According to CIE (1996) recommendations, the XYZ-tristimuli values of a colour stimulus can be obtained by multiplying the colour stimulus function  $\phi_\lambda(\lambda)$  for each wavelength value. Thus, each colour-matching function (CIE, 1931) and the integrated set of products over the wavelength range correspond to the entire visible spectrum within 360–830 nm. CIE (1996) suggest that the integration may be carried out by numerical summation at wavelength intervals  $\Delta\lambda$  equal to 1 nm. For most practical purposes, a  $\Delta\lambda$ -summation at 5-nm wavelength intervals is suitable over the wavelength range 380–780 nm.

The XYZ-tristimuli are weighted to the normalized constant  $k$  (equation 5-1). The value  $k$  relates to the remission or spectral reflectance factor  $R(\lambda)$  or the transmission of a sample and  $S(\lambda)$ , which is the relative spectral power distribution. These values are detected against the ideal reflecting diffuser, which normally is a  $\text{BaSO}_4$ -standard (KLEIN, 2004; WYSZECKI AND STILES, 1982). For reflecting or transmitting object colours, the colour stimulus function  $\phi_\lambda(\lambda)$  is replaced by the relative colour stimulus function (equation 5-2) (CIE, 1996). The remission rate is then set to 100 for each detected wavelength interval. The assumed

value 100 coincides with the definition that  $Y$  as *perfect white* should be 100. Hence, the co-ordinates are computed with reference to the  $D_{65}$  -white point of the  $10^\circ$ -observer, which is defined in CIEXYZ-tristimuli as  $X_0 = 94.811$ ;  $Y_0 = 100$  and  $Z_0 = 107.304$ .

$$k = \frac{100}{\sum_{\lambda} S(\lambda) \bar{y}(\lambda) \Delta\lambda} \quad (5-1)$$

$$\phi(\lambda) = R(\lambda) \cdot S(\lambda) \quad (5-2)$$

#### 5.4.5 The CIE $xyY$ -colour space

The CIE $xyY$  is a two-dimensional and perceptually non-linear colour system (Figure 5-3). We calculated the colorimetric coordinates according to (CIE, 1996; Table 5-1). The co-ordinates are computed with reference to the  $D_{65}$  white point of the  $10^\circ$ -observer. Hence, the XYZ-values are indexed by 10. Following equation 5-3, it is sufficient to quote only  $x$  and  $y$  (CIE, 1996).

$$x_{10} + y_{10} + z_{10} = 1 \quad (5-3)$$

#### 5.4.6 The CIE $L^*a^*b^*$ -colour space

The CIE $L^*a^*b^*$ -colour system is defined as a three-dimensional, approximately uniform colour space with the rectangular coordinates  $L^*$ ,  $a^*$ , and  $b^*$  (CIE, 1978; CIE, 1996; Figure 5-3). The metric lightness function or luminosity  $L^*$  describes the brightness of the colour between pure black ( $L^* = 0$ ) and pure white ( $L^* = 100$ ) on the  $y$ -axis. The terms  $a^*$  and  $b^*$  describe the colour stimulus specification. The value  $a^*$  is the red-green-ratio whereas  $b^*$  is the yellow-blue-ratio. For computing the difference of the colour ratios, the Euclidean to  $\Delta E_{ab}^*$  distance can be used (CIE, 1978). The formulas are presented in Table 5-1. The CIE $L^*a^*b^*$ -colour space is almost equal to CIE $L^*u^*v^*$  (CIE, 1978). In contrast to the previous example, it allows the transformation to CIE $L^*c^*h^*$ .

Table 5-1: Summary of applied formulas, key parameters, and citations for *SC*-surrogates; colour space indicated by letters A) CIEXYZ, B) CIE $xyY$ , C) CIE $L^*a^*b^*$ , D) CIE $L^*c^*h^*$ , E) *sRGB*, F) *RGB*.

| Colour space, relevant parameter                      | Formula (Application range)  | References       |
|---|--|------------------|
| A) Colour-matching functions for red, green, and blue | $X = k \sum_{\lambda} \phi_{\lambda}(\lambda) \bar{x}(\lambda) \Delta\lambda$ ; $Y = k \sum_{\lambda} \phi_{\lambda}(\lambda) \bar{y}(\lambda) \Delta\lambda$<br>$Z = k \sum_{\lambda} \phi_{\lambda}(\lambda) \bar{z}(\lambda) \Delta\lambda$ | CIE (1931)       |
| B) Colorimetric coordinates                           | $x_{10} = \frac{X_{10}}{(X_{10}+Y_{10}+Z_{10})}$ ; $y_{10} = \frac{Y_{10}}{(X_{10}+Y_{10}+Z_{10})}$ ; $z_{10} = \frac{Z_{10}}{(X_{10}+Y_{10}+Z_{10})}$   | CIE (1996)       |
| C) Luminosity [-]                                     | $L^* = 116 \cdot \left(\frac{Y_{10}}{Y_0}\right)^{\frac{1}{3}} - 16$ ; $\left(\frac{Y_{10}}{Y_0}\right) > 0.008856$ $0 \leq L^* \leq 100$  | CIE (1978, 1996) |

| Colour space, relevant parameter                     | Formula (Application range)   | References                    |
|--|---|-------------------------------|
| C) Luminosity [-]                                    | $L^* = 903.3 \cdot \left(\frac{Y_{10}}{Y_0}\right); \left(\frac{Y_{10}}{Y_0}\right) < 0.008856$<br>0 = white; 100 = pure black  | CIE (1978, 1996)              |
| C) Red-Green-ratio [-]                               | $a^* = 500 \cdot \left[ \left(\frac{X_{10}}{X_0}\right)^{\frac{1}{3}} - \left(\frac{Y_{10}}{Y_0}\right)^{\frac{1}{3}} \right]$<br>$X/X_n, Y/Y_n, Z/Z_n > 0.008856$  | CIE (1978, 1996)              |
| C) Yellow-Blue-ratio [-]                             | $b^* = 200 \cdot \left[ \left(\frac{Y_{10}}{Y_0}\right)^{\frac{1}{3}} - \left(\frac{Z_{10}}{Z_0}\right)^{\frac{1}{3}} \right]$<br>$X/X_n, Y/Y_n, Z/Z_n < 0.008856$ ; term (quotient) <sup>1/3</sup> must be replaced by 7.787 quotient + 16/116 if previous conditions for a* or b* are not fulfilled)  | CIE (1978, 1996)              |
| C) Euclidean distance between a* and b* in space [-] | $\Delta E_{ab}^* = \sqrt{[(\Delta L^*)^2 + (\Delta a^*)^2 + (\Delta b^*)^2]}$   | CIE (1978)                    |
| D) Chroma [%]  | $c^* = \sqrt{a^{*2} + b^{*2}}$<br>0 = neutral grey; 50 = low saturated color; 100 = completely saturated color  | CIE (1978, 1996)              |
| D) Hue angle [°]                                     | $h^* = \arctan\left(\frac{a^*}{b^*}\right)$<br>$0^\circ \leq h^* \leq 90^\circ; a^*, b^* > 0$<br>$90^\circ < h^* \leq 180^\circ; a^* < 0 \text{ and } b^* > 0$<br>$180^\circ < h^* \leq 270^\circ; a^*, b^* < 0$<br>$270^\circ < h^* \leq 360^\circ; a^* > 0 \text{ and } b^* < 0$  | CIE (1978, 1996)              |
| D) Hue distance [-]                                  | $\Delta H_{ab}^* = \sqrt{(\Delta E_{ab}^*)^2 - (\Delta L^*)^2 - (\Delta c^*)^2}$  | CIE (1978, 1996)              |
| E) Transformation from CIEXYZ to sRGB                | $\begin{bmatrix} X \\ Y \\ Z \end{bmatrix} = [M] \cdot \begin{bmatrix} r \\ g \\ b \end{bmatrix} \text{ or } \begin{bmatrix} r \\ g \\ b \end{bmatrix} = [M]^{-1} \cdot \begin{bmatrix} X \\ Y \\ Z \end{bmatrix}$<br>$0 \leq XYZ \leq 100$ in [%]<br>$0 \leq RGB \leq 255$<br>0 = darkness, 255 = whiteness  | CIE (1978)                    |
| E) sRGB companding function for rgb to RGB           | $\begin{bmatrix} X \\ Y \\ Z \end{bmatrix} = \begin{bmatrix} 0.4124564 & 0.3575761 & 0.1804375 \\ 0.2126727 & 0.7151522 & 0.0721750 \\ 0.0193339 & 0.1191920 & 0.9503041 \end{bmatrix} \cdot \begin{bmatrix} r \\ g \\ b \end{bmatrix}$<br>$\begin{bmatrix} r \\ g \\ b \end{bmatrix} = \begin{bmatrix} 3.2404542 & -1.5371385 & -0.4985314 \\ -0.96992660 & 1.8760108 & 0.0415560 \\ 0.0556434 & -0.2040259 & 1.0572252 \end{bmatrix} \cdot \begin{bmatrix} X \\ Y \\ Z \end{bmatrix}$<br>$V = \{12.92v \quad v \leq 0.0031308$<br>$V = \{1.16v^{1/2.4} - 0.055 \quad v > 0.0031308$ | WYSZECKI AND STILES (1982)    |
| E) Brightness index [-]                              | $BI = \sqrt{(R^2 + G^2 + B^2)/3}$   | WYSZECKI AND STILES (1982)    |
| E) Saturation index [-]                              | $SI = \frac{(R-B)}{(R+B)}$  | LEVIN ET AL.(2005);           |
| E) Hue index [-]                                     | $HI = \frac{(2 \cdot R - B - G)}{(G - B)}$  | MADEIRA ET AL. (1997);        |
| E) Colouration index [-]                             | $CI = \frac{(R-G)}{(R+G)}$  | MATHIEU ET AL. (1998);        |
| F) Decorrelated hue [-]                              | $H_{RGB} = \frac{(2 \cdot G) - R - B}{4}$   | RAY ET AL. (2004)             |
| F) Decorrelated light intensity [-]                  | $I_{RGB} = \frac{R + G + B}{3}$   | WISCARRA ROSSEL ET AL. (2006) |
| F) Decorrelated saturation [-]                       | $S_{RGB} = \frac{R - B}{2}$   |                               |

#### 5.4.7 The CIEL\**c*\**h*\*-colour space

The spherical coordinates from CIEL\**a*\**b*\* can be transformed into cylindrical coordinates within the colour space model (Figure 5-3). Instead of the *a*\* and *b*\* as colour stimulus specifications, the chroma *c*\* as the value for the colourfulness or saturation of a colour and the hue  $\Delta H_{ab}^*$  with the related hue angle *h*\* are used to describe the colour distribution. The chroma is given as a percentage, where 0 % = neutral grey, 50 % = low saturated colour, 100 % = completely saturated colour. The hue is described as the hue angle within the colour space. The hue angle is positioned in the four quadrants of the ideal circle, depending on whether the ratios are positive or negative. The angle itself can be translated into colours, e.g., 0° = red, 120° = green, 240° = blue. The calculation of the metric lightness function or luminosity *L*\* is calculated in the same manner as the CIEL\**a*\**b*\*-system (CIE, 1978; CIE, 1996). The equations that transfer the CIEL\**a*\**b*\* into CIEL\**c*\**h*\*-colour system are given in Table 5-1.

#### 5.4.8 The RGB-colour space and RGB-indices

The RGB-colour system describes the mixture of the three primary colours red (*R*), green (*G*), and blue (*B*) (Figure 5-3). The corresponding primary stimuli are 700, 546, and 436 nm (VISCARRA ROSSEL ET AL., 2006). The colour data are points realized in the cube limited by the cube face, where the values range from 0 (darkness) to 255 (whiteness). A total gamut of  $(2^8)^3$  different colours results from all of the possible combinations (WYSZECKI AND STILES, 1982). We calculated the RGB-values from the CIEXYZ-tristimuli using a transformation matrix *M*. In this thesis, *M* was used for the sRGB-colour space with the *D*<sub>65</sub>-white point representing the 1964 CIE 10°-supplementary standard colorimetric observer (CIE, 1978; WYSZECKI AND STILES, 1982), as presented in Table 5-1.

The XYZ-tristimuli were first rescaled as percentage values and then multiplied by the matrix values. The received linear RGB, denoted by *rgb* or *v* (equation 5-4), is transferred into non-linear RGB or generally *V* (equation 5-5) by gamma ( $\gamma$ ) companding (equation 5-6).

$$v \in \{r, g, b\} \quad (5-4)$$

$$V \in \{R, G, B\} \quad (5-5)$$

$$V = v^{\frac{1}{\gamma}} \quad (5-6)$$

We performed operation (5-6) for each channel. The companding function for the sRGB-colour space is also presented in Table 5-1.

The sRGB-values can also be used for the determination of various indices. We calculated the brightness *BI*, saturation *SI*, hue *HI*, and colouration index *CI* according to

LEVIN ET AL. (2005), MADEIRA ET AL. (1997), MATHIEU ET AL. (1998), and RAY ET AL. (2004) as ratios of *R*, *G*, and *B* (Table 5-1).

In addition, VISCARRA ROSSEL ET AL. (2006) suggested a decorrelation of the *RGB*-colours into three statistically independent components by transforming the single *RGB*-tristimuli. The outcome ratios  $H_{RGB}$ ,  $I_{RGB}$ , and  $S_{RGB}$  represent hue, light intensity, and chromatic information, respectively (Table 5-1).

#### 5.4.9 Denoising strategies

After numerical transformation of the raw data into a set of *SC*-surrogates, we applied two different filter approaches in order to smooth colour surrogates with depth, to decrease non-representative colour values and generally denoise the raw data (Figure 5-4). Both are adjustable and dependent upon layer description, e.g., for modelling. The processing flowchart illustrates the data denoising steps (Figure 5-4).

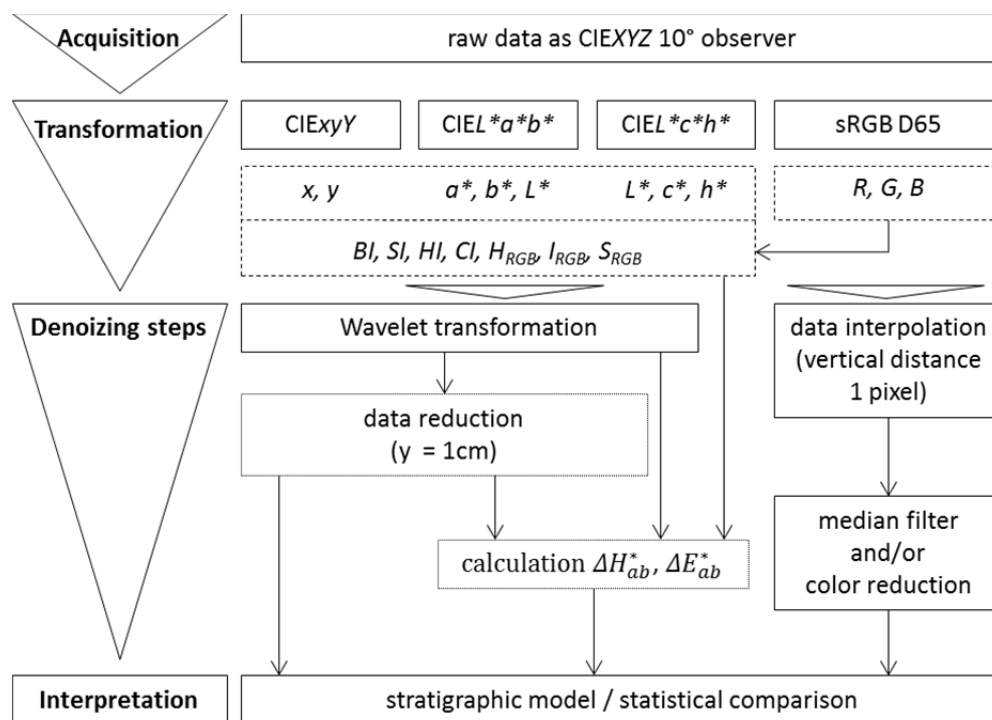


Figure 5-4: Processing flowchart from field data acquisition, numerical transformation of the raw data into a standardised colour system and associated denoising steps for enhanced data interpretation either using median filtering and colour reduction within the *RGB*-colour space or wavelet transformation (*WT*) approach. All symbols are explained in Table 5-1.

Following the transformation steps from CIEXYZ -raw data to *sRGB*-colour space, we received an ensemble of colours, which show variation with depth. The data set now contains *SC*-data as one-pixel values  $x$  and depth information  $y$ . Since the data is not equally distributed with depth, the values  $x$  were interpolated linearly. Thus, after interpolation, each

pixel represents 1-mm vertical resolution in the log. Afterwards, the data was smoothed using a sliding median  $\tilde{x}_n$  of the range  $n$ .

We achieved colour reduction by performing minimum variance quantization of all colours in the data set - for each applied median range or window size, respectively. Plotting all *RGB*-values as three-dimensional points in the cube will form clusters. Hence, reduction of the clusters will in turn reduce the total amount of colours. We could perform this approach with the *rgb2ind*-function in *MatLab* (URL 1). The *rgb2ind*-algorithm divides the *RGB*-colour cube into a number of smaller boxes, mapping all clustered colours, which fall into one cube to the colour value of the centre of that particular cube (URL 1). If the amount of clusters is reduced (manually constrained), the algorithm searches for bigger cubes or clusters, which generally will smooth the recorded data. We specified the quantity of clusters as being 5, 10, 15, 20, 25, and 30 in order to check the influence of cluster size against non-clustered data. The window size  $n$  of the sliding median  $\tilde{x}_n$  was increased stepwise from 10 pixel (1 cm) to 50 (5 cm), 100 (10 cm), 200 (20 cm), 500 (50 cm) to 1,000 (100 cm) pixel.

The recorded *RGB*-raw data mainly varies in grey and brown colours, with regard to the geological setting. These small visual differences are too slight to be recognised merely by human cognition. Therefore, for plotting the results we adjusted them into false colour representation to obtain a better visualization. Thus, we adjusted the three output channels of the received image files. The *R* (red) colour channel was set to 200, whereas the *G* (green) and *B* (blue) channel were reduced to 0. The same procedure was carried out for the green and blue output channel, respectively.

Secondly, we applied wavelet transformation (*WT*), which is generally similar to *FOURIER*-transformation in the sense that they can measure the time-frequency variations of spectral components in a signal (MALLAT, 2003). This method has great potential for denoising geophysical data (COOPER AND COWAN, 2009; DUCHESNE AND GAILLOT, 2011; PAN ET AL., 2008). Within *DP*-logs, the obtained parameter may also show high variation with depth. The variation can be understood as spectral components in a time-frequency signal. As such, we adopted this approach for filtering and denoising *SC*-data and their surrogates simply by replacing the time  $t$  by scale  $y$ . The recorded colour signal will be correlated with the so-called wavelets, which are single scaled aperiodic functions. The *WT* can be achieved in increasing levels, where the  $y$ -information of the signal is reduced by factor two for each level. This allows an adaptive smoothing of the data.

Generally, *WT* comes in families. The base wavelet for low-pass filtering is called the father wavelet. It captures the smooth, low frequency nature of data. However, mother wavelets capture the detailed and high frequency nature of data. Therefore, a father wavelet  $\varphi$  integrates to 1, whereas a mother wavelets  $\psi$  integrates to 0.

Thus, we applied *WT* to *DP*-logs, especially for *in situ*-obtained *SC* and their surrogates that show high variation. We first applied the HAAR-function with the mother wavelet  $\psi$  (equations 5-7 and 5-8) (MALLAT, 2003).

$$\frac{1}{\sqrt{2}} \psi\left(\frac{y}{2}\right) = \sum_{n=-\infty}^{+\infty} (-1)^{1-n} h[1-n] \phi(y-n) = \frac{1}{\sqrt{2}} (\phi(y-1)\phi(y)) \quad (5-7)$$

$$\psi(x) = \begin{cases} 1, & 0 \leq y < 1/2, \\ -1, & 1/2 \leq y < 1, \\ 0, & \text{otherwise.} \end{cases} \quad (5-8)$$

The father wavelet is  $\phi(y) = 1$  for  $y \in [0,1]$  and zero otherwise. Generally, the choice of mother wavelet and the scaling parameters depends on the application (AHUJA ET AL., 2005).

DAUBLET4 as one of DAUBECHIES' wavelet family (DAUBLET 2, 4, ..., 30) (DAUBECHIES, 1992) is a more commonly used wavelet (SHUMWAY AND STOFFER, 2011). The mathematical expressions for a continuous *WT* ( $T^{CWT}$ ) as function  $f(y)$  and the derived discrete *WT* ( $T^{DWT}$ ) are adopted from DUCHESNE AND GAILLOT (2011) and NALLEY ET AL. (2012) (equation 5-9 and 5-10).

$$T^{CWT} f(a, b) = \frac{1}{\sqrt{a}} \int_{-\infty}^{+\infty} f(y) \psi\left(\frac{y-b}{a}\right) dy \quad (5-9)$$

$$\psi_{a,b}(y) = \frac{1}{\sqrt{a}} \psi\left(\frac{y-b}{a}\right) \quad (5-10)$$

The term 5-10 is the analysing wavelet derived by dilatation and contraction of  $a$ , which is the scale factor and the translation parameter  $b$  from the mother wavelet function  $\psi$ . The value  $y$  is the space domain, which is depth in this current study. Replacing  $a$  by  $a_0^j$  and  $b$  by  $nb_0$  in equation (5-9) allows us to obtain discrete *WT* (equation 5-11).

$$T^{DWT} f_{j,n}(y) = a_0^{-j/2} \int_{-\infty}^{+\infty} f(y) \psi(a_0^{-j} y - nb_0) dy \quad (5-11)$$

The number of coefficients  $n$  that are used can be adjusted. They are associated with length. Therefore, for instance, the DAUBLET4-wavelet has  $4n$  coefficients, as presented in MALLAT (2003). Theoretically, an infinite number of wavelets exist. Both wavelets (HAAR and DAUBLET4) were applied to the enumerated soil colour surrogates and indices.

## 5.5 Results

### 5.5.1 Soil sampling (SS)

We performed *SONIC*-soil sampling (T/SON-1) to a depth of 16 m within <1 m distance of the soil colour measurements (Figure 2-2). The first 9 m of the profile are dominated by middle sands. From 10-m depth, there is evidence of the presence of till. At 14-m depth, we found a boundary between the till and the lower clay from Miocene age. Thus, we

could validate and verify what we expected to see, namely presence of the tripartite layer structure. For improved characterisation, we performed sieve analyses for samples from the T/SON-1-core (Figure 5-5). This allows a more detailed characterisation of the three observed layers.

In total, we found three major units, which can be described as (I) alluvial sand (0–9.40 m), (II) till (9.40–13.63 m), and (III) clay (13.63–15.20 m). The ill-fitting values in the final depth of each core-section occur because of core loss and compaction while sampling. The upper alluvial sand is composed of and dominated by middle sands, showing changing amounts of fines, fine sand, course sand, and fine to middle gravel. Therefore, locally we could observe bigger grains in the matrix. The till layer generally shows higher grain size variation. After grain size analysis, the material could be described as sandy silt to sandy clay. The clay layer also shows small amounts of silt and fine sands.

The upper sand is very finely layered and shows reddish, yellow, and light brown colours, and is sometime bleached. The till shows rusty-brown colours at the top, continuing with dark grey and dark brown mixed layers. The lower clay shows grey, dark grey and light grey sections.

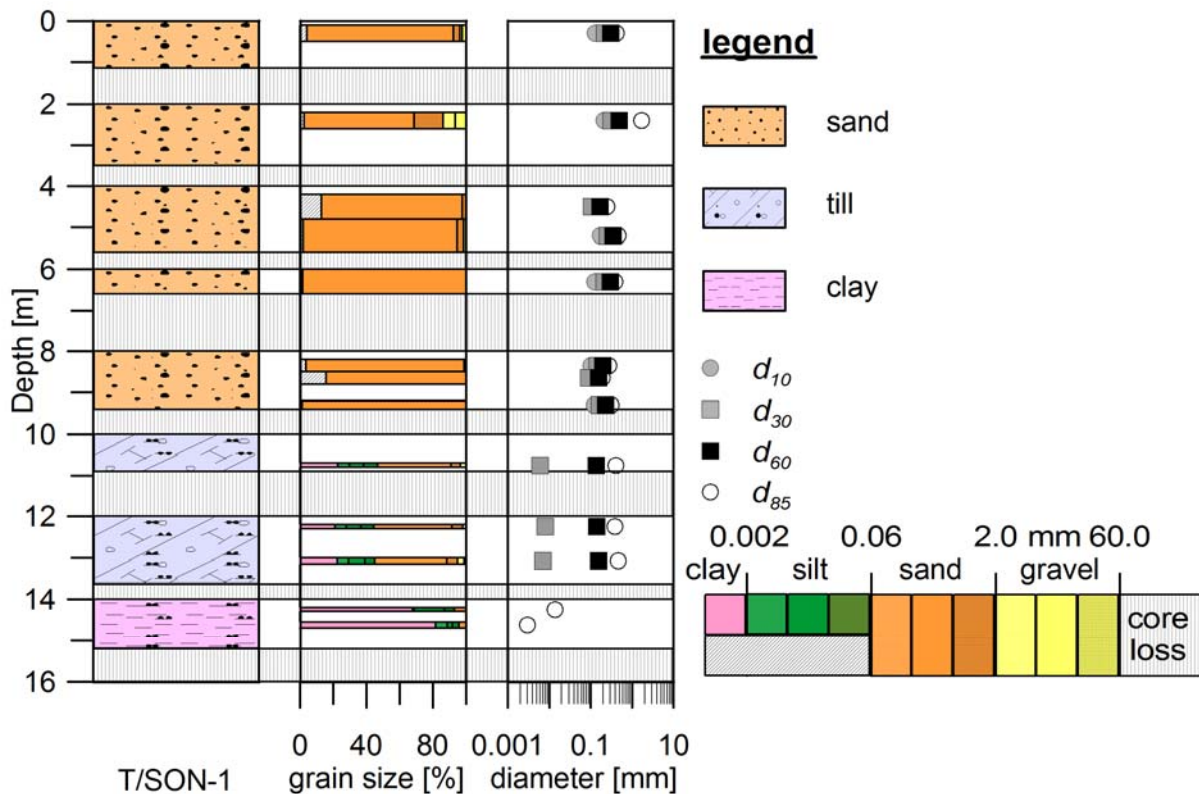


Figure 5-5: Stratigraphic interpretation and sieve analyses according to DIN 18123 for T/SON-1 at Taucha test site.

### 5.5.2 Resolution of *in situ*-obtained *SC*-data

The *CLT*-probing (T/CLT-80/1–5) were performed cluster form (Figure 2-2). Investigation depths and additional ground water levels are explained in Appendix B.

For characterisation of the vertical resolution of the five repeated *SC*-measurements, we initially classified the raw data with regard to depth resolution. For our analysis, we calculated  $\Delta y$ -values (distance between data logs) for each measurement/log and sorted these values into classes of 1 mm. Then we added up the single classes for the individual recordings T/CLT-80/1, T/CLT-80/2, T/CLT-80/3, T/CLT-80/3, T/CLT-80/4, and T/CLT-80/5. Thus, 80% of the data was recorded with a vertical distance of 5–6 mm or less, whereas 90% of data can be sorted into the 6–7-mm class (Figure 5-6). In comparison, only the T/CLT-80/5-profile was slightly less dispersed. Thus, the depth resolution of the single measurements is very high, but not constant. Shifting  $\Delta y$ -values occur because the penetration velocity could not be kept constant during one probing. The integration time is also non-equal between the five repeated probings because each was calibrated individually. Thus, we find a vertical resolution of 10 mm to be an appropriate lower boundary for data reduction. All aforementioned profiles show high variation for colour values.

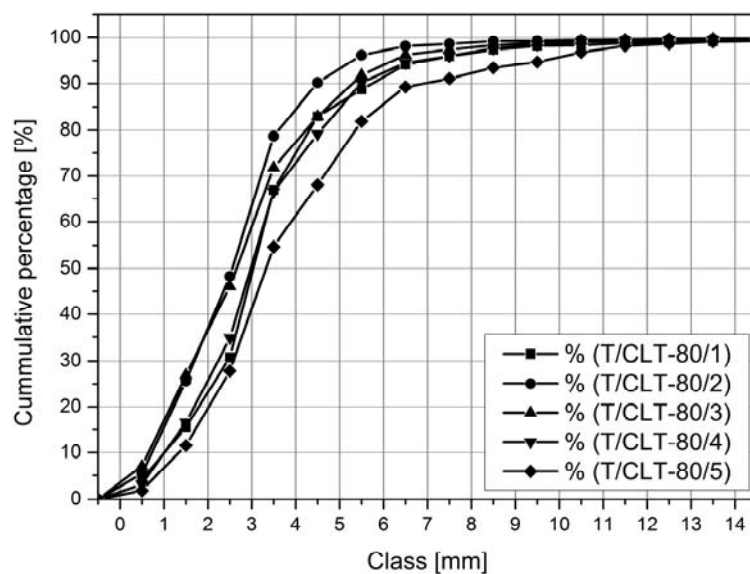


Figure 5-6: Distribution of  $\Delta y$  for repeated colour logs.

### 5.5.3 Colour reduction within *sRGB*-colour space

We applied the colour reduction algorithm to the dataset T/CLT-80/1. Figure 5-7A plots the results with stepwise increasing of the vertical median filter, while colour reduction remained constant and was five colours in total. The window size of the median filter starts at 10 pixels and ends at 1,000 pixels. 10 pixels represent 1-cm vertical resolution, whereas 1,000 pixels correspond to a vertical distance of 1 m, respectively. The data is more roughly

filtered because of increasing filter spread. Therefore, small colour bands which maybe represent a single layer are more and more smoothed out, forming vertical blocks of equal colour values.

In addition to the previous results, Figure 5-7B presents increasing colour reduction with constant median filter median of  $\tilde{x}_{100} = 10 \text{ cm}$  vertical resolution. This range was chosen as it revealed itself to be an appropriate depth unit in order to smooth out very small colour contrasts. The results show, that the reduction of total colours enables us to better describe single individual layers. There is no established or fixed rule for setting minimum values for accurate profile description, as far as colour limits are concerned.

Generally, the data shows the same *SC*-distribution according to depth as expected from the geological setting (Table 2-2). A highly diverse top layer (0–9.80 m depth) covers a more uniform block (>13.50 m depth). Beneath this, another more uniform coloured layer is visible. These three units can be interpreted as (I) sand, (II) till, and (III) clay layers, respectively. The boundaries of the three main layers vary in depth by up to 0.5 m, dependent upon the amount of filtering.

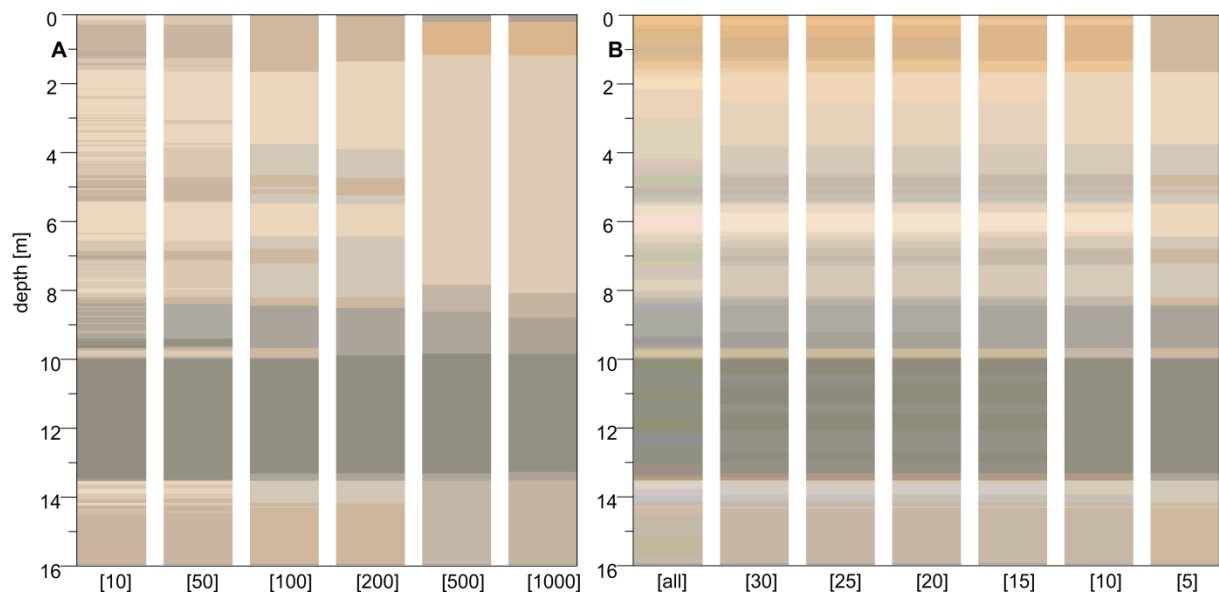


Figure 5-7: Comparison of *RGB*-data of T/CLT-80/1-colour profile (false coloured plots), median filter and colourreduction; A) Continuously increasing vertical median filter (window size in parenthesis as pixel values, e.g., 10 pixel (1 cm), 50 pixel (5 cm), etc.) and constant colour reduction to five colours; B) Constant median filtering (100 pixel = 10 cm) with increasing colour reduction (number in parentheses) from zero colour reduction (all), 30 to 5 colours.

#### 5.5.4 Wavelet transformation (*WT*)

Figure 5-8 presents a qualitative comparison of applied HAAR-function in certain levels from 1–6 with a 50%-threshold in contrast to the unsmoothed raw data for calculated luminosity  $L^*$  from profile T/CLT-80/1. Here, the influence of the levels on the smoothness of the output data can be clearly observed. The same procedure was applied to the data using

the DAUBLET4-wavelet function. Similar levels and a 50%-threshold were also used, respectively (Figure 5-9). As estimated, the results show increased denoising with rising level. In summation, levels 1–3 still show a lot of noise in the signal, whereas 4–6 provide more rough data filtering. These results can be used for stratigraphic interpretation. The difference between the HAAR-function and DAUBLET4 becomes more apparent with rising levels. The HAAR-function exhibits more stepwise and blocky behaviour.

Figure 5-10 depicts results of the DAUBLET4 6-level 50%-threshold filtered colour surrogates of profile T/CLT-80/1. We computed the brightness index  $BI$ , saturation index  $SI$ , hue index  $HI$ , colouration index  $CI$ , the decorrelated hue  $H_{RGB}$ , the decorrelated light intensity  $I_{RGB}$ , and the decorrelated saturation  $S_{RGB}$  of the  $sRGB$ -colour space, the products of  $a^*$  and  $b^*$  from  $CIEL^*a^*b^*$ -colour system, as well as  $x$  and  $y$  from the  $CIE_{xyY}$ -colour space. Lastly, the Euclidian distances  $\Delta E_{ab}^*$  ( $CIEL^*a^*b^*$ ) and  $\Delta H_{ab}^*$  ( $CIEL^*c^*h^*$ ) are plotted as raw data. These are not denoised, due to the fact that the distances are not equally distributed with depth. The results show that the main stratigraphic components become visible. They can be subdivided into three major units, which are 0–9.40 m, 9.40–13.63 m, and 13.63–15.20 m (end of record T/SON-1).

### 5.5.5 Comparison of repeated measurements

The gathered *SC*-measurements show strong modulation of the raw data owing to high-resolution data recording. In order to check repeatability and variation of the vertical colour profiles, we performed a set of five probings in a close cluster (Figure 2-2). As an example, Figure 5-11 and Figure 5-12 presents luminosity  $L^*$  data for all previously mentioned profiles (T/CLT-80/1–5) and allows quantitative comparison. As can be seen here, the denoised data exhibit the same trends but also are subject to certain local variations. To check the general coherence of the recorded profiles, we calculated the aforementioned colour surrogates for all of them. After application of a 6-level 50%-threshold DAUBLET4 wavelet, we re-sampled the data by reducing it to a constant vertical distance of 1 cm. A number  $N$  of 1,339 total comparable data sets remained for a depth of 15.86 m. Then, we calculated the multiple regression coefficients  $R$  and  $R^2$  for each possible combination of the five profiles with  $\alpha = 0.05$ . The results of our statistical comparison are presented in Table 5-2. Greater variation reduces the number of comparable cases  $F$ , resulting in lower correlation coefficients. The results illustrate that the colour surrogates from repeated measurements show significant to good correlation, except for the Hue index  $HI$ . The maximum regression value was achieved with  $R^2 = 0.90$ . The probings T/CLT-80/2 and T/CLT-80/3 are not equivalent to the other probings. Most parameters do correlate well, however, some do not correlate at all. Ranking the surrogates according to the mean  $R^2$ , we found best correlations ( $0.70 \leq R^2 \leq$

0.80) for the product of red-green-ratio and blue-yellow-ratio ( $a^* \cdot b^*$ ), colouration index  $CI$ , decorrelated saturation  $S_{RGB}$ , and chroma  $c^*$ . The correlation coefficient  $R^2$  of the brightness index  $BI$ , the saturation index, the decorrelated light intensity  $I_{RGB}$ , and the luminosity  $L^*$  averages 0.68. The decorrelated hue  $H_{RGB}$  and the product of the colorimetric values ( $x \cdot y$ ) exhibit more diverse behavior.

Table 5-2: Regression coefficients  $R$  and  $R^2$  (bold) from multiple regression of denoised and resampled *SC*-surrogate values and indices for all profiles (T/CLT-80/1–5). Data was denoised using 6-level 50%-threshold DAUBLET4-wavelet and re-sampled to a constant vertical distance of 1 cm. *sRGB*-colour space:  $BI$  – brightness index,  $SI$  – saturation index,  $HI$  – hue index,  $CI$  – colouration index,  $H_{RGB}$  – decorrelated hue,  $I_{RGB}$  – decorrelated light intensity,  $S_{RGB}$  – decorrelated saturation; CIE $xyY$ -colour space:  $x \cdot y$  – product of colorimetric values; CIE $L^*a^*b^*$ -colour space:  $a^* \cdot b^*$  – product of red-green-ratio and blue-yellow-ratio,  $L^*$  – luminosity; CIE $L^*c^*h^*$ -colour space:  $c^*$  – chroma,  $h^*$  – hue angle.  $F$  = number of pairs with an  $\alpha = 0.05$ ;  $N = 1349$ .

|           | T/CLT-80/1<br>to<br>I/2-I/3-I/4-I/5 |       |      | T/CLT-80/2<br>to<br>I/1-I/3-I/4-I/5 |       |     | T/CLT-80/3<br>to<br>I/1-I/2-I/4-I/5 |       |      | T/CLT-80/4<br>to<br>I/1-I/2-I/3-I/5 |       |      | T/CLT-80/5<br>to<br>I/1-I/2-I/3-I/4 |       |      | all $R^2$ |             |
|-----------|-------------------------------------|-------|------|-------------------------------------|-------|-----|-------------------------------------|-------|------|-------------------------------------|-------|------|-------------------------------------|-------|------|-----------|-------------|
|           | $R$                                 | $R^2$ | $F$  | $R$                                 | $R^2$ | $F$ | $R$                                 | $R^2$ | $F$  | $R$                                 | $R^2$ | $F$  | $R$                                 | $R^2$ | $F$  | min-max   | $\emptyset$ |
| $BI$      | 0.84                                | 0.69  | 754  | 0.80                                | 0.64  | 605 | 0.89                                | 0.80  | 1323 | 0.81                                | 0.65  | 619  | 0.78                                | 0.61  | 517  | 0.61-0.80 | 0.68        |
| $SI$      | 0.86                                | 0.74  | 754  | 0.77                                | 0.60  | 499 | 0.69                                | 0.48  | 308  | 0.89                                | 0.79  | 1292 | 0.89                                | 0.78  | 1215 | 0.48-0.79 | 0.68        |
| $HI$      | 0.20                                | 0.04  | 14   | 0.04                                | >0.00 | 1   | 0.24                                | 0.06  | 26   | 0.10                                | 0.01  | 4    | 0.17                                | 0.03  | 10   | >0-0.06   | 0.03        |
| $CI$      | 0.89                                | 0.80  | 1342 | 0.82                                | 0.67  | 678 | 0.78                                | 0.61  | 518  | 0.92                                | 0.84  | 1795 | 0.92                                | 0.84  | 1735 | 0.61-0.84 | 0.75        |
| $H_{RGB}$ | 0.70                                | 0.49  | 323  | 0.75                                | 0.56  | 423 | 0.80                                | 0.64  | 594  | 0.80                                | 0.64  | 585  | 0.56                                | 0.32  | 156  | 0.32-0.64 | 0.53        |
| $I_{RGB}$ | 0.84                                | 0.70  | 779  | 0.79                                | 0.63  | 562 | 0.89                                | 0.80  | 1320 | 0.80                                | 0.64  | 606  | 0.78                                | 0.61  | 525  | 0.61-0.80 | 0.68        |
| $S_{RGB}$ | 0.92                                | 0.82  | 1496 | 0.81                                | 0.66  | 656 | 0.75                                | 0.56  | 427  | 0.90                                | 0.80  | 1374 | 0.90                                | 0.81  | 1409 | 0.56-0.82 | 0.73        |
| $xy$      | 0.86                                | 0.73  | 928  | 0.71                                | 0.51  | 352 | 0.58                                | 0.34  | 171  | 0.64                                | 0.41  | 231  | 0.88                                | 0.77  | 1132 | 0.34-0.77 | 0.55        |
| $a^*b^*$  | 0.86                                | 0.74  | 984  | 0.78                                | 0.61  | 526 | 0.87                                | 0.75  | 1005 | 0.94                                | 0.89  | 2783 | 0.95                                | 0.90  | 2948 | 0.61-0.90 | 0.78        |
| $L^*$     | 0.82                                | 0.67  | 674  | 0.83                                | 0.68  | 724 | 0.90                                | 0.81  | 1469 | 0.81                                | 0.65  | 629  | 0.78                                | 0.61  | 523  | 0.61-0.81 | 0.68        |
| $c^*$     | 0.89                                | 0.78  | 1323 | 0.79                                | 0.62  | 548 | 0.72                                | 0.52  | 368  | 0.89                                | 0.80  | 1341 | 0.90                                | 0.80  | 1379 | 0.52-0.80 | 0.70        |
| $h^*$     | 0.87                                | 0.75  | 1013 | 0.81                                | 0.65  | 631 | 0.66                                | 0.43  | 255  | 0.72                                | 0.52  | 361  | 0.84                                | 0.73  | 918  | 0.43-0.75 | 0.62        |

## 5.6 Discussion

We have shown that vertical resolution in the mm-range (Figure 5-1; Figure 5-6) becomes equal to the grain size of coarse sands. However, this very good resolution makes data interpretation challenging, as each larger grain or aggregate is represented as a series of equal values in the data set by passing the detection window. These pseudo-layers are non-representative for the whole soil horizon of the layer in which they are embedded. The raw data shows strong modulation. Hence, we developed an appropriate filter approach in order to perform accurate smoothing with regard to stratigraphic interpretation, allowing us to avoid some of the problems that high resolution can lead to (a false and/or over-interpretation of the layering structure).

We transferred the raw data into numerical surrogates (Table 5-1; Figure 5-10). The

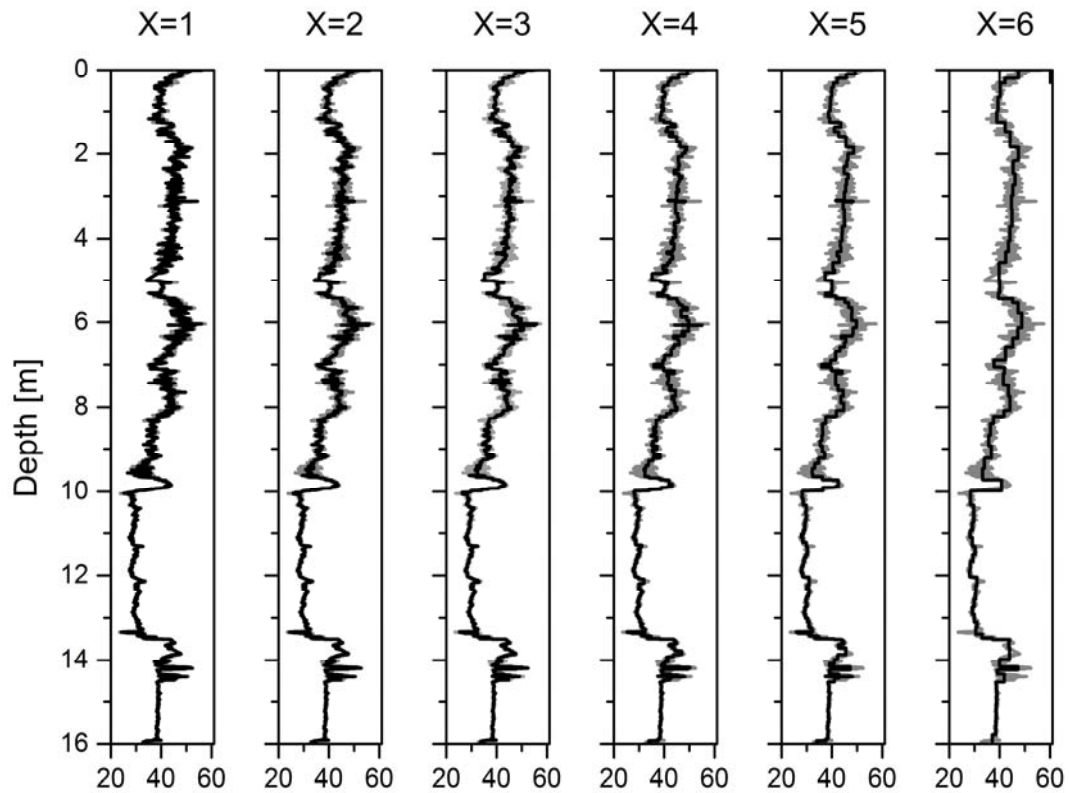


Figure 5-8: Comparison of luminosity data from CIEL\**a*\**b*\*-colour space from profile T/CLT-80/1; light grey = raw data; black = X-level(s) 50%-threshold HAAR-denoise.

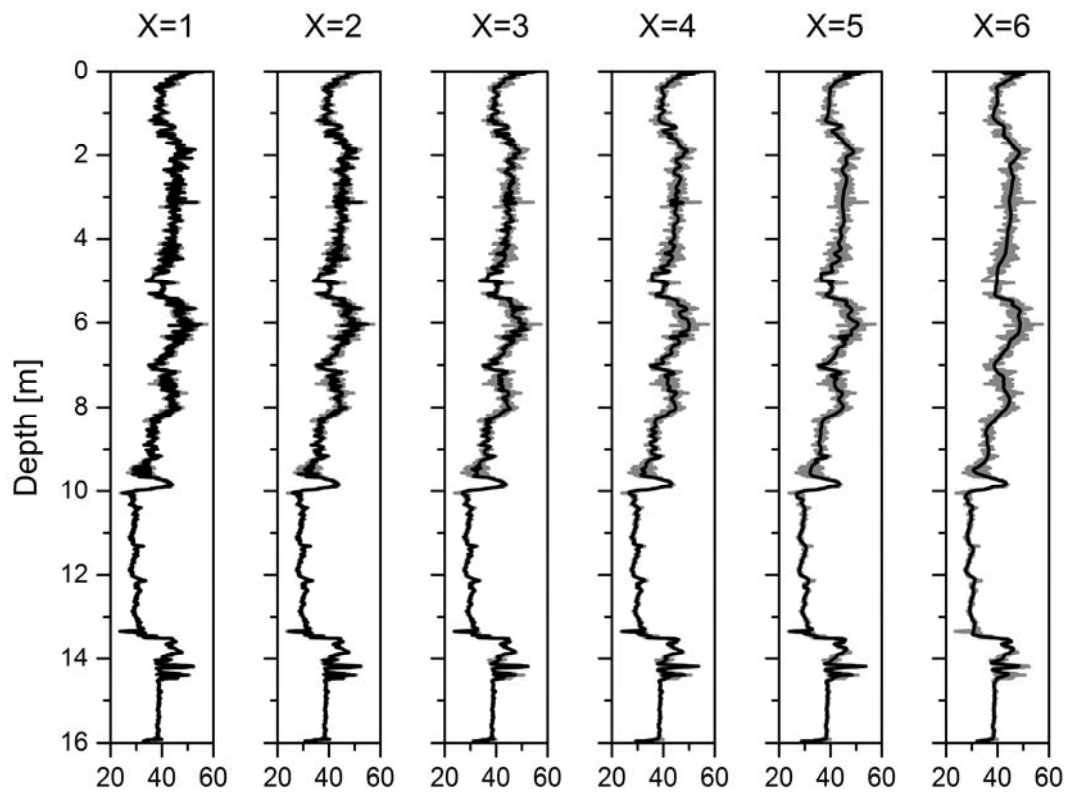


Figure 5-9: Comparison of luminosity data from CIEL\**a*\**b*\*-colour space from profile T/CLT-80/1; light grey = raw data; black = X-level(s) 50%-threshold DAUBLET4 denoise.

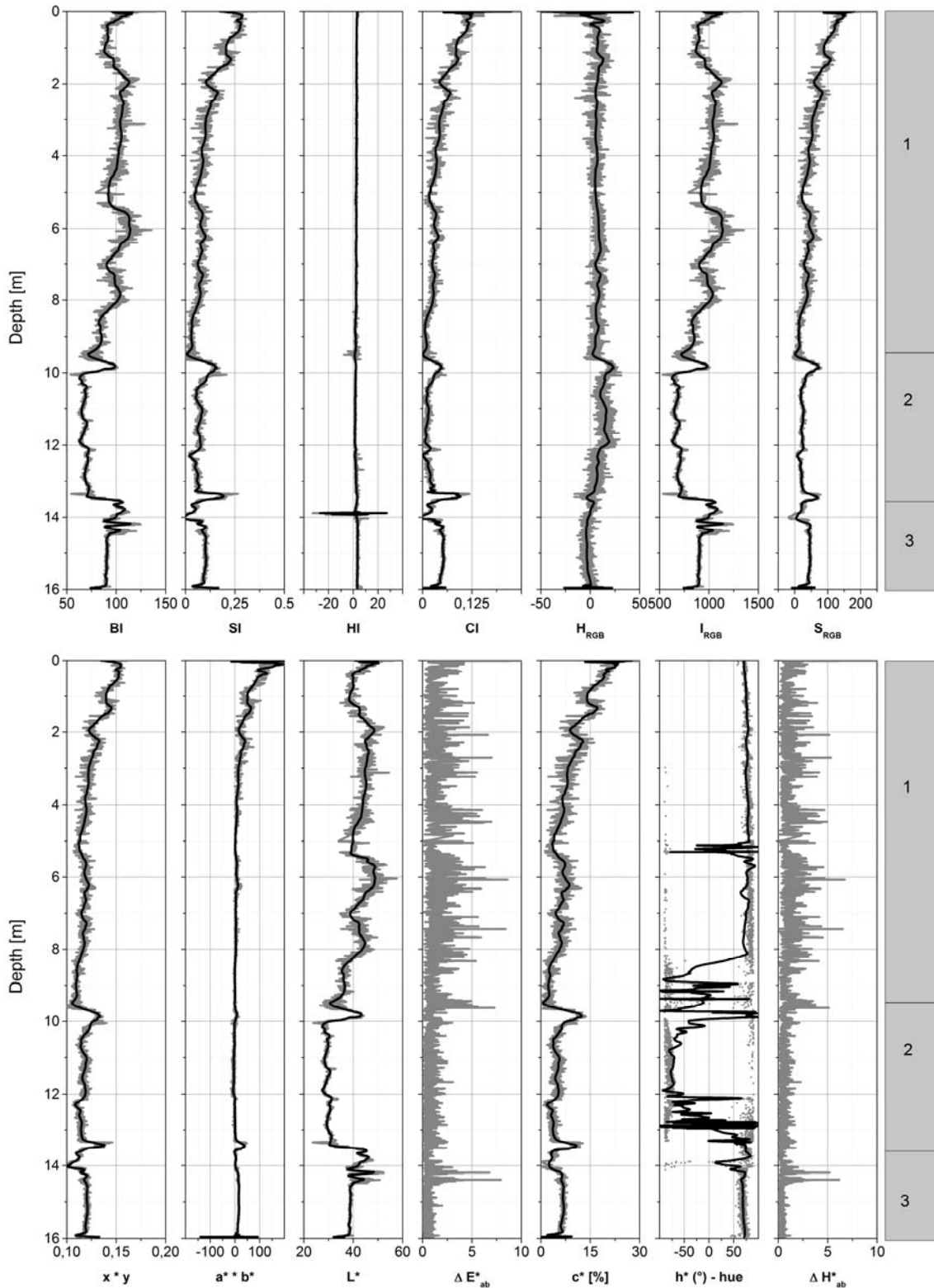


Figure 5-10: Comparison of raw and smoothed data for a set of SC-surrogates using 6-level 50%-threshold DAUBLET4-denoise (T/CLT-80/1) to the found three major stratigraphic units (T/SON-1) alluvial sand (I), till (II), clay (III); ( $\rightarrow$  Figure 5-5);  $sRGB$ -colour space:  $BI$  – brightness index,  $SI$  – saturation index,  $HI$  – hue index,  $CI$  – colouration index,  $H_{RGB}$  – decorrelated hue,  $I_{RGB}$  – decorrelated light intensity,  $S_{RGB}$  – decorrelated saturation;  $CIE_{xyY}$ -colour space:  $x \cdot y$  – product of colorimetric values;  $CIE_{L^*a^*b^*}$ -colour space:  $a^* \cdot b^*$  – product of red-green-ratio and blue-yellow-ratio,  $L^*$  – luminosity,  $\Delta E_{ab}^*$  – Euclidian distance between the colour values in this colour space;  $CIE_{L^*c^*h^*}$ -colour space:  $c^*$  – chroma,  $h^*$  – hue angle,  $\Delta H_{ab}^*$  – Euclidian distance between the colour values in this colour space.

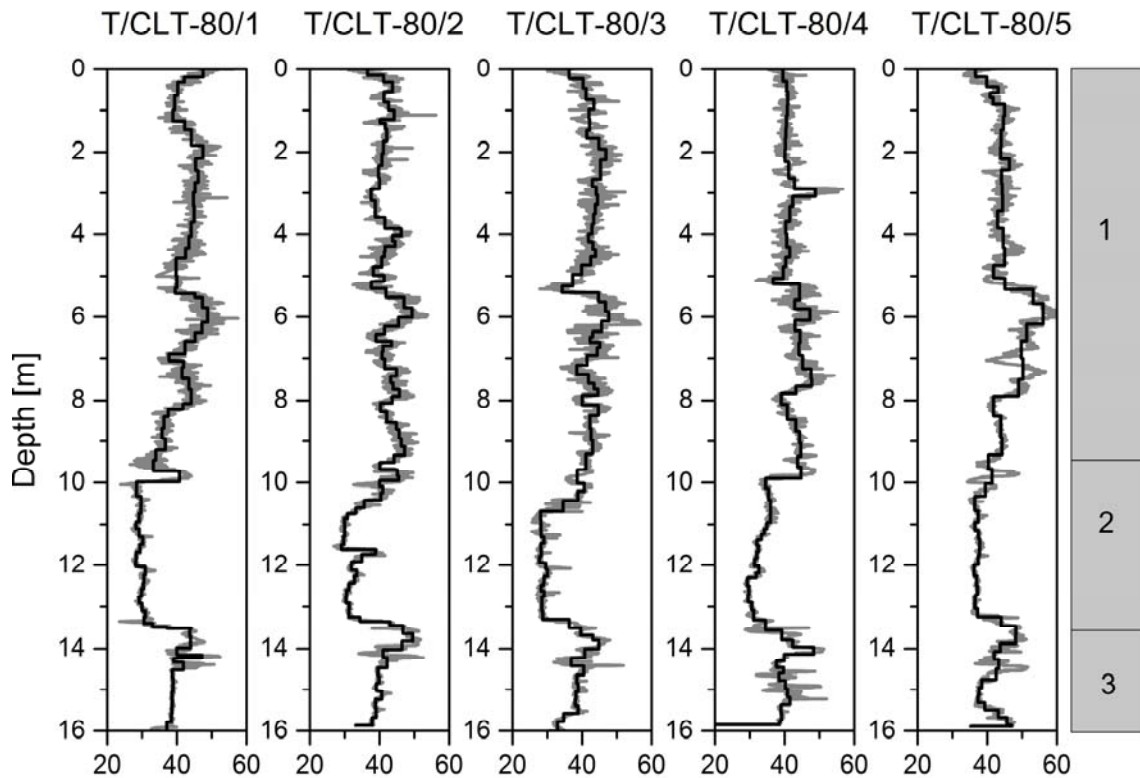


Figure 5-11: Comparison of luminosity data from CIEL\**a*\**b*\*-colour space from profiles T/CLT-80/1-5; light grey = raw data; black = using 6-level 50%-threshold HAAR-denoise to the found three major stratigraphic units (T/SON-1) alluvial sand (I), till (II), clay (III); (→ Figure 5-5).

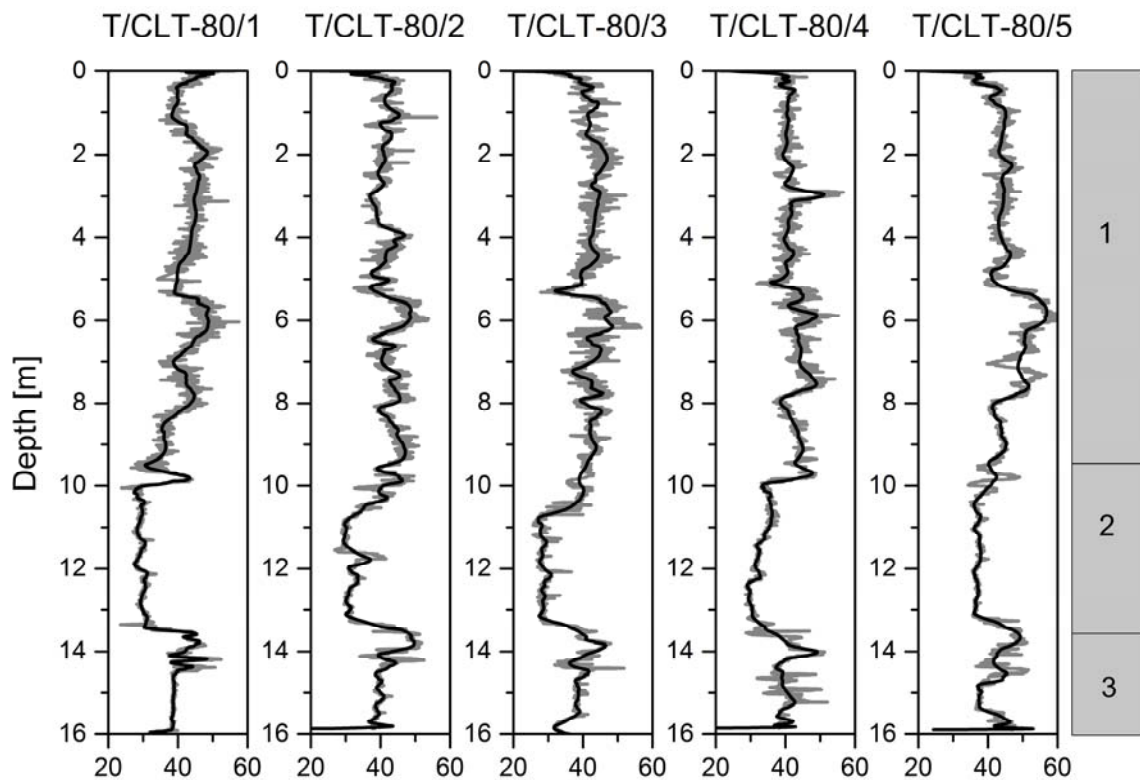


Figure 5-12: Comparison of luminosity data from CIEL\**a*\**b*\*-colour space from profiles T/CLT-80/1-5; light grey = raw data; black = using 6-level 50 % threshold DAUBLET4-denoise to the found three major stratigraphic units (T/SON-1) alluvial sand (I), till (II), clay (III); (→ Figure 5-5).

*XYZ*-tristimuli (CIE, 1931; 1978; 1996) can be used as base variables for transformation into a set of colour systems within a three dimensional space. The derived colour surrogates allow a mathematical filtering of the highly resolved data sets as pure numerical data. Depth related profiles can be plotted and stratigraphic interpretation become possible. The transformation of *in situ*-obtained *SC* into a set of colour systems is rapid and easily to applicable. The presented surrogates were found to be appropriate. We used *CIEXYZ*, *CIExyY*, *CIEL\*a\*b\**, *CIEL\*c\*h\** (CIE, 1931; 1978; 1996), and *sRGB*-colour, as well as the *RGB*-indices system to image the *SC*-distribution respective to depth (Figure 5-10).

Performing colour reduction within the *RGB*-colour space by application of the *rgb2ind*-algorithm (URL 12) is a good option for profile-based filtering. This is especially applicable if high variations and sharp colour contrasts occur, which may be directly related to certain specific layers. The main constraint is the total variation of colours within the depth profile. On the contrary, dominant colours will distort smoothing results by global colour reduction. In the sense of depth, rare appearances of certain colours will be smoothed out in this case, as they are either representative or not. Thus, spatially close colour clusters in the *RGB*-colour space require more attention during processing. Otherwise they may be lost. Logs, which obtain minor colour variability or only little contrast fluctuations require a higher number (smaller) clusters to define these slight differences than contrast-rich profiles. The combination of a moving median and colour cluster relies on the chosen pre-sets of median range and total colour number. Depending on the desired vertical resolution, they can be adjusted for an optimal smoothing of the data. The results show that the vertical part of the profile loses more detail by increasing its median range and decreasing colour numbers, as overall variation was higher in this part. Hence, the overall setting becomes more defined. Bearing this in mind, the results nonetheless provide good quantification of layering, where non-representative *SC*-information is filtered out as intended.

The application of wavelet transformation to *in situ*-obtained *SC*-data is shown to have great potential, according to the findings of COOPER AND COWAN (2009), DUCHESNE AND GAILLOT (2011), and PAN ET AL. (2008). Both the HAAR and DAUBLET4-functions are highly applicable here. Both provide good results in the sense of data denoising, and for control of the output. The HAAR-function leads to *blockier* filter results, which resultantly can *cut off* significant peaks in the data function, e.g., at 9.80–10 m depth (Figure 5-8). This method is appropriate for demonstrating wavelet properties in general, but does not have good time-frequency properties (SHUMWAY AND STOFFER, 2011) or good location-frequency properties, respectively. As such, the DAUBLET4-function is more appropriate for denoising soil colour surrogates data (Figure 5-9) and is best suited to detecting phase shifts in noisy density logs, as described in DUCHESNE AND GAILLOT (2011). All chosen *SC*-surrogates can be smoothed using this approach (Figure 5-10). This allows an enhanced interpretation of the stratigraphic

units. The layers can be more clearly defined and non-representative *SC*-data can be smoothed out. The strong modulation mainly caused by local variation in the geology setting resultantly decreases, and the data becomes more comparable. Core results reveal that major peaks correspond with stratigraphic changes (Figure 5-5; Figure 5-10).

In addition, it is possible to obtain differences between the *SC*-surrogates too. Comparison of the five repeated measurements shows significant to high correlation (Table 5-2) after denoising with DAUBLET4-function, using a 6-level 50%-threshold. The results indicate that higher variation will lead to less comparable cases of  $F$ , resulting in lower correlation coefficients. The T/CLT-80/2 and T/CLT-80/3 probings are not as reliable as the other probings, whereas the T/CLT-80/1 and T/CLT-80/5 probings show good correlation with one another. We achieved good to high correlations by comparing 1-cm depth-resolved data. Variations may depend on the geological setting and variations beyond the 1-cm resolution threshold.

*“Notice 2: This is the author’s version of a work that was submitted for publication in Vadose Zone Journal. Changes resulting from the publishing process, such as peer review, editing, corrections, structural formatting, and other quality control mechanism may not reflected in this document. Changes may have been made to this work since it was submitted for publication.”*

#### *Postscript*

*The results of this chapter deliver a processing technique for in situ-obtained soil colours. The next chapter will apply this technique for geotechnical site characterisation.*

## 6 *In situ*-obtained soil colours (SC) for geotechnical site characterisation

### Chapter Outline

*This chapter presents results from joint interpretation of in situ-obtained SC-data and state-of-the-art geotechnical DP-based profiling tools discussing the additional benefit of such data as a new proxy for geotechnical site characterisation of the near surface at the local-scale Chapter highlights include:*

- *In situ-obtained SC reflect small-scale lithological changes measured by cone penetration testing and soil sampling.*
- *In situ-obtained SC allow the characterisation of chemical states (oxidative/reductive conditions) and reflect soil moisture patterns.*
- *In situ-obtained SC deliver extra information on subsurface properties that allow enhanced profiling.*

### Preface

*We owe thanks to Dr. Thomas Vienken and Manuel Kreck (Dept. Monitoring and Exploration Technologies, UFZ Helmholtz Centre for Environmental Research) for providing the data set of dried soil samples (T/DT-2), T/SMP-1, T/SMP-2, and the corresponding CLT-log (T/CLT-6) from the Taucha test site published in VIENKEN ET AL. (2013).*

## 6.1 Introduction

The application of the *colour logging tool (CLT)* (as we have named it) contributes a new approach and data for (geotechnical) site characterisation. Hence, it is our intention to improve colour measurements by means method of application (*DP*-based, *in situ*) and data interpretation (stratigraphy, chemical state, soil moisture, etc.), which opens new fields of application and possibilities for this data.

*CLT* has great potential to become a prominent new technique that can supplement the spectrum of classical *SC*-measurement methods. As previously stated, *SC* can be used as a proxy for soil classification, e.g., in the vadose zone. The *SC*-changes may be directly associated with the vertical distribution of hydraulic properties, e.g., difference of grain sizes and therefore hydraulic conductivity, an indication of oxidative or reductive conditions, or

micro-stratification. Any change that occurs in *SC* is a useful criterion, e.g., for stratigraphic differentiation of the log data. Hence, this exhibits great potential to deliver extra information for geotechnical engineering purposes in an unconsolidated rock environment.

We intimated that site-specific prior knowledge of the geological setting is required to accurately sort colours into certain specific layers (→ Chapter 5). We provided complementary data that supplements soil-sampling results (*SONIC*). However, these sampling results sometimes lacked the requisite resolution for vertical results because of sediment compaction. Nevertheless, the tripartite layer structure (sand, till, clay) was successfully imaged by the *SC*-surrogate data.

In this chapter we will compare *SC*-data with standard *DP*-based site investigation tools such as *cone penetration testing (CPT)*, high-resolution *soil sampling (SS)*, *soil moisture probing (SMP)*, and *electrical conductivity logging (DPEC)*, gathered at the Taucha test site (→ Chapter 2.2; Figure 2-2). These tools provide high-resolution data for one-dimensional and two-dimensional profiling. After, we will discuss the additional benefits *in situ*-obtained *SC* brings for geotechnical site characterisation.

## 6.2 Methods

### 6.2.1 Cone penetration testing (*CPT*)

The fundamentals of *CPT* have been previously described. We kindly refer the reader to Chapter 4.3.5 for detailed information.

### 6.2.2 Electrical conductivity logging (*DPEC*)

*DPEC* detects electrical resistivity that relates to lithology. *DPEC* adapts the principles of D.C. geoelectrical measurements at surface level (→ Chapter 3.3.1). In the same way as D.C. geoelectrical methods, in *DPEC* two electrodes apply a current to the soil. The electrodes are part of the *DP*-probe itself. Here, two major types are used, namely ring and point electrodes. Hence, depending on the probe design, a specific array configuration is measured. In principle, the same pair of electrodes can be used for dipole array measurements, whereas the separate pair of electrodes can be used as a WENNER-array. Considering the injected current and the measured voltage with regards to the probe-specific configuration factor, the apparent electrical conductivity *EC* or  $\sigma$  (or inverse resistivity  $\rho_s$ ) can be calculated (ZSCHORNACK AND LEVEN-PFISTER, 2012A). These parameters are constantly logged with depth. As conductivity (and inverse resistivity) is related to soil types, a detailed investigation of the near surface becomes possible (CHOUKER, 1971). Generally, high

conductivity describes cohesive material, whereas low conductivity describes non-cohesive material.

The *DPEC* is often used in the initial stages of site investigation (ZSCHORNACK AND LEVEN-PFISTER, 2012A). This method is a robust tool that can distinguish between different soil types especially in the saturated zone, e.g., CHOUKER (1971), BECK ET AL. (2000), SCHULMEISTER ET AL. (2003), and SELLWOOD ET AL. (2005). Hence, *DPEC*-logs allow lower conductivity zones to be defined, equivalent to coarser grained and, therefore, more permeable sediments. These zones are important when considering hydraulic flow (SCHULMEISTER ET AL., 2004) or contaminant transport (MCCALL, 1996).

At the Taucha test site, we acquired data using the *EC*-probe *SC-500* with accessory field computer designed by *Kejr Engineering Inc. – Geoprobe Systems*, KS, USA (URL 19).

### 6.2.3 Soil moisture probing (*SMP*)

*SMP* (also known as *water content profiler*) detects *in situ* parameters that relate to soil moisture (TOPP ET AL., 1980; ROTH ET AL., 1990). EVETT ET AL. (2006), KIM ET AL. (2007), and SHINN ET AL. (1998) provided a detailed description of *SMP*. During measurement, *SMP* continuously detects the dielectric properties of the soil and the electrical resistivity  $\rho_s$  to a cm-scale. Thereof, soil moisture content  $\theta$  (volumetric water content) and porosity  $\phi$  can be obtained for the unsaturated and saturated zone, respectively. The principal relationship was initially present by TOPP ET AL. (1980). Generally, the probe is similar to the *DPEC* (see above), consisting of at least two ring electrodes. In the soil, the electrode board generates an oscillating signal between the two rings. This enables the measurement of the dielectric properties of the soil between those rings (KIM ET AL., 2007; SHINN ET AL., 1998). The frequency of the induced electromagnetic signal is >100 MHz. The measured impedance (measured in time domain - *TD* or frequency domain - *FD*) is related to the capacitance of the soil and is then transformed into dielectric permittivity values  $\varepsilon$  (ZSCHORNACK AND LEVEN-PFISTER, 2012B).

The measured dielectric permittivity values can be used to obtain *in situ* soil moisture. TOPP'S empirical formula (TOPP ET AL., 1980) is most widely used for this calculation. Here, the volumetric water content  $\theta$  is calculated from the dielectric number  $\varepsilon_c$  (Equation 6-1).

$$\theta = -5.3 \cdot 10^{-2} + 2.92 \cdot 10^{-2} \varepsilon_c - 5.5 \cdot 10^{-4} \varepsilon_c^2 + 4.3 \cdot 10^{-6} \varepsilon_c^3 \quad (6-1)$$

However, the formula according to TOPP ET AL. (1980) is purely empirical. A bias exists between mineral and organic soils. A third order polynomial function is useful to describe water contents in a range of  $0 \leq \theta \leq 0.5$ . In contrast, the CRIM-formula (*complex refractive index method*; ROTH ET AL., 1990) is physically-based and thus allows a calculation of water content for the whole range ( $0 \leq \theta \leq 1.0$ ). The formula describes wet (moist) soil in

the form of a three-phase system, where  $\phi$  is the soil's porosity,  $1 - \phi$ ,  $\theta$  the volumetric water content, and  $\phi - \theta$  are volumetric fractions (equation 6-2). The terms  $\varepsilon_s$ ,  $\varepsilon_w$ , and  $\varepsilon_a$  are the dielectric numbers of the solid, the aqueous, and gaseous phase, respectively.

$$\varepsilon_c = (\theta \varepsilon_w^\alpha + (1 - \phi) \varepsilon_s^\alpha + (\phi - \theta) \varepsilon_a^\alpha)^{1/\alpha} \quad (6-2)$$

Following ROTH ET AL. (1990) and others, alpha can be assumed in a three-phase system as being  $\alpha = 0.5$ . Furthermore, the dielectric number of the gaseous phase is set to the constant value of  $\varepsilon_a = 1$ . Hence, we can simplify the equation (6-2) into equation (6-3).

$$\theta = \frac{\sqrt{\varepsilon_c} - \sqrt{\varepsilon_s(1-\phi)} - \phi}{\sqrt{\varepsilon_w} - 1} \quad (6-3)$$

The dielectric number of the solid phase  $\varepsilon_s$  varies between 5–8. Values for porosity  $\phi$  can be either detected on undisturbed core samples or must be assumed using reference values. The dielectric number of water  $\varepsilon_w$  is around 80, however it is sensitive to temperature. To consider the groundwater temperature, we apply a temperature correction according to KAATZE (2007) (equation 6-4), where  $a = 78.35$ ,  $T_0 = 298.15 \text{ K}$ , and  $b = -4.55 \cdot 10^{-3}$ . Term  $T$  is the groundwater temperature, which is mostly similar to the average yearly temperature, e.g.,  $10^\circ\text{C}$ .

$$\varepsilon_w = a \cdot \exp(b(T - T_0)) \quad (6-4)$$

At the Taucha test site, we acquired data with the *SMP*, designed by *Geomil Equipment BV.*, The Netherlands (URL 7), which was then extended to a *CPT*-probe ( $\rightarrow$  Chapter 4.3.5). Similar to the *CPTU*, the *SMP* operates by applying static pressure on the probe.

#### 6.2.4 Colour logging tool (*CLT*)

The fundamentals of *CLT* have been previously described. We kindly refer the reader to ( $\rightarrow$  Chapter 5) for detailed information. Accordingly, we processed the data applying the *wavelet transformation (WT)* approach ( $\rightarrow$  Chapter 5.4.9).

#### 6.2.5 Soil sampling (*SS*)

The basics of *DP*-based *SS* have been previously described. We kindly refer the reader to ( $\rightarrow$  Chapter 3.3.5) for more detailed information.

At the Taucha test site, we used *SONIC*-equipment designed by *SonicSampDrill BV.*, The Netherlands (URL 18) and the *DT22 SS*-system designed by *Kejr Engineering Inc. – Geoprobe Systems*, KS, USA (URL 5).

The *DT22*-method gathers 1.22-m core sections in plastic tubes (liner) with an inner diameter of approx. 3.3 cm. Liners were covered with plastic caps after excavation. In the

laboratory, core T/DT-1 was sliced open horizontally. Then we took core photos under almost constant light conditions. Finally, the core samples were analysed manually to ascertain grain size distribution and layer thickness.

For core T/DT-2 we used a bigger liner (inner diameter: 4.96 cm). This was pre-cut into 10-cm sections for sampling, which allowed the determination of gravimetric water content  $\omega$ . Therefore, the samples were weighted before and after 12 hours of 110°C oven drying (VIENKEN ET AL., 2013).

## 6.3 Results

Besides the colour measurements, we performed several other *DP*-probing (*CPT*, *DPEC*, *SMP*, *DT*) for ground truthing. Figure 2-2 plots the position of each probing and the diameter of the cluster. Investigations depths and additional ground water levels are summarised in Appendix B.

### 6.3.1 Comparison of *CLT*-data with cone penetration testing (*CPT*) and soil sampling (*SS*)

We performed *SONIC*-soil sampling (T/SON-1) to a depth of 16 m within <1-m distance of the soil colour measurements (Figure 2-2). In total, we found three major units, which can be described as (I) alluvial sand (0–9.40 m), (II) till (9.40–13.63 m), and (III) clay (13.63–15.20 m). The *misfit* that occurs in the final is attributable to core loss and compaction during sampling (due to the method used).

The interpretation of the corresponding *CPT*-log (T/CPT-1) according to ROBERTSON ET AL. (1986) also shows a clear layering structure (Figure 6-1). Thus, we can divide the three major units into a set of sub-layers. We obtain more precise data in the *CPT*-log (useful for interpretation with regard to lithology), because of constant logging. In total, 14 layers are delineable and are listed by depth and substrate in Table 6-1.

The upper alluvial sand (I) can be subdivided into 8 layers. The layers 1 to 3 (0–8.26 m) are composed of sands and silty sands. Then, we observe a decrease in grain size. In the layers 4 to 6 (8.27–9.17 m), there are mixtures of silty sand to sandy silt with interbedded more clayey sections. Layer 7 (9.18 – 9.49 m) consists of sensitive fine-grained material. This is the lowest layer of the alluvial sands. Therefore, we can draw a main geologic boundary at 9.50-m depth (10 cm deeper than measured by T/SON-1).

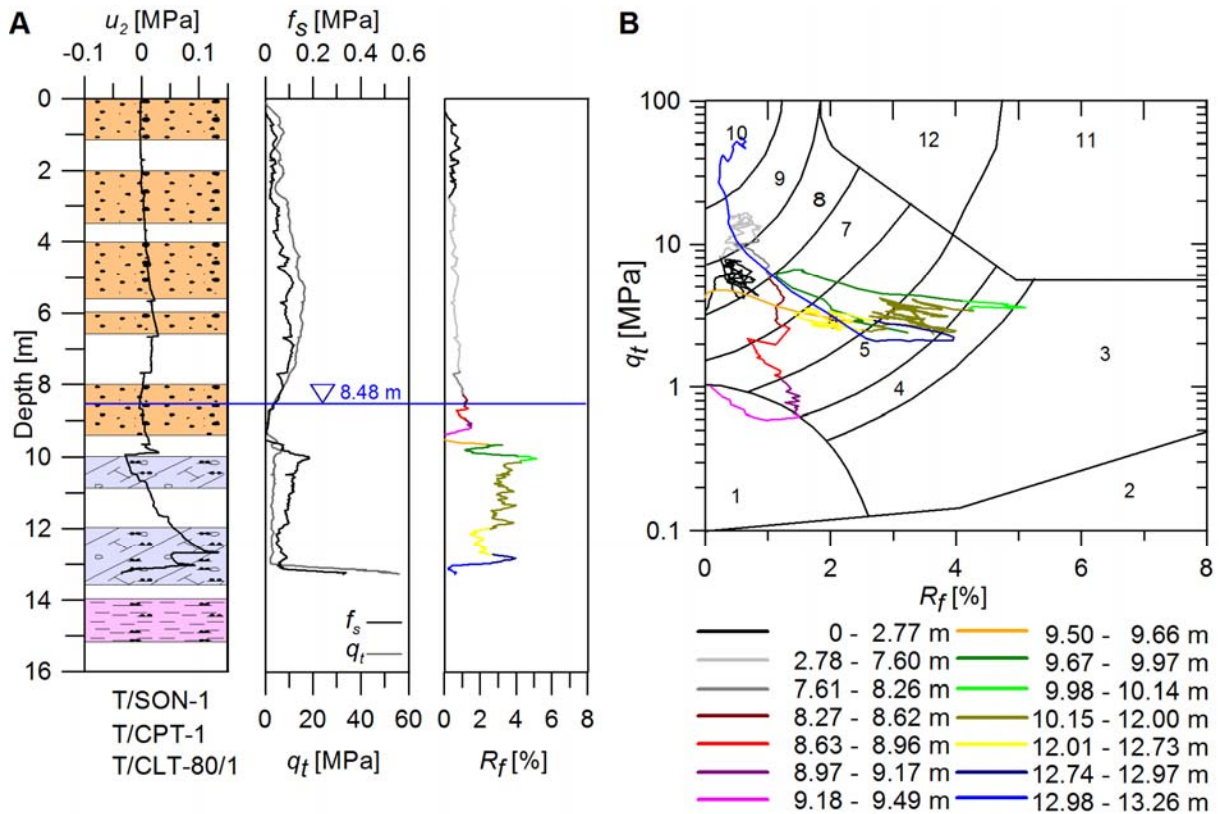


Figure 6-1: Results from *CPT* (T/CPT-1) and *SS* (T/SON-1); A) Dynamic pore water pressure  $u_2$ , sleeve friction  $f_s$ , corrected cone resistance  $q_t$ , and friction ratio  $R_f$  (color coded to interpretation in B) and core results (green = silt, orange = dominantly sandy, white = core loss/no data); groundwater level in borehole at 8.48 m depth; B) color coded lithological interpretation from ratio between corrected cone resistance  $q_t$  and friction ratio  $R_f$  according to ROBERTSON ET AL. (1986); 1 - sensitive fine grained, 2 - organic material, 3 - clay, 4 - silty clay to clay, 5 - clayey silt to silty clay, 6 - sandy silt to clayey silt, 7 - silty sand to sandy silt, 8 - sand to silty sand, 9 - sand, 10 - gravelly sand to sand, 11 - very stiff fine grained\*, 12 - sand to clayey sand\* [\*over-consolidated or cemented].

Table 6-1: Geological setup at Taucha test site derived from *CPT*-log T/CPT-1 (interpreted according to ROBERTSON ET AL. (1986) -Figure 5-7); \*end of log.

| No. | Depth [m]      | Substrate  |
|-----|----------------|--|
| 1   | 0 – 2.77       | sand – silty sand  |
| 2   | 2.78 – 7.60    | sand   |
| 3   | 7.61 – 8.26    | sand – silty sand  |
| 4   | 8.27 – 8.62    | silty sand to sandy silt   |
| 5   | 8.63 – 8.96    | sandy silt – clayey silt   |
| 6   | 8.97 – 9.17    | clayey silt – silty clay   |
| 7   | 9.18 – 9.49    | sensitive fine grained   |
| 8   | 9.50 – 9.66    | sand – silty clay (transition zone)                                |
| 9   | 9.67 – 9.97    | clayey silt – silty clay   |
| 10  | 9.98 – 10.14   | silty clay to clay   |
| 11  | 10.15 – 12.00  | silty clay – silty sand – silty clay (transition zone)             |
| 12  | 12.01 – 12.73  | sandy silt – clayey silt   |
| 13  | 12.74 – 12.97  | clayey silt – silty clay   |
| 14  | 12.98 – 13.26* | clayey silt – silty clay – gravelly sand – sand (transition zone)* |

As previously discussed, the till layer generally shows higher grain size variation (Figure 5-5). According to the *CPT*-results, the till package can be subdivided into 7 sub-layers. The till section (II) begins with a transition zone which is represented by layer 8 (9.50–9.66 m), composed of a broad grain size variety (sand to silty clay). The layers 9 to 14 are mainly composed of mixtures from cohesive materials. This silty and clayey matrix includes sandy sections and gravel pebbles (observed in soil samples).

However, we still have not reached the lower clay unit (III), the *CPT*-log only deliver high-resolution lithological information for the upper two major geologic units (I) and (II). Groundwater was measured at 8.48-m and 8.15-m depths for the T/SON-1 and T/CPT-1-log, respectively (→ Appendix B).

Core T/DT-1 was sliced open horizontally in the laboratory. Thus, we obtained detailed information about small-scale layering and, furthermore, related *SC*. Generally, we obtained (light) red-brown colours in the upper part (0–1.90 m) of the alluvial packages (I). Then, the sand shows bright colours (light olive, light yellow, white). We can follow this bleached section to the boundary of the underlying till. However, we obtain high variation of *SC* (and related grain sizes) between 8.05–8.64-m depths. We could not accurately measure the groundwater after coring. However, we obtained a wet section starting at 8.20-m depth, limited at 9.40 m. This corresponds to the previously observed groundwater level measurements from *SONIC* (8.48 m) and *CPT* (8.15 m). Hence, we interpret this local high variation of colours as the transition between oxidative and reductive conditions controlled by changing groundwater level. Beneath 8.64-m depths (down to 9.49 m), we obtained bleached sands in the saturated zone which represent reductive conditions. In the core, we could delineate the beginning of the till layer (II) at a depths of 9.45 m. This corresponds well with the *CPT*-log (9.49-m depth). The till generally shows darker colours. The upper part (9.45–9.76 m) shows reddish (rusty) colours. Then, we observe several layers composed of the same material, but with different colours (dark-brown, dark-grey); whereas dark-grey is dominant to a depth of 11.98 m. Then, we obtain mainly light grey to a depth of 13.79 m. The clay layer (III) has changing coloured layers, ranging from light grey, grey, to first light blue. However, these are just nuances of brightness, while the general colour of the clay is grey.

Figure 6-2 plots luminosity  $L^*$  and chroma  $c^*$  to grain size distribution and core photos from DT22 (T/DT-1) for selected profile sections. Figure 6-3 shows a comparison of *CPT*-data to the corresponding soil colour surrogates (→ Figure 5-10). Thus, we obtain a good fit for the major peaks, indicating lithological changes. Both figures (total log, sections) illustrate that that *SC*-changes relate to grain size. Thus, general stratigraphic interpretation becomes possible and delivers extra information on the lithological log.

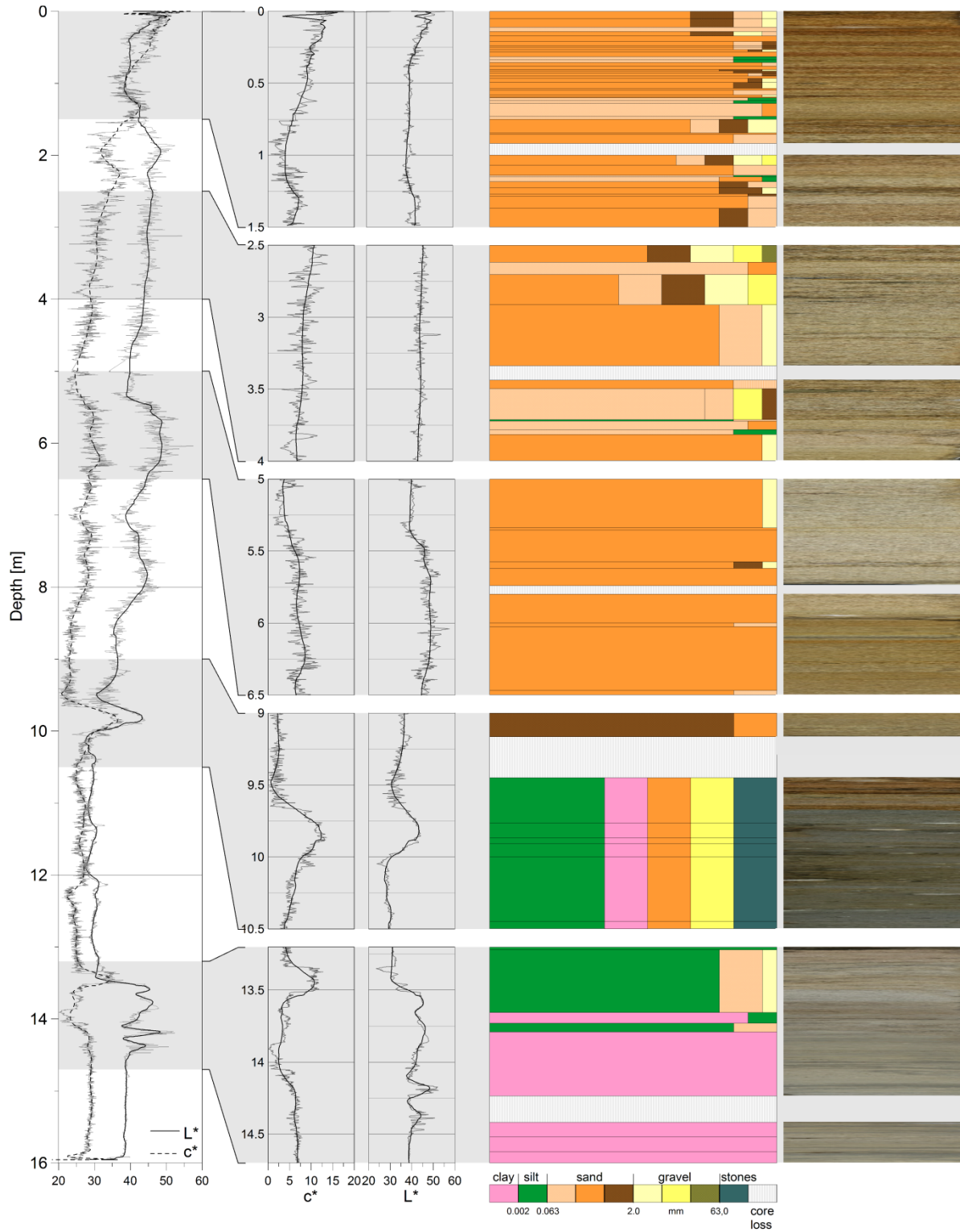


Figure 6-2: Comparison smoothed *SC*-data (luminosity  $L^*$ ; chroma  $c^*$ ) using 6-level 50%-threshold DAUBLET4-denoise (T/CLT-80/1) to grain size distribution and core photos results from DT22 (T/DT-1) for selected profile sections.

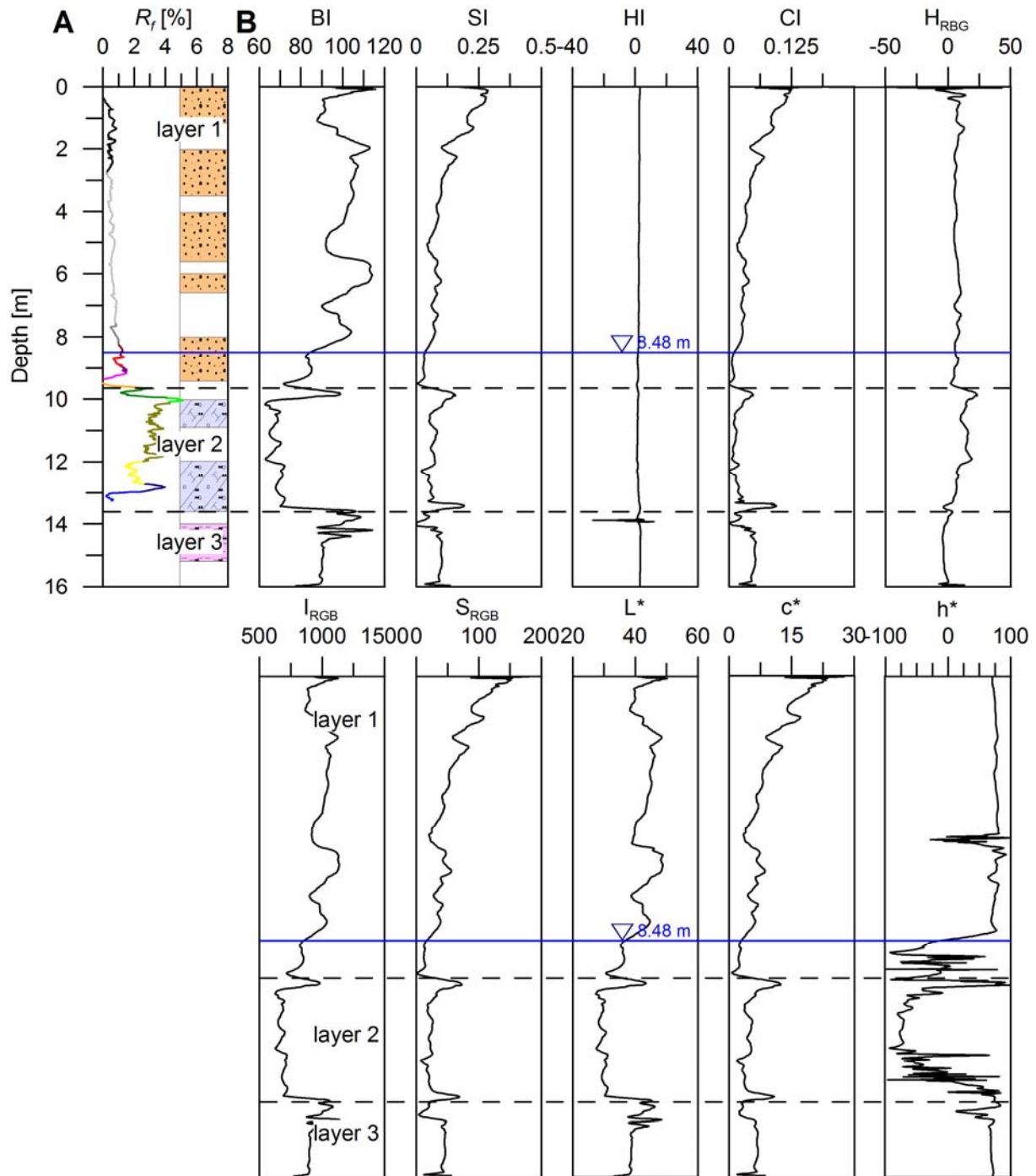


Figure 6-3: Comparison of smoothed *SC*-surrogates using 6-level 50%-threshold DAUBLET4-denoise (T/CLT-80/1) to results from *CPT* (T/CPT-1) and *SS* (T/SON-1) (Figure 6-1);  $R_f$  – friction ratio;  $sRGB$ -colour space: *BI* – brightness index, *SI* – saturation index, *HI* – hue index, *CI* – colouration index,  $H_{RGB}$  – decorrelated hue,  $I_{RGB}$  – decorrelated light intensity,  $S_{RGB}$  – decorrelated saturation; CIEL\* $c^*h^*$ -colour space:  $L^*$  - luminosity,  $c^*$  - chroma,  $h^*$  - hue angle.

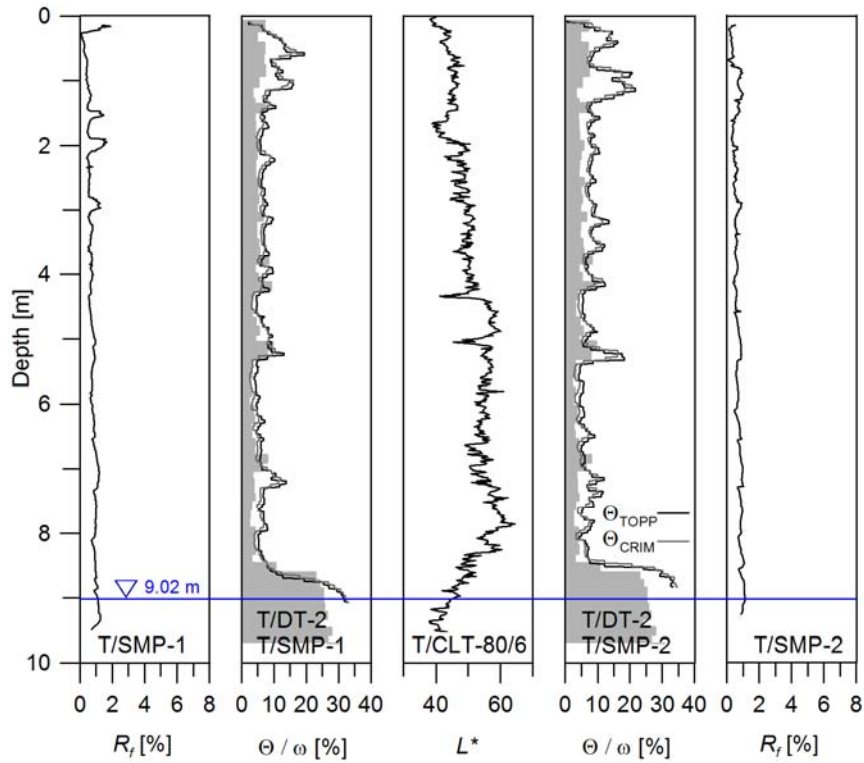


Figure 6-4: Comparison of volumetric water content  $\Theta$  from *SMP*-data (T/SMP-1; T/SMP-2) and gravimetric water content  $\omega$  from *SS* (T/DT-2) (both from VIENKEN ET AL., 2013) to *SC*-surrogate luminosity  $L^*$  (CLT-80/6, raw data).

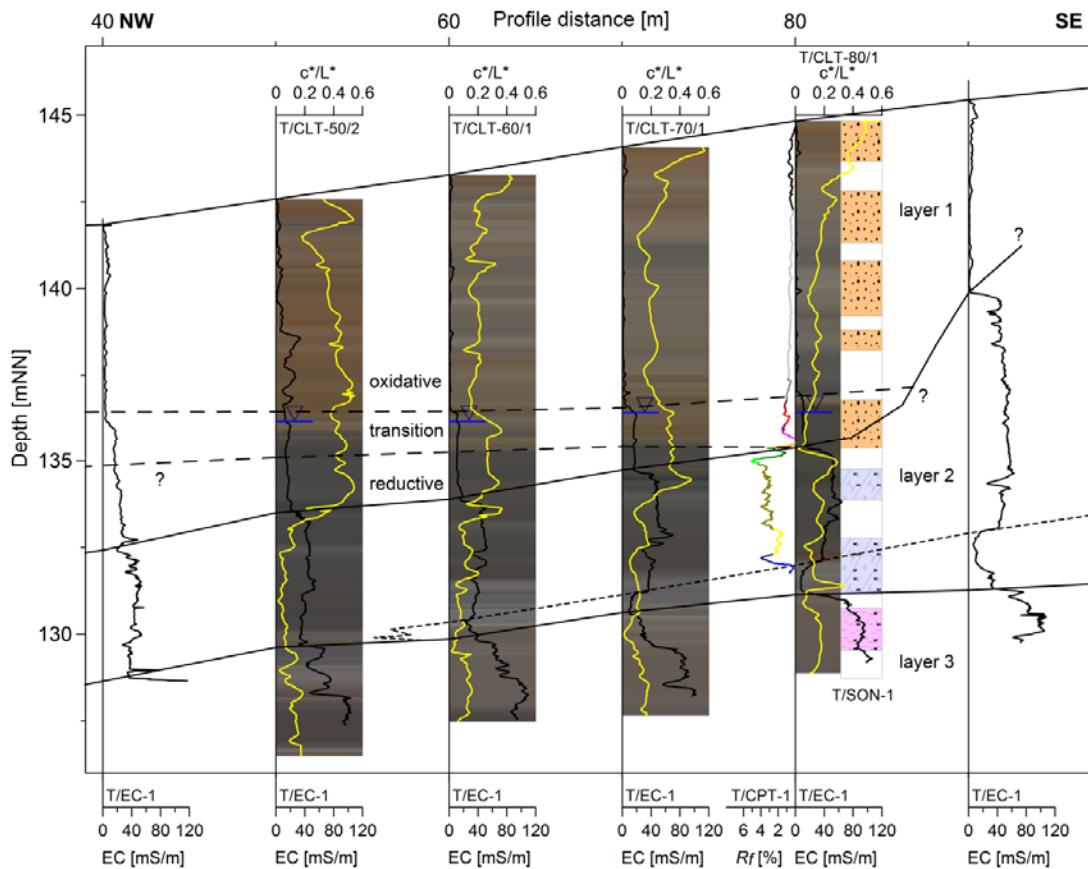


Figure 6-5: Mapped profile (layers, oxidative boundary) at Taucha test site obtained from joint interpretation of *CLT* and *DPEC*-data (supported by *CPT* and *SS*; Figure 6-3); proportion of horizontal to vertical section 1:2.

### 6.3.2 Comparison of *CLT*-data with soil moisture probing (*SMP*)

For comparison of *in situ*-obtained *SC* to *in situ* moisture conditions, we performed two independent investigations of water content (*SMP*, *DT*) in the upper alluvial sands (I) (VIENKEN ET AL., 2013). These were then compared with colour data gathered on the same day. As can be seen in Figure 6-5, the sands show variation in water content with depth. The applied formulas according to TOPP ET AL. (1980) and CRIM (ROTH ET AL., 1990) show the same moisture distribution. Groundwater was measured at 9.02-m. The volumetric water content  $\omega$  (oven-dried samples along 10-cm section) generally shows the same moisture pattern. However, in the upper part, the water content is underestimated when compared with *SMP*-results. Subsequently, we plotted luminosity data to the soil moisture data. Luminosity generally decreases with increasing soil moisture. As previously discussed, the alluvial sands show four differently coloured sections. These are 0–1.9-m section (red-brown colours), 1.90–8.05-m section (bleached), 8.05–8.64-m section (high colour variation, wet  $\rightarrow$  transition zone between oxidative/reductive conditions), and the 8.64–9.49-m section (bleached, reductive zone). Following this interpretation from the core log (T/DT-1), our subsequent analysis of soil moisture data compared with luminosity showed a good fit. The luminosity of the upper 1.9-m section is lower (darker) than the lower log. This corresponds to the measured high soil moisture. Then soil moisture decreases as does luminosity. Small-scale increases of soil moisture ( $\sim 4$ ;  $\sim 5.1$ , and  $\sim 7.2$  m) cause a reduction in luminosity. While soil moisture constantly increases in the capillary fringe, luminosity follows the opposite trend, as expected. Thus, we can delineate the capillary fringe also by using colours. The upper limit of the capillary fringe corresponds to the transition zone of oxidative/reductive states (high colour variations). However, compared with older log data (Figure 6-2; Figure 6-3), this changes with depth because of different ground water levels. This also helps illustrate groundwater dynamics at the test site between the measurement dates.

### 6.3.3 Comparison of *CLT*-data with electrical conductivity logging (*DPEC*)

With regards to two-dimensional mapping of site-specific stratigraphy, we compared *DPEC*-measurements with *CLT*-results (supported by *CPT* and *SS*). As Figure 6-5 shows, we can use information from this comparison to characterise layer structures of the subsurface. Following CHOUKER (1971), high electrical conductivity values indicate fines (clay, silt), which decrease as grain size increases. In our logs, the alluvial sands (I) generally have low electrical conductivity. However, the data sections we obtained were of low data quality, due to dry conditions. With increasing soil moisture, we can delineate the capillary fringe in the lowest part of the sand layer. The geological boundary to the lower till layer (II) is indicated by an increase in conductivity. Accordingly, we obtain highest conductivity data in the clay

(III). Because of the high data resolution (1 cm) in the *DPEC*-log, it is possible to observe a sub-layer in the till above the clay. This zone, shows lower conductivity values than the rest of the till layer, indicating a higher amount of sand in this section (small-dashed line). Thus, we combine the interpreted one-dimensional logs to achieve a two-dimensional cross section. In total, we use six *DPEC*-logs, gathered 10-m distance apart from each other.

The three major layers have equidistant layer thicknesses along the lower part of the profile (40–80 m). Between 80–90 m, the till layer increases rapidly with depth. This deformation is typical for the end moraine facies and represents clinching, squeezing, and pushing processes the accumulation of the tills at the former crystalline hill barrier (→ Chapter 2.2).

Subsequently, we can add additional information from *in situ*-obtained *SC*. In Figure 6-5, we plot the ratio between chroma  $c^*$  and luminosity  $L^*$  and the corresponding *RGB*-chart (smoothed colour surrogates using a 6-level 50%-threshold DAUBLET4-denoise). Thus, we see qualitatively high concordance to the *DPEC*-logs. This supports the interpretation of the three major geologic boundaries. Furthermore, we can add boundaries (dashed lines) that characterise vertical extent of the oxidative and reductive zone. Here, the upper boundary (transition/oxidative) corresponds to the *DPEC*-delineated capillary fringe. The *term transition* zone was chosen to describe the part of the log, where we obtain the highest colour variation, which shows the presence of oxidative and reductive boundaries lying upon each other that depend on small-scale grain size variations, as previously discussed for core (T/DP-1). In the *SC*-plot, we see more variation. This allows a more detailed delineation of layers than just for the three major units. However, this was not interpreted in detail here.

## 6.4 Discussion

Comparison of the data obtained by *colour logging tool (CLT)* - processed by the previously presented denoising strategy (→ Chapter 5) - with *state-of-the-art* site characterisation tools and techniques showed, that this data (1) corresponds to stratigraphic information of the subsurface (small-scale, large-scale) and (2) provides additional information. The colour information allows a reliable interpretation of on-site subsurface features (layers). At the Taucha test site, we could characterise the three major geological units, which are (I) alluvial sand, (II) till, and (III) clay. These units contrast greatly, in both lithology and colours observed/presented.

When we compared *CLT*-logs with *cone penetration testing (CPT)* results and *soil sampling (SS)* (addressed to grain size and *SC*) results, they corresponded well with each other (Figure 6-2; Figure 6-3). This allows a more detailed characterisation of single layer properties to be made, and enables general stratigraphic site investigation. The *CPT*-data is

interpretable for lithological information according to ROBERTSON ET AL. (1986). Thus, we found 14 different layers. However, in areas of constant lithology, *SC* (and its surrogates) is useful to delineate zones within the uniform lithological block. In these depth-sections, the colour data indicates a different chemical state and/or soil moisture increase/decrease, whereas grain size distribution has no influence.

Comparing *SMP*-data (*soil moisture probe*) and lab-samples to colour logs, we found evidence of how soil moisture influences the luminosity of the soil (Figure 6-4). Increasing soil moisture, e.g., in the capillary fringe, causes a decrease in luminosity. Small-scale variations of soil moisture changes were also observed, due to high-resolution measurement methods employed. Hence, soil colour can be used as an indicator of *in situ* soil moisture patterns.

The comparison of *DPEC*-measurements (*electrical conductivity logging*) and *CLT*-logs for two-dimensional profiling helped reveal the additional benefits that colour data can provide (Figure 6-5). Here, we could successfully delineate zones of opposite chemical states (oxidative/reductive) by interpreting the occurrence of reddish and grey colours. From one-dimensional interpretation, we were able to analyse this variation in two dimensions (cross section). This example also highlights the potential of such investigations for monitoring the vertical and lateral shift of these zones by performing repeated measurements over time.



---

## 7 Conclusion

### *Preface*

*This chapter concludes the findings of the thesis. The second paragraph, which describes the multi-method investigation at the Löbnitz test site bases on the publication HAUSMANN ET AL (2013), → Notice 1 in Chapter 3. The fourth paragraph presents improvements of direct data acquisition, numerical transformation, filtering, and interpretation bases on the submitted manuscript HAUSMANN ET AL (SUBMITTED), → Notice 2 in Chapter 5.*

The past few decades have seen the rapid development of *engineering geophysics (EG)* and *direct push technologies (DPT)*, allowing better measurement of the relevant parameters for geotechnical site investigation. Thus, following the general trend of applying an inter-disciplinary approach of direct/indirect exploration of the near surface, this thesis focuses on a joint application and, indeed, further development of such technologies and data processing. Consequently, we tested integrated site investigation approaches at selected test sites (Löbnitz and Taucha), which represent typical construction grounds in Central Germany. In this course of out testing, we performed intensive fieldwork.

We present the results of a multi-method investigation of structural features of an abandoned meander of the River Mulde at the Löbnitz test site using *electrical resistivity tomography (ERT)*, *ground penetrating radar (GPR)*, *refraction seismic (RS)*, and *multichannel analysis of surface waves (MASW)*. By combining these methods, we were able to characterise and delineate all subsurface features of the abandoned meander, including a point bar, a channel, a cut bank, and the structure of the infill area. Comparison of results from each method helps support our particular findings concerning the subsurface characteristics of the meander. Using the same survey line, the results of the *ERT* and *GPR*-methods show differences compared to seismic methods, especially for depth resolution and imaging of the channel's internal structures. Joint interpretation of the *ERT* and *GPR*-data helps solve any uncertainties concerning near-surface structures. Even though both methods did not reach the intended target depth, we can delineate the shape of the infilling of the abandoned channel, providing some spatial information about its lateral and horizontal extent. Low electrical resistivities of the saturated sands and gravels, the lack of dielectrical contrasts, as well as the insufficient penetration depth of the applied antenna frequency prevented the detection of deeper subsurface layers using *ERT* and *GPR*-methods. However, the *ERT* and *GPR*-images correlate well with the infill structure mapped by *MASW*. The *RS* and *MASW*-data reveal a similar trend of high velocities. Via *DP*-based core samplings, we

can correlate these high velocities with gravelly sediments and validate the findings of the seismic methods. The *RS*-were unable to detect inverse velocity layers of the infilling or the path because of methodical limitations. The *MASW*-results show a laterally and vertically more heterogeneous spatial distribution of velocity structures, in which the findings from sonic core sampling fit reasonably well. Although the measured physical properties of each technique do not correspond to certain materials, a qualitative interpretation of subsurface features based on combined geophysical methods is a powerful tool for the characterisation of geomorphological structures, given their non-invasive and time/cost-efficient nature. Any disadvantages of a single method can be compensated for by using a combined interpretation of the different geophysical techniques. Additional information from core samples is indispensable for validation and classification of the results. We find that *MASW* in particular delivers extra detailed information about the channel's internal structure with respect to lateral and vertical resolutions. This significant benefit may advance the use of this method in site investigations focused on imaging subsurface structures. Results from this method expand upon the data obtained from *RS*-surveys without any considerable additional cost, time, or personnel expenditure. Existing *RS*-data sets can also be analysed with respect to surface waves. The results of this multi-method investigation provide detailed knowledge about the subsurface structures at the test sites. We used this data for interpretation of results from *seismic traveltime tomography (STT)*.

Inversions of first break traveltimes from *STT* provide detailed models of the variability of seismic velocities at the Löbnitz test site. The combined recording of P- and S-wave velocity and the resulting velocity models allow for estimation of highly-detailed geotechnical parameter patterns (elastic moduli, water content, etc.). This novel method developed for mobile *DP*-based near-surface P- and S-wave tomography has the potential to enhance geotechnical site characterisation. The use of temporary-installed boreholes helps us to overcome the restrictions imposed by existing on-site boreholes. This supplements existing general advantages of *DPT* – namely speed of measurement, cost effectiveness, field site accessibility, and on-site decision-making. The joint inversion of seismic traveltime data with the *particle swarm optimization (PSO)* approach allows an appraisal of uncertainty to be made for final model ensembles. As such, a reliable calculation of two-dimensional high-resolution parameter distributions for geotechnical site assessment becomes possible, and can be further supplemented by *DP*-based *in situ* data or soil sampling. This technical development encourages the use of *in situ* prediction of geotechnical parameters for geophysical site investigation, especially for appraising information uncertainty, which still remains a challenge when undertaking an objective geotechnical risk analysis.

The rapid and high-resolution *DP*-based *colour logging tool (CLT)* helps bridge the gap between classical soil sampling and *ex situ* soil colour (*SC*) determination using colour

charts, handheld colorimeter, or laboratory methods. Transformation of the raw data into the standardised colour systems allows numerical comparison of the depth-related profiles. The resolution of the gathered data is much higher than when using the classical approaches and requires advanced data processing (denoising approaches) to be applied. The application of wavelet transformation, median filtering, and the colour reduction algorithm to *in situ*-obtained *SC* leads to reliable and repeatable results. The tested filter approaches work rapidly, effectively, and are easy to apply. The methods have been found to be appropriate for the transformation of *SC* into comparable numerical surrogates, to downscale high-resolution data, resulting in an increase in interpretation certainty that corresponds well with soil sampling data. The presented approach enhances the *DP*-based characterisation of *in situ*-obtained *SC*-measurements under natural conditions and enlarges the methodological spectrum for *SC*-measurement in the near surface. *SC* can be used as a proxy for stratigraphic interpretation of the near surface. This measurement method and the suggested processing provide repeatable data sets for a range of various tasks, e.g., for modelling. In contrast to classical *SC*-detection approaches, the presented probe delivers high-resolution data for the characterisation of the near surface. Furthermore, the smoothing approach has a wide application capacity and could be used on any other *DP*-based high-resolution data set.

We present our results from joint interpretation of *in situ*-obtained *SC*-data and *state-of-the-art* geotechnical *DP*-based profiling tools discussing the additional benefit of such data for geotechnical site characterisation of the near-surface. The comparison of *SC*-data (and their surrogates) to data from *cone penetration testing (CPT)*, *soil sampling (SS)*, *soil moisture probing (SMP)*, and *electrical conductivity logging (DPEC)* helps show that this data provides additional information on small-scale lithological changes, chemical states (oxidative/reductive conditions), soil moisture, and allow enhanced profiling. This opens potential new areas of application and new outputs for such data. Hence, this method has great potential to provide extra information for geotechnical engineering purposes in an unconsolidated rock environment. However, interpreting *CLT*-data as a single application remains challenging. Thus, additional information, such as site-specific prior knowledge of the geological setting, is required to accurately sort *SC* into certain specific layers.

We conclude that the techniques used from *engineering geophysics* and *direct push technologies* and the joint interpretation of the results helps increase knowledge of the spatial distribution of geotechnical parameters in the near surface. We showed that the geophysical methods have the important advantage of enabling ground characterisation with relatively little effort. The applied *DP*-tools help to supplement (ground truth) these geophysical data sets and are applicable as carrier devices, which can be used for the creation of new high-resolution data sets for geotechnical site characterisation. The *in situ*-measured data provide numerous advantages over traditional drilling methods. This in turn supplements the existing

general advantages of *direct push technologies* – namely speed of measurement, time/cost effectiveness, field site accessibility, and on-site decision-making. The selected approaches are applicable to support and/or substitute common geotechnical surveying and analysis tools such as drill logs and lab analysis, which are essential for a thorough assessment of construction sites. The application and technical developments of *engineering geophysics* and *direct push technologies* in this thesis (used for *in situ*-recording of geotechnical parameters for geotechnical site investigation) encourage the reliable characterisation of highly heterogeneous ground and are especially useful for appraising information uncertainty, which still remains a challenge of delivering objective geotechnical risk analysis at different scales in one, two, and three dimensions. Compared with traditional, limited geotechnical measurements methods, these methods provide further information, which allows us to clearly define homogeneous sections (layers). The combined data interpretation approach compensates for any disadvantages of a single method. Thus, we expect a significant positive impact for near-surface characterisation in the frame of engineering geological investigations.

---

## References

### A

- Anderson, K.B., Spotila, J.A., Hole, J.A., 2003. Application of geomorphic analysis and ground-penetrating radar to characterization of paleoseismic sites in dynamic alluvial environments: an example from southern California. *Tectonophysics*, 368(1-4), 25-32.
- Angioni, T., Rechten, R.D., Cardimona, S.J., Luna, R., 2003. Crosshole seismic tomography and borehole logging for engineering site characterization in Sikeston, MO, USA. *Tectonophysics*, 368(1-4), 119-137.
- Ahuja, N., Lertrattanapanich, S., Bose, N.K., 2005. Properties determining choice of mother wavelet. *IEE Proc.-Vis. Image Signal Process.*, 152(5), 659-664.

### B

- Bano, M., Marquis, G., Niviere, B., Maurin, J.C., Cushing, M., 2000. Investigating alluvial and tectonic features with ground-penetrating radar and analyzing diffractions patterns. *J. Appl. Geophys.*, 43(1), 33-41.
- Barrett, L.R., 2002. Spectrophotometric color measurement in situ in well drained sandy soils. *Geoderma*, 108(1-2), 49-77.
- Barrón, V., Torrent, J., 1986. Use of the Kubelka—Munk theory to study the influence of iron oxides on soil colour. *J. Soil. Sci.*, 37(4), 499-510.
- Becht, A., Appel, E., Dietrich, P., 2006. Analysis of multi-offset GPR data: a case study in a coarse-grained gravel aquifer. *Near Surf. Geophys.*, 4(4), 227-240.
- Beck, F.P.J., Clark, P.J., Puls, R.W., 2000. Location and characterization of subsurface anomalies using soil conductivity probe. *Ground Water Monit. R.*, 55, 55-59.
- Becker, M., 2012. Vorratsabschätzung für die Tongrube Taucha mittels 3D-Modellierung anhand von Bohrergebnissen und geophysikalischen Datenmaster, Universität Leipzig, Leipzig, 119 pp.
- Ben-Dor, E., Heller, D., Chudnovsky, A., 2008. A novel method of classifying soil profiles in the field using optical means. *Soil Sci. Soc. Am. J.*, 72(4), 1113-1123.
- Bennett, M.R., Cassidy, N.J., Pile, J., 2009. Internal structure of a barrier beach as revealed by ground penetrating radar (GPR): Chesil beach, UK. *Geomorphology*, 104(3-4), 218-229.
- Blavet, D., Mathe, E., Leprun, J.C., 2000. Relations between soil colour and waterlogging duration in a representative hillside of the West African granito-gneissic bedrock. *Catena*, 39(3), 187-210.
- Boniger, U., Tronicke, J., 2010. Integrated data analysis at an archaeological site: A case study using 3D GPR, magnetic, and high-resolution topographic data. *Geophysics*, 75(4), B169-B176.
- Boxberger, T., Picozzi, M., Parolai, S., 2011. Shallow geology characterization using Rayleigh and Love wave dispersion curves derived from seismic noise array measurements. *J. Appl. Geophys.*, 75(2), 345-354.
- Bridge, J., Collier, R., Alexander, J., 1998. Large-scale structure of Calamus River deposits (Nebraska, USA) revealed using ground-penetrating radar. *Sedimentology*, 45(6), 977-986.
- Breul, P., Gourves, R., 2006. In field soil characterization: Approach based on texture image analysis. *J. Geotech. Geoenviron. Eng.*, 132(1), 102-107.
- Brouwer, J.J.M., 2007. In-situ soil testing. Lankelma, East Sussex.
- Bucholtz, F., Nau, G., Aggawal, I.D., Sanger, J.S., Ewing, K.J., 1998. Fiber optic infrared cone penetrometer system. Patent US005739536 A, pp. 16.
- Burger, H.R., Sheehan, A.F., Jones, C.H., 2006. Introduction to Applied Geophysics. W. W. Norton & Company, New York London.
- Butler, D.K., 2005. Near-Surface Geophysics. Society of Exploration Geophysics - SEG, Tulsa, OK.
- Butler, J.J. Jr., Healey, J.M., Zheng, L., McCall, W., Schulmeister, M.K., 1999. Hydrostratigraphic characterization of unconsolidated alluvial deposits with direct-push sensor technology, Kansas Geological Survey.
- Butler, J.J. Jr., 2005. Hydrogeological methods. In: Y. Rubin, S. Hubbard (Eds.), *Hydrogeophysics*. Springer, Dordrecht, pp. 23-58.

### C

- Campanella, R.G., Weemees, I., 1990. Development and Use of an Electrical-Resistivity Cone for Groundwater Contamination Studies. *Can. Geotech. J.*, 27(5), 557-567.

- Cardarelli, E., Cercato, M., Cerreto, A., Di Filippo, G., 2010. Electrical resistivity and seismic refraction tomography to detect buried cavities. *Geophys. Prospect.*, 58(4), 685-695.
- Chambers, J.E., Wilkinson, P.B., Wardrop, D., Hameed, A., Hill, I., Jeffrey, C., Loke, M.H., Meldrum, P.I., Kuras, O., Cave, M., Gunn, D.A., 2012. Bedrock detection beneath river terrace deposits using three-dimensional electrical resistivity tomography. *Geomorphology*, 177, 17-25.
- Christy, C.D., Christy, T.M., Wittig, V., 1994. A percussion probing tool for direct sensing of soil conductivity, *Geoprobe Systems Technical Paper No. 94-100*.
- Chouker, F., 1971. Methodische und theoretische Untersuchungen zur geophysikalischen Grundwasseruntersuchung. *Freiberger Forschungshefte / C, Geophysik*, 271, 123.
- CIE, 1931. Proceedings of the Eight Session, Commission Internationale de l'Eclairage (CIE), Paris.
- CIE, 1978. Supplement Publication No 2 to CIE Publication No 15 (1971) 'Recommendations on uniform colour spaces, colour-difference equations, and psychometric colour terms', Commission Internationale de l'Eclairage (CIE), Vienna.
- CIE, 1996. Corrected reprint of the Technical Report CIE 15.2 (1986 2. ed.), Commission Internationale de l'Eclairage (CIE), Vienna.
- Clifford, J., Binley, A., 2010. Geophysical characterization of riverbed hydrostratigraphy using electrical resistance tomography. *Near Surf. Geophys.*, 8(6), 493-501.
- Cooper, G.R.J., Cowan, D.R., 2009. Blocking geophysical borehole log data using the continuous wavelet transform. *Explor. Geophys.*, 40(2), 233-236.
- Cooper, S.S., Malone, P.G., 1992. Device for measuring reflectance and fluorescence of in-situ soil. Patent US005128882A, pp. 7.
- Coulouma, G., Samyn, K., Grandjean, G., Follain, S., Lagacherie, P., 2012. Combining seismic and electric methods for predicting bedrock depth along a Mediterranean soil toposequence. *Geoderma*, 170, 39-47.
- Crook, N., Binley, A., Knight, R., Robinson, D.A., Zarnetske, J., Haggerty, R., 2008. Electrical resistivity imaging of the architecture of substream sediments. *Water Resour. Res.*, 44.

## D

- Dachroth, W.R., 2002. *Handbuch der Baugewologie und Geotechnik*. Springer, Berlin.
- D'Affonseca, F.M., Blum, P., Finkel, M., Melzer, R., Grathwohl, P., 2008. Field scale characterization and modeling of contaminant release from a coal tar source zone. *J. Contam. Hydrol.*, 102(1-2), 120-139.
- Daubechies, I., 1992. Ten lectures on wavelets. CBMS-NSF regional conference series in applied mathematics. Society for Industrial and Applied Mathematics, Philadelphia, Pa.
- Debeglia, N., Bitri, A., Thierry, P., 2006. Karst investigations using microgravity and MASW; application to Orleans, France. *Near Surf. Geophys.*, 4(4), 215-225.
- de Lollo, J.A., Rodrigues, R.A., Elis, V.R., Prado, R., 2011. Use of electrical resistivity to identify collapsible soils in Brazil. *B. Eng. Geol. Environ.*, 70(2), 299-307.
- Dietrich, P., Leven, C., 2006. Direct push-technologies. In: J. Kirsch (Ed.), *Groundwater Geophysics*. Springer, Berlin, pp. 321-340.
- DIN 18123, 2011(04). Soil, investigation and testing - Determination of grain-size distribution [Baugrund, Untersuchung von Bodenproben - Bestimmung der Korngrößenverteilung] DIN Deutsches Institut für Normung e.V., Berlin.
- DIN 4022-3, 1982. Subsoil and ground water; designation and description of soil types and rocky soil; list of soil courses for testing and boring without continuous gaining of core trials [Baugrund und Grundwasser - Benennen und Beschreiben von Boden und Fels; Schichtenverzeichnis für Bohrungen mit durchgehender Gewinnung von gekernten Proben im Boden (Lockergestein)]. Deutsches Institut für Normung e.V., Berlin.
- DIN EN ISO14688-2, 2011(06). Geotechnical investigation and testing - Identification and classification of soil - Part 2: Principles for a classification [Geotechnische Erkundung und Untersuchung - Benennung, Beschreibung und Klassifizierung von Boden - Teil 2: Grundlagen für Bodenklassifizierungen]. DIN Deutsches Institut für Normung e.V., Berlin, pp. 16.
- DIN EN ISO22476-1, 2009(10). Geotechnical investigation and testing - Field testing - Part 1: Electrical cone and piezocone penetration tests [Geotechnische Erkundung und Untersuchung - Felduntersuchungen - Teil 1: Drucksondierungen mit elektrischen Messwertaufnehmern und Messeinrichtungen für den Porenwasserdruck]. DIN Deutsches Institut für Normung e.V., Berlin.
- DIN EN ISO22476-12, 2009(10). Geotechnical investigation and testing - Field testing - Part 12: Mechanical cone penetration test (CPTM) [Geotechnische Erkundung und Untersuchung -

---

Felduntersuchungen - Teil 12: Drucksondierungen mit mechanischen Messwertaufnehmern].  
DIN Deutsches Institut für Normung e.V., Berlin.

Douglas, B.J., Olsen, R.S., 1981. Soil classification using electric cone penetrometer - Cone Penetration Testing and Experience, ASCE National Convention, St. Louis, MO, pp. 209-227.

Duchesne, M.J., Gaillot, P., 2011. Did you smooth your well logs the right way for seismic interpretation? *J. Geophys. Eng.*, 8(4), 514.

## **E**

Eissmann, L., 1994. Grundzüge der Quartärgeologie Mitteldeutschlands (Sachsen, Sachsen-Anhalt, Südbrandenburg, Thüringen). *Altenbg. nat. wiss. Forsch.*, 7, 55-135.

EPA, 1997. Office of Solid Waste and Emergency Response: Expedited Site Assessment Tools for Underground Storage Tank Sites - A Guideline for Regulators EPA 542-R-04-017. U.S. Government Printing Office, Pittsburgh.

EPA, 2005. Office of Solid Waste and Emergency Response: Ground Water Sampling and Monitoring with Direct Push Technologies, EPA 540/R-04/2005. U.S. Government Printing Office, Washington.

Evans, C.V., Franzmeier, D.P., 1988. Color index values to represent wetness and aeration in some Indiana soils. *Geoderma*, 41(3-4), 353-368.

Evett, S.R., Tolk, J.A., Howell, T.A., 2006. Soil profile water content determination: Sensor accuracy, axial response, calibration, temperature dependence, and precision. *Vadose Zone J.*, 5(3), 894-907.

## **F**

Fernandez, R.N., Schulze, D.G., 1987. Calculation of soil color from reflectance spectra. *Soil Sci. Soc. Am. J.*, 51(5), 1277-1282.

Fernandez, R.N., Schulze, D.G., 1992. Munsell colors of soils simulated by mixtures of goethite and hematite with kaolinite. *Z. Pflanz. Bodenkunde*, 155(5-6), 473-478.

Fomel, S., 1997. A variational formulation of the fast marching eikonal solver SEP-95: Stanford Exploration Project., Stanford University.

Foti, S., Parolai, S., Albarello, D., Picozzi, M., 2011. Application of Surface-Wave Methods for Seismic Site Characterization. *Surv. Geophys.*, 32(6), 777-825.

Froese, D.G., Smith, D.G., Clement, D.T., 2005. Characterizing large river history with shallow geophysics: Middle Yukon River, Yukon Territory and Alaska. *Geomorphology*, 67(3-4), 391-406.

## **G**

Galvão, L.S., Vitorello, Í., Formaggio, A.R., 1997. Relationships of spectral reflectance and color among surface and subsurface horizons of tropical soil profiles. *Remote Sens. Environ.*, 61(1), 24-33.

Ge, J., Magnani, M.B., Waldron, B., 2010A. Imaging a shallow aquitard with seismic reflection data in Memphis, Tennessee, USA. Part I: source comparison, walk-away tests and the plus-minus method. *Near Surf. Geophys.*, 8(4), 331-340.

Ge, J.D., Magnani, M.B., Waldron, B., 2010B. Imaging a shallow aquitard with seismic reflection data in Memphis, Tennessee, USA. Part II: data analysis, interpretation and travelttime tomography. *Near Surf. Geophys.*, 8(4), 341-351.

Grey, C.E., Cooper, S.S., Malone, P.G., 1993. Method and apparatus for in-situ detection and determination of soil contaminants. Patent, pp. 9.

Grandjean, G., Bitri, A., Krzeminska, D.M., 2012. Characterisation of a landslide fissure pattern by integrating seismic azimuth tomography and geotechnical testing. *Hydrol. Proc.*, 26(14), 2120-2127.

Grundl, T.J., Aldstadt, J.H., 3rd, Harb, J.G., St Germain, R.W., Schweitzer, R.C., 2003. Demonstration of a method for the direct determination of polycyclic aromatic hydrocarbons in submerged sediments. *Environ. Sci. Technol.*, 37(6), 1189-1197.

Gourry, J.C., Vermeersch, F., Garcin, M., Giot, D., 2003. Contribution of geophysics to the study of alluvial deposits: a case study in the Val d'Avaray area of the River Loire, France. *J. Appl. Geophys.*, 54(1-2), 35-49.

Günther, T., Rücker, C., Spitzer, K., 2006. Three-dimensional modelling and inversion of dc resistivity data incorporating topography - II. Inversion. *Geophys. J. Int.*, 166(2), 506-517.

---

## H

- Harrington, G.A., Hendry, M.J., 2006. Using direct-push EC logging to delineate heterogeneity in a clay-rich aquitard. *Ground Water Monit. R.*, 26(1), 92-100.
- Hausmann, J., Dietrich, P., Vienken, T., Werban, U., Enhanced Direct Push based characterization using appropriately filtered in-situ gained soil colors. *Vadose Zone J.*, submitted.
- Hausmann, J., Steinel, H., Kreck, M., Werban, U., Vienken, T., Dietrich, P., Two-dimensional geomorphological characterization of a filled abandoned meander using geophysical methods and soil sampling. *Geomorphology(0)*., doi: 10.1016/j.geomorph.2013.07.009.
- Hawthorne, S.B., St Germain, R.W., Azzolina, N.A., 2008. Laser-induced fluorescence coupled with solid-phase microextraction for in situ determination of PAHs in sediment pore water. *Environ. Sci. Technol.*, 42(21), 8021-8026.
- Hengstermann, T., Schultze, R.H., Wollenhaupt, H., Lemke, M., 2002. In situ analysis of petroleum hydrocarbons in soils by a combination of laser induced fluorescence (LIF) spectroscopy with cone penetration tests (CPT) - Application of the OPTIMOS (Oil Pollution Transportable Independent Monitoring System) for surface and subsurface soil analysis. *Field Screening Europe 2001*, 299-302.
- Hilhorst, M.A., 2000. A pore water conductivity sensor. *Soil Sci. Soc. Am. J.*, 64(6), 1922-1925.
- Hoffmann, R., Dietrich, P., 2004. An approach to determine equivalent solutions to the geoelectrical 2D inversion problem. *J. Appl. Geophys.*, 56(2), 79-91.
- Hoffmann, S., Beilecke, T., Werban, U., Leven, C., Engeser, B., Polom, U., 2008. Joint application of shear wave seismics and direct push methods in the site investigation of an urban aquifer. *Grundwasser*, 13(2), 78-90.
- Hryciw, R.D., Chalib, A.M., Raschke, S.A., 1998. In-situ soil characterization using vision cone penetrometer, First International Conference on Site Characterization (ISC'1). Balkema, Atlanta, GA, pp. 1081-1086.
- Hryciw, R.D., Shin, S., 2004. Thin layer and interface characterization by VisCPT, Second International Conference on Site Characterization (ISC'2). Millpress, Porto, Portugal, pp. 701-706.
- Hurst, V.J., 1977. Visual estimation of iron in saprolite. *Geol. Soc. Am. B.*, 88(2), 174-176.

## I

- Ismail, A., Anderson, N., 2007. Near-surface characterization of a geotechnical site in north-east Missouri using shear-wave velocity measurements. *Near Surf. Geophys.*, 5(5), 331-336.

## J

- Jefferies, M.G., Davies, M.P., 1991. Soil Classification by the Cone Penetration Test - Discussion. *Can. Geotech. J.*, 28(1), 173-176.

## K

- Kaatze, U., 2007. Reference liquids for the calibration of dielectric sensors and measurement instruments. *Meas. Sci. Technol.*, 18(4), 967-976.
- Kästner, M., Braeckvelt, M., Döberl, G., Cassiani, G., Papini, M.P., Leven-Pfister, C., Van Ree, D., 2012. Model-Driven Soil Probing, Site Assessment and Evaluation Guidance on Technologies. Sapienza Università Editrice, Rome, Italy.
- Kater, R., Koch, T., 2007. Sachen-Anhalts verdeckte Ströme, *Mitteil. Geol. Bergw. SA. Landesamt für Geologie und Bergwesen Sachsen-Anhalt (LAGB), Halle/Saale*, pp. 135.
- Kim, Y., Oh, M., Park, J., 2007. Laboratory study on the dielectric properties of contaminated soil using CPT deployed probe. *Geosci. J.*, 11(2), 121-130.
- Knight, R., 2001. Ground penetrating radar for environmental applications. *Annu. Rev. Earth. PI Sc.*, 29, 229-255.
- Klein, G.A., 2004. *Farbenphysik für industrielle Anwendungen*. Springer, Berlin Heidelberg.
- Knödel, K., Krummel, H., Lange, G., 1997. *Geophysik. Handbuch zur Erkundung des Untergrundes von Deponien und Altlasten*. Springer, Berlin Heidelberg New York.
- Knödel, K., Lange, G., Voigt, H.-J., 2007. *Environmental Geology - A handbook of field methods and case studies*. Springer, Berlin Heidelberg.
- Kosmas, C.S., Curi, N., Bryant, R.B., Franzmeier, D.P., 1984. Characterization of Iron Oxide Minerals by Second-Derivative Visible Spectroscopy. *Soil Sci. Soc. Am. J.*, 48(2), 401-405.

- Kram, M.L., Keller, A.A., Rossabi, J., Everett, L.G., 2001. DNAPL characterization methods and approaches, part 1: Performance comparisons. *Ground Water Monit. R.*, 21(4), 109-123.
- Kram, M.L., Keller, A.A., Rossabi, J., Everett, L.G., 2002. DNAPL characterization methods and approaches, part 2: Cost comparisons. *Ground Water Monit. R.*, 22(1), 46-61.
- Kram, M.L., Keller, A.A., 2004A. Complex NAPL site characterization using fluorescence Part 2: Analysis of soil matrix effects on the excitation/emission matrix. *Soil Sediment Contam.*, 13(2), 119-134.
- Kram, M.L., Keller, A.A., 2004A. Complex NAPL site characterization using fluorescence Part 3: Detection capabilities for specific excitation sources. *Soil Sediment Contam.*, 13(2), 135-148.
- Kreck, M., 2011. Geotechnische und hydraulische Charakterisierung des Untergrundes am Deich Löbnitz mittels geophysikalischer und Direct Push gestützter Erkundung als Ergänzung zum baulichen Hochwasserschutzmaster, Martin Luther Universität Halle-Wittenberg, Halle/Saale, 69 pp.

## L

- Lee, D.S., Elsworth, D., Hryciw, R., 2008. Hydraulic Conductivity Measurement from On-the-Fly uCPT Sounding and from VisCPT. *J. Geotech. Geoenviron. Eng.*, 134(12), 1720-1729.
- Lehmann, B., 2007. Seismic traveltome tomography for engineering and exploration applications. EAGE Publications bv.
- Leven, C., Weiß, H., Koschitzky, H.-P., Blum, P., Ptak, T., Dietrich, P., 2010. Direct-Pusch-Verfahren. alllastenforum Baden-Württemberg e.V., 2010. E. Schweizerbart'sche Verlagsbuchhandlung (Nägele u. Obermiller), Stuttgart.
- Leven, C., Weiss, H., Vienken, T., Dietrich, P., 2011. Direct Push technologies – An efficient investigation method for subsurface characterization. *Grundwasser*, 16(4), 221-234.
- Levin, N., Ben-Dor, E., Singer, A., 2005. A digital camera as a tool to measure colour indices and related properties of sandy soils in semi-arid environments. *Int. J. Remote Sens.*, 26(24), 5475-5492.
- Lieberman, S.H., 1998. Direct-push, fluorescence-based sensor systems for in situ measurement of petroleum hydrocarbons in soils. *Field Anal. Chem. Technol.*, 2(2), 63-73.
- Lieberman, S.H., Knowles, D.S., 1998. Cone penetrometer deployable in situ video microscope for characterizing sub-surface soil properties. *Field Anal. Chem. Technol.*, 2(2), 127-132.
- Linder, S., Paasche, H., Tronicke, J., Niederleithinger, E., Vienken, T., 2010. Zonal cooperative inversion of crosshole P-wave, S-wave, and georadar traveltome data sets. *J. Appl. Geophys.*, 72(4), 254-262.
- Luo, Y., Xia, J., Liu, J., Xu, Y., Liu, Q., 2009. Research on the middle-of-receiver-spread assumption of the MASW method. *Soil Dyn. Earthq. Eng.*, 29(1), 71-79.
- Lunne, T., Robertson, P.K., Powell, J.J.M., 1997. Cone Penetration Testing in Geotechnical Practice. Spon Press (Taylor & Francis Group), London, New York.

## M

- Madeira Netto, J.S., 1993. Étude quantitative des relations constituants minéralogiques-réflexance diffuse des latosols Brésiliens, Université Pierre et Marie Curie, Paris, 236 pp.
- Madeira, J., Bedidi, A., Cervelle, B., Pouget, M., Flay, N., 1997. Visible spectrometric indices of hematite (Hm) and goethite (Gt) content in lateritic soils: the application of a Thematic Mapper (TM) image for soil-mapping in Brasilia, Brazil. *Int. J. Remote Sens.*, 18(13), 2835-2852.
- Malehmir, A., Bastani, M., Krawczyk, C.M., Gurk, M., Ismail, N., Polom, U., Persson, L., 2013. Geophysical assessment and geotechnical investigation of quick-clay landslides - a Swedish case study. *Near Sur. Geophys.*, 11(3), 341-350.
- Mallat, S., 2003. *A Wavelet Tour of Signal Processing*. Academic Press, Boston.
- Mathieu, R., Pouget, M., Cervelle, B., Escadafal, R., 1998. Relationships between Satellite-Based Radiometric Indices Simulated Using Laboratory Reflectance Data and Typic Soil Color of an Arid Environment. *Remote Sens. Environ.*, 66(1), 17-28.
- McCall, W., 1996. Electrical conductivity logging to determine control of hydrocarbon flow path in alluvial sediments, National Groundwater Association's Outdoor Action Conference, Las Vegas, NV, pp. 20.
- McCall, G.W., Nielsen, D.M., Farrington, S.P., Christy, T.M., 2005. Use of direct-push technologies in environmental site characterization and ground-water monitoring. In: D.M. Nielsen (Ed.), *Practical handbook of environmental site characterization and ground-water*. CRS Press Taylor and Francis Group, Boca Raton, pp. 345-471.

- Meigh, A.C., 1987. Cone penetration testing: Methods and interpretation. Butterworths, London.
- Miltitzer, H., Weber, F., 1987. *Angewandte Geophysik, Band 3. Seismik*. Akademie-Verlag, Berlin.
- Mokma, D.L., Sprecher, S.W., 1994. Water-table depths and color patterns in soils developed from red parent materials in Michigan, USA. *Catena*, 22(4), 287-298.
- Monnier, S., Camerlynck, C., Rejiba, F., Kinnard, C., Feuillet, T., Dhemaied, A., 2011. Structure and genesis of the Thabor rock glacier (Northern French Alps) determined from morphological and ground-penetrating radar surveys. *Geomorphology*, 134(3-4), 269-279.
- Mosier-Boss, P.A., Lieberman, S.H., Theriault, G.A., 2002. Field demonstrations of a direct push FO-LIBS metal sensor. *Environ. Sci. Technol.*, 36(18), 3968-3976.
- Munsell Color Company, 1994. Munsell soil color charts, revised edition. Macbeth Division of Kollmorgen Instruments Corporation, New Windsor.

## N

- Nalley, D., Adamowski, J., Khalil, B., 2012. Using discrete wavelet transforms to analyze trends in streamflow and precipitation in Quebec and Ontario (1954–2008). *J. Hydrol.*, 475, 204-228.
- Nau, G., Bucholtz, F., Ewing, K.J., Vohra, S.T., Sanghera, J.S., Aggarwal, I.D., 1995. Fiber optic IR reflectance sensor for the cone penetrometer. *P. Soc. Photo-Opt. Ins.*, 2504, 291-296.
- Neal, A., 2004. Ground-penetrating radar and its use in sedimentology: principles, problems and progress. *Earth Sci. Rev.*, 66(3-4), 261-360.
- Niederleithinger, E., Weller, A., Lewis, R., 2012. Evaluation of Geophysical Techniques for Dike Inspection. *J. Environ. Engin. Geophys.*, 17(4), 185-195.

## O

## P

- Paasche, H., Werban, U., Dietrich, P., 2009. Near-surface seismic travelttime tomography using a direct-push source and surface-planted geophones. *Geophysics*, 74(4), G17-G25.
- Paasche, H., Ohrnberger, M., Werban, U., Fechner, T., Tronicke, J., Krüger, F., Dietrich, P., 2011. Multi-scale S-wave tomography for exploration and risk assesement of development sites. *GEOTECHNOLOGIEN Sci. Rep.*, 18, 24-34.
- Paasche, H., Rumpf, M., Hausmann, J., Fechner, T., Werban, U., Tronicke, J., Dietrich, P., 2013. Advances in acquisition and processing of near-surface seismic tomographic data for geotechnical site assessment. *first break*, 18, 59-65.
- Paasche, H., Tronicke, J., 2013. Non-linear joint inversion of tomographic data using swarm intelligence. *Geophysics*, submitted.
- Pälchen, W., Walter, H., 2008. *Geologie von Sachsen*. E. Schweizerbart'sche Verlagsbuchhandlung, Stuttgart.
- Persson, M., 2005. Estimating Surface Soil Moisture from Soil Color Using Image Analysis. *Vadose Zone J.*, 4(4), 1119-1122.
- Pan, S.Y., Hsieh, B.Z., Lu, M.T., Lin, Z.S., 2008. Identification of stratigraphic formation interfaces using wavelet and Fourier transforms. *Comput. Geosci.*, 34(1), 77-92.
- Park, C.B., Miller, R.D., Xia, J., 1999. Multichannel analysis of surface waves. *Geophysics*, 64(3), 800-808.
- Park, C.B., Miller, R.D., Xia, J., Ivanov, J., 2007. Multichannel analysis of surface waves (MASW) - active and passive methods, *The Leading Edge*, pp. 60-64.
- Parolai, S., Picozzi, M., Richwalski, S.M., Milkereit, C., 2005. Joint inversion of phase velocity dispersion and H/V ratio curves from seismic noise recordings using a genetic algorithm, considering higher modes. *Geophys. Res. Lett.*, 32(1), L01303.
- Persson, M., Haridy, S., Olsson, J., Wendt, J., 2005. Solute transport dynamics by high-resolution dye tracer experiments - Image analysis and time moments. *Vadose Zone J.*, 4(3), 856-865.
- Picozzi, M., Parolai, S., Richwalski, S.M., 2005. Joint inversion of H/V ratios and dispersion curves from seismic noise: Estimating the S-wave velocity of bedrock. *Geophys. Res. Lett.*, 32(11), L11308.
- Pilz, M., Parolai, S., Picozzi, M., Wang, R., Leyton, F., Campos, J., Zschau, J., 2010. Shear wave velocity model of the Santiago de Chile basin derived from ambient noise measurements: a comparison of proxies for seismic site conditions and amplification. *Geophys. J. Int.*, 182(1), 355-367.
- Post, D.F., Fimbres, A., Matthias, A.D., Sano, E.E., Accioly, L., Batchily, A.K., Ferreira, L.G., 2000. Predicting soil albedo from soil color and spectral reflectance data. *Soil Sci. Soc. Am. J.*, 64(3), 1027-1034.

---

Prinz, H., Strauß, R., 2006. Abriss der Ingenieurgeologie. Spektrum Akademischer Verlag, Elsevir, München.

## Q

## R

- Raschke, S.A., Hryciw, R.D., 1997. Vision cone penetrometer for direct subsurface soil observation. *J. Geotech. Geoenviron. Eng.*, 123(11), 1074-1076.
- Ray, S.S., Singh, J.P., Das, G., Panigrahy, S., 2004. Use of high resolution remote sensing data for generating site specific soil management plan. *Int. Arch. Photogramm. Remote Sens. (B7) Spatial Inf. Sci.*, 35, 127-131.
- Rein, A., Hoffmann, R., Dietrich, P., 2004. Influence of natural time-dependent variations of electrical conductivity on DC resistivity measurements. *J. Hydrol.*, 285(1-4), 215-232.
- Reynolds, J.M., 1997. An introduction to applied and environmental geophysics. John Wiley & Sons, Chichester, UK.
- Robertson, P.K., 1990. Soil classification using the cone penetration test. *Can. Geotech. J.*, 27(1), 151-158.
- Robertson, P.K., 2009. Interpretation of cone penetration tests - a unified approach. *Can. Geotech. J.*, 46(11), 1337-1355.
- Robertson, P.K., Campanella, R.G., Wightman, A., 1983. SPT-CPT Correlations. *J. Geotech. Eng.*, 109(11), 1449-1459.
- Robertson, P.K., Campanella, R.G., Gillespie, D., Greig, J., 1986. Use of piezometer cone data, ASCE Specialty Conference In Situ '86: Use of In Situ Tests in geotechnical Engineering. *Am. Soc. Engin. (ASCE)*, pp. 1263-1280.
- Robertson, P.K., Woeller, D.J., Finn, W.D.L., 1992. Seismic Cone Penetration Test for Evaluating Liquefaction Potential under Cyclic Loading. *Can. Geotech. J.*, 29(4), 686-695.
- Roy, L., Sen, M.K., McIntosh, K., Stoffa, P.L., Nakamura, Y., 2005. Joint inversion of first arrival seismic travel-time and gravity data. *J. Geophys. Eng.*, 2(3), 277-289.
- Roy, S., Stewart, R.R., 2012. Near-surface Seismic Investigation of Barringer (Meteor) Crater, Arizona. *J. Environ. Eng. Geophys.*, 17(3), 117-127.
- Rubin, L.A., Marino, G.G., 1979. Engineering Geophysics Applied to Geotechnical Site Investigation. *Geophysics*, 44(3), 365-366.
- Rücker, C., Günther, T., Spitzer, K., 2006. Three-dimensional modelling and inversion of dc resistivity data incorporating topography - I. Modelling. *Geophys. J. Int.*, 166(2), 495-505.

## S

- Scheinost, A.C., Chavernas, A., Barrón, V., Torrent, J., 1998. Use and limitations of second-derivative diffuse reflectance spectroscopy in the visible to near-infrared range to identify and quantify Fe oxide minerals in soils. *Clay Clay Min.*, 46(5), 528-536.
- Scheinost, A.C., Schwertmann, U., 1999. Color identification of iron oxides and hydroxysulfates: Use and limitations. *Soil Sci. Soc. Am. J.*, 63(5), 1463-1471.
- Schmelzbach, C., Tronicke, J., Dietrich, P., 2011. Three-dimensional hydrostratigraphic models from ground-penetrating radar and direct-push data. *J. Hydrol.*, 398(3-4), 235-245.
- Schmertmann, J.H., 1978. Guidelines for Cone Penetration Test (Performance and Design). FH-TS-78-209. US Department of Transportation, Washington D.C.
- Schön, J.H., 1998. Physical properties of rocks, Fundamentals and principals of petrophysics. Elsevir.
- Schrott, L., Hufschmidt, G., Hankammer, M., Hofmann, T., Dikau, R., 2003. Spatial distribution of sediment storage types and quantification of valley fill deposits in an alpine basin, Reintal, Bavarian Alps, Germany. *Geomorphology*, 55(1-4), 45-63.
- Schrott, L., Sass, O., 2008. Application of field geophysics in geomorphology: Advances and limitations exemplified by case studies. *Geomorphology*, 93(1-2), 55-73.
- Schulmeister, M.K., Butler, J.J., Healey, J.M., Zheng, L., Wysocki, D.A., McCall, G.W., 2003. Direct-push electrical conductivity logging for high-resolution hydrostratigraphic characterization. *Ground Water Monit. R.*, 23(3), 52-62.
- Schulmeister, M.K., Buttler, J.J., Franseen, E.K., 2004. High-resolution stratigraphic characterization of unconsolidated deposits using direct-push electrical conductivity logging: A floodplain-margin example. In: J.S. Bridge, D.W. Hyndman (Eds.), *Aquifer Characterization, SEPM Concepts in Hydrogeology and Environmental Geology Vol. 2. SEPM*, pp. 67-78.
- Sethian, J.A., 1996. A fast marching level set method for monotonically advancing fronts. *P. Natl. Acad. Sci. USA*, 93(4), 1591-1595.

- Sethian, J.A., Popovici, A.M., 1999. 3-D travelttime computation using the fast marching method. *Geophysics*, 64(2), 516-523.
- Shields, J.A., Paul, E.A., Starnaud, R.J., Head, W.K., 1968. Spectrophotometric measurement of soil color and it's relationship to moisture and organic matter. *Can. J. Soil Sci.*, 48(3), 271-281.
- Shields, J.A., Starnaud, R.J., Paul, E.A., Clayton, J.S., 1966. Measurement of soil color. *Can. J. Soil Sci.*, 46(1), 83-90.
- Shinn, J.D., Timian, D.A., Morey, R.M., Mitchell, G., Antle, C.L., Hull, R., 1998. Development of a CPT deployed probe for in situ measurement of volumetric soil moisture content and electrical resistivity. *Field Anal. Chem. Technol.*, 2(2), 103-109.
- Shum, M., Lavkulich, L.M., 1999. Use of sample color to estimate oxidized Fe content in mine waste rock. *Environ. Geol.*, 37(4), 281-289.
- Shumway, R.H., Stoffer, D.S., 2011. Time series analysis and its applications. Springer Texts in Statistics. Springer, New York.
- Sinfield, J.V., Hemond, H.F., Germaine, J.T., Johnson, B., Bloch, J., 2007. Contaminant detection, identification, and quantification using a microchip laser fluorescence sensor. *J. Environ. Eng.*, 133(3), 346-351.
- Slob, E., Sato, M., Olhoeft, G., 2010. Surface and borehole ground-penetrating-radar developments. *Geophysics*, 75(5), A103-A120.
- Socco, L.V., Strobbia, C., 2004. Surface-wave method for near-surface characterization: a tutorial. *Near Surf. Geophys.*, 165-185.
- Socco, L.V., Boiero, D., Comina, C., Foti, S., Wisen, R., 2008. Seismic characterization of an Alpine site. *Near Surf. Geophys.*, 6(4), 255-267.
- Socco, L.V., Jongmans, D., Boiero, D., Stocco, S., Maraschini, M., Tokeshi, K., Hantz, D., 2010. Geophysical investigation of the Sandalp rock avalanche deposits. *J. Appl. Geophys.*, 70(4), 277-291.
- Sperling, O., Lazarovitch, N., 2010. Characterization of Water Infiltration and Redistribution for Two-Dimensional Soil Profiles by Moment Analyses. *Vadose Zone J.*, 9(2), 438-444.
- Steinel, H., 2012. Anwendungsmöglichkeiten von Rayleigh-Wellen zur Charakterisierung des oberflächennahen Untergrundes am Beispiel eines Altarms der Mulde in Nordsachsendiploma, Universität Leipzig, Leipzig, 93 pp.
- Steinel, H., Hausmann, J., Werban, U., Dietrich, P., submitted. Reliability of MASW profiling in near-surface applications. *Near Sur. Geophys.* (0).
- St Germain, R.W., Adamek, S., Rudolph, T., 2006. In situ Characterization of NAPL with TarGOST® at MGP Sites. *Land Contam. Reclam.*, 14(2), 573-578.
- Suzuki, Y., Sanematsu, T., Tokimatsu, K., 1998. Correlation between SPT and seismic CPT. *Geotech.Site Charact.*, Vol 1-2, 1375-1380.

## T

- Telford, W.M., Geldard, L.P., Sheriff, R.E., 1990. Applied Geophysics. Cambridge University Press, Cambridge.
- Tezcan, S.S., Keceli, A., Ozdemir, Z., 2006. Allowable Bearing Capacity of Shallow Foundations Based on Shear Wave Velocity. *Geotech. Geol. Eng.*, 24(1), 203-218.
- Thompson, J.A., Bell, J.C., 1996. Color index for identifying hydric conditions for seasonally saturated mollisols in Minnesota. *Soil Sci. Soc. Am. J.*, 60(6), 1979-1988.
- Tkalcic, M., Tasic, J.F., 2003. Colour spaces: perceptual, historical and applicational background, EUROCON 2003. Computer as a Tool. The IEEE Region 8, Ljubljana, Slovenia, pp. 304-308 vol.301.
- Topp, G.C., Davis, J.L., Annan, A.P., 1980. Eelectromagnetic determination of soil-water content - measurements in coaxial transmission-lines. *Water Resour. Res.*, 16(3), 574-582.
- Torrent, J., Barrón, V., 1993. Laboratory measurement of soil color: Theory and practice. In: J.M. Bigham, E.J. Ciolkosz, R.J. Luxmoore (Eds.), *Soil Color*. Soil Soc. Am., Madison, WI, pp. 21-33.
- Torrent, J., Schwertmann, U., Schulze, D.G., 1980. Iron oxide mineralogy of some soils of two river terrace sequences in Spain. *Geoderma*, 23, 191-208.
- Torrent, J., Schwertmann, U., Fechter, H., Alferéz, F., 1983. Qualitative relationships between soil color and hematite content. *Soil Sci.*, 136(6), 354-358.
- Travelletti, J., Demand, J., Jaboyedoff, M., Marillier, F., 2010. Mass movement characterization using a reflexion and refraction seismic survey with the sloping local base level concept. *Geomorphology*, 116(1-2), 1-10.

- 
- Tronicke, J., Paasche, H., U., B., 2011. Joint global inversion of GPR and P-wave seismic traveltimes using particle swarm optimization, 6th Int. Workshop on Advanced Ground Penetrating Radar (IWAGPR). IEEE, Aachen, Germany, pp. 223-226.
- Tronicke, J., Paasche, H., Boniger, U., 2012. Crosshole traveltime tomography using particle swarm optimization: A near-surface field example. *Geophysics*, 77(1), R19-R32.
- Turesson, A., 2007. A comparison of methods for the analysis of compressional, shear, and surface wave seismic data, and determination of the shear modulus. *J. Appl. Geophys.*, 61(2), 83-91.

## **U**

- Uyanik, O., 2011. The porosity of saturated shallow sediments from seismic compressional and shear wave velocities. *J. Appl. Geophys.*, 73(1), 16-24.

## **V**

- van Dam, R.L., Schlager, W., 2000. Identifying causes of ground-penetrating radar reflections using time-domain reflectometry and sedimentological analyses. *Sedimentology*, 47(2), 435-449.
- Vandenbergh, J., van Overmeeren, R.A., 1999. Ground penetrating radar images of selected fluvial deposits in the Netherlands. *Sediment. Geol.*, 128(3-4), 245-270.
- van den Boogaart, J., van Deen, J.K., Kinneging, N.A., Meyer, J.G., van Ree, C.C.D.F., 2002. The camera cone as an effective site screening tool. In: W. Breh, J. Gottlieb, H. Hötzl, F. Kern, T. Liesch, R. Niessner (Eds.), *Field Screening Europe 2001 – Proceed. Second Int. Conf. on Strategies and technologies for the Investigation and Monitoring of Contaminated Sites*. Kluwer Academic Publishers, Dordrecht, NL, pp. 107-111.
- van Huyssteen, C.W., Ellis, F., Lambrechts, J.J.N., 1997. The relationship between subsoil colour and degree of wetness in a suite of soils in the Gabrouw district, Western Cape. II. Predicting duration of water saturation and evaluation of colour definitions for colour-defined horizons. *S. Afr. J. Plant Soil*, 14(4), 154-157.
- Vienken, T., 2010. Critical evaluation of vertical high resolution methods for determining hydraulic conductivity. *Dr. rer. nat.*, Eberhard Karls Universität Tübingen, Tübingen, 101 pp.
- Vienken, T., Reboulet, E., Leven, C., Kreck, M., Zschornack, L., Dietrich, P., 2013. Field comparison of selected methods for vertical soil water content profiling. *J. Hydrol.*, 501(0), 205-212.
- Viscarra Rossel, R.A., Minasny, B., Roudier, P., McBratney, A.B., 2006. Colour space models for soil science. *Geoderma*, 133(3-4), 320-337.

## **W**

- Werban, U., Dietrich, P., 2008. Geophysics for the hydrogeological practices. *Grundwasser*, 13(2), 67-67.
- Witt, K.J. (Ed.), 2008. *Grundbau-Taschenbuch Teil 1: Geotechnische Grundlagen*. Ernst und Sohn.
- Wyszecki, G., Stiles, W.S., 1982. *Color Science: Concepts and Methods, Quantitative Data and Formulae*, 2. Wiley, New York.

## **X**

- Xia, J., Miller, R.D., Park, C.B., Ivanow, J., 2000. Construction of 2-D vertical shear-wave velocity field by multichannel analysis of surface waves technique. In: M.H. Powers, A.B. Ibrahim, L. Cramer, J.C. Wynn (Eds.), *SAGEEP 2000*, Wheat Ridge, CO, pp. 1197-1206.

## **Y**

- Yamakawa, Y., Kosugi, K., Masaoka, N., Tada, Y., Mizuyama, T., 2010. Use of a combined penetrometer-moisture probe together with geophysical methods to survey hydrological properties of a natural slope. *Vadose Zone J.*, 9(3), 768-779.
- Yamakawa, Y., Kosugi, K., Masaoka, N., Sumida, J., Tani, M., Mizuyama, T., 2012. Combined geophysical methods for detecting soil thickness distribution on a weathered granitic hillslope. *Geomorphology*, 145, 56-69.

---

## Z

- Zschornack, L., Leven-Pfister, C., 2012A. Direct Push Tools for Geophysical Measurements. In: M. Kästner, M. Braeckevelt, G. Döberl, G. Cassiani, M.P. Papini, C. Leven-Pfister, D. Van Ree (Eds.), *Model-Driven Soil Probing, Site Assessment and Evaluation - Guidance on Technologies*. Sapienza University of Rome, Rome, Italy, pp. 163-174.
- Zschornack, L., Leven-Pfister, C., 2012B. Direct Push Methods for Sampling of Soil, Soil Gas and Groundwater. In: M. Kästner, M. Braeckevelt, G. Döberl, G. Cassiani, M.P. Papini, C. Leven-Pfister, D. Van Ree (Eds.), *Model-Driven Soil Probing, Site Assessment and Evaluation - Guidance on Technologies*. Sapienza University of Rome, Rome, Italy, pp. 175-186.

### REFERENCES ON SOFTWARE AND INSTRUMENTATION

- URL 1 BIS-SH source, Geotomographie GmbH, Germany, [http://www.crosswellinstruments.de/html/s-wave\\_source.html](http://www.crosswellinstruments.de/html/s-wave_source.html), Aug 7th 2013
- URL 2 BH-geophones, Geotomographie GmbH, Germany, [http://www.crosswellinstruments.de/html/type\\_3.html](http://www.crosswellinstruments.de/html/type_3.html), Aug 7th 2013
- URL 3 Dakota Technologies Inc., ND, USA, available online: <http://www.dakotatechnologies.com/index.php/In-Situ-Tools/Soil-Color.html>, Aug 7th 2013
- URL 4 DC2DInvRes, <http://dc2dinvres.resistivity.net>, Aug 7th 2013
- URL 5 Drill log database, LfULG (Sächsisches Landesamt für Umwelt, Landwirtschaft und Geologie), Dresden, Germany, <http://www.umwelt.sachsen.de/umwelt/geologie/7649.htm>, Aug 25th 2013.
- URL 6 DT 22, Kejr Engineering Inc. – Geoprobe Systems, KS, USA, <http://geoprobe.com/dt22-soil-sampling-system>, Aug 7th 2013
- URL 7 Geodes, Geometrics Inc., San Jose, CA, USA, <http://www.geometrics.com/geometrics-products/seismographs/geode/>, Aug 7th 2013
- URL 8 Geomil Equipment BV., The Netherlands, <http://www.geomil.com>, Aug 7th 2013
- URL 9 GeoServe –Angewandte Geophysik, Kiel, Germany, <http://www.geoserve.de>, Aug 7th 2013
- URL 10 Geophones, Geospace Technologies Cooperation, Houston, TX, USA, <http://www.geospace.com/geophones-gs-20dx>, Aug 7th 2013
- URL 11 GeoTomCG, GeoTom, LLC, Apple Valley, MN, USA, <http://dev.geotom.net/>, Aug 11th 2013
- URL 12 Image Processing Toolbox, The MathWorks Inc., MA, USA, <http://www.mathworks.de/products/image>, Aug 7th 2013
- URL 13 Kansas Geological Survey, MASW, <http://www.kgs.ku.edu/software/surfseis/masw.html>, Aug 7<sup>th</sup> 2013
- URL 14 Madagascar, <http://www.ahay.org>, Aug 7<sup>th</sup> 2013
- URL 15 *MuSaWa*-project, GEOTECHNOLOGIEN, <http://www.geotechnologien.de/portal/cms/Geotechnologien/Forschung/Laufende/Tomographie/MuSaWa>, Aug 7<sup>th</sup> 2013
- URL 16 OpenDTect, <http://www.opendtect.org>, Aug 7<sup>th</sup> 2013
- URL 17 Reflex, <http://www.sandmeier-geo.de>, Aug 7<sup>th</sup> 2013
- URL 18 Ra/TT2dTom, <http://resistivity.net>, Aug 7<sup>th</sup> 2013
- URL 19 SC-500 probe, Kejr Engineering Inc. – Geoprobe Systems, KS, USA, <http://geoprobe.com/ec-electrical-conductivity>, Aug 7<sup>th</sup> 2013
- URL 20 SeisImager / SWSurfaceWaveDataAnalysis, Seismodule Controller, <http://www.geometrics.com>, Aug 7<sup>th</sup> 2013
- URL 21 SIR-30TM GPR, Geophysical Survey Systems Inc., Salem, NH, USA, <http://www.geophysical.com/sir30.htm>, Aug 7th 2013
- URL 22 Sonic drilling equipment, SonicSampDrill BV., available online <http://www.sonic-sampdrill.com/sonic-tooling/aqualock-soil-samplers.htm>, Aug 7<sup>th</sup> 2013

## Contributions

The thesis includes data that have been gathered by students and colleagues from other affiliations.

At the Löbnitz test site (→ Chapter 3) two qualification works were performed. Firstly, Manuel Kreck (*UFZ Helmholtz Centre for Environmental Research, former Martin-Luther University Halle/Wittenberg*) prepared his Master thesis (KRECK, 2011). In the thesis, we used data from *GPR* and *ERT*-investigations and the raw data of the corresponding *CPT*-log (L/CPT-1). Furthermore, Hannes Steinel (former *University of Leipzig*) prepared his Diploma thesis (STEINEL, 2012) contributing seismic data sets (*refraction seismic, multichannel analysis of surface waves*) and the soil samplings (L/SON-1–5). HAUSMANN ET AL. (2013) published the aforementioned data sets from both degree dissertations. The chapter follows this text as a modified author's version fully acknowledged to all co-authors, adjusted to BE, and expanded in the method section.

*“Notice 1: This is the author's version of a work that was accepted for publication in Geomorphology. Changes resulting from the publishing process, such as peer review, editing, corrections, structural formatting, and other quality control mechanism may not reflected in this document. Changes may have been made to this work since it was submitted for publication. A definitive version was subsequently published in Geomorphology, published online July 13th, 2013 doi:10.1016/j.geomorph.2013.07.009”*

The seismic experiment at the Löbnitz test site (→ Chapter 4) was designed and performed in close cooperation with the *MuSaWa*-project partners (Dr. Ulrike Werban, Dr. Hendrik Paasche, Michael Rumpf, etc.). Appendix B provides an overview of the project-related persons and affiliations. The picking of the seismic data obtained from the aforementioned experiment and the model generation (*P/S*-wave quantiles) with *particle swarm optimisation (PSO)* was done by Michael Rumpf (Institute of Earth and Environmental Science, University of Potsdam) providing also the description of the *PSO* in Chapter 4.3.2. We owe thanks to Dr. Thomas Fechner (*Geotomographie GmbH, Germany*) for providing support inverting the simple tomograms with *GeoTomCG* software.

The achievements in processing of *in situ*-obtained soil colours (→ Chapter 5) follow the manuscript HAUSMANN ET AL. (SUBMITTED) as a modified author's version fully acknowledged to all co-authors, adjusted to BE, and expanded in the comparison to core samples.

*“Notice 2: This is the author's version of a work that was submitted for publication in Vadose Zone Journal. Changes resulting from the publishing process, such as peer review, editing, corrections, structural formatting, and other quality control mechanism may not reflected in this document. Changes may have been made to this work since it was submitted for publication.”*

The data set of dried soil samples (T/DT-2), the T/SMP-1 and T/SMP-2, and the corresponding *CLT*-log (T/CLT-6) from the Taucha test site - published in VIENKEN ET AL. (2013) - was provided from Dr. Thomas Vienken and Manuel Kreck (*Dept. Monitoring and Exploration Technologies, UFZ Helmholtz Centre for Environmental Research*).

## Acknowledgment

Firstly, I would like to say thank Prof. Dr. Grathwohl and Prof. Dr. Peter Dietrich for their supervision of this thesis.

In particular, I owe special thanks to Prof. Peter Dietrich, Dr. Ulrike Werban, and Dr. Thomas Vienken for their support of my work during my PhD-time, as well, as for scientific advice, guidance, fruitful discussion, opportunities, and always keeping me on track.

Furthermore, thanks to all of my colleagues, who were involved in the *MuSaWa*-project (*Multi-scale S-wave tomography for exploration and risk assessment of development sites*), which was kindly funded by the BMBF *German Ministry of Education and Research*, grant 03G0745. Thanks therefore go to Michael Rumpf, Agostiny M. Lontsi, Prof. Dr. Jens Tronicke, Dr. Mathias Ohrnberger; Prof. Dr. Frank Krüger (all *University of Potsdam*, Germany), Dr. Thomas Fechner (*Geotomographie GmbH*, Neuwied, Germany), and Dr. Ulrike Werban, Prof. Dr. Peter Dietrich, and Dr. Hendrik Paasche (all *UFZ Helmholtz Centre for Environmental Research*, Leipzig, Germany).

Moreover, I would like to thank all the *good souls* of the *Dept. Monitoring and Exploration Technologies* (MET) at the UFZ such as Helko Kotas, Andreas 'Schossi' Schoßland, Marco Pohle, Simon Kögler, Daniel Steinbrückner, and Manuel Kreck for technical support throughout intensive fieldworks. A more general *thank-you* to all MET-colleagues, to the UFZ staff generally, and the *Helmholtz Interdisciplinary GRADuate School of Environmental Research* (HIGRADE) for wide-ranging across-the-board scientific input, discussions, and funding, respectively. Thanks therefore go to Dr. Steffen Zacharias, Dr. Ute Wollschläger, Dr. Jan Bumberger, Uta Sauer, Dr. Claudia Schütze, and many many others. Accordingly, I would also like to thank Hannes Steinel, Maiko Becker, and Manual Kreck for providing very good results while preparing their theses in the frame of my project, and to Marcus Jenderka (*University of Leipzig*) for assisting in programming. Further thanks to Christopher Higgins for improving my written English style.

I would like to extend a very warm thank-you to my fellow PhD-students/friends, such as Anne-Kathrin Nüsch, Ludwig Zschornack, Claudia Dierke, Hendrik Lamert, Thomas Grau, Theresa Mannschatz, Edoardo Martini, Ingmar Schröder, Tatiana Feskova, Astrid Denk, Linda Firmbach, Sophie Schelenz, Martin Schrön, Falk Händel, and M. Andrei Chirila for friendship, general support, and academic encouragement.

Most importantly of all, I would like to thank Marcia, my family, and friends for their support of and faith in my work. I dedicate this work to my son.



## Appendix A

The *MuSaWa*-project (*Multi-scale S-wave tomography for exploration and risk assessment of development sites*) was funded by the BMBF/DFG special funding program GEOTECHNOLOGIEN: *Tomography of the Earth's Crust – From Geophysical Sounding to Real-Time Monitoring*. The project was administrated by Jülich PtJ-MGS (Germany). The project duration was 01.7.2010 – 30.06.2013. Table 0-1 lists the contributing organisations including with the subproject's name. Figure 0-1 provides an overview about the objectives of the four subprojects showing the intense connections to each other.

The project's key objective is the enhancement of S-wave tomography, presenting it as a method which can be routinely applied for local-scale exploration of development sites. Additionally, the acquisition of geotechnical parameters based on *DPT* (required as a ground truthing method) and its comparability with derived parameters from geophysical data (with special focus on *seismic travelttime tomography*) and use of this information to validate reconstructed velocity models was further advanced in this project.

Table 0-1: Related affiliations in the *MuSaWa*-project and titles of the subprojects.

| <b>Affiliation, working group</b>  | <b>Subproject (SP)</b>  |
|--|---|
| Dr. Hendrik Paasche*, Prof. Dr. Jens Tronicke, Michael Rumpf<br><i>University of Potsdam, Institute of Earth and Environmental Science, Potsdam, Germany</i>                               | SP 1 – High-resolution shear wave tomography as prerequisite for reliable geotechnical appraisal of development sites: local scale    |
| Dr. Matthias Ohrnberger, Prof. Dr. Frank Krüger, Agostiny M. Lontsi<br><i>University of Potsdam, Institute of Earth and Environmental Science, Potsdam, Germany</i>                        | SP 2 – High-resolution shear wave tomography as prerequisite for reliable geotechnical appraisal of development sites: regional scale |
| Dr. Ulrike Werban, Prof. Dr. Peter Dietrich, Jörg Hausmann<br><i>UFZ Helmholtz Centre for Environmental Research, Department Monitoring und Exploration Technologies, Leipzig, Germany</i> | SP 3 – Direct Push (DP) based seismic und geotechnical measurement  |
| Dr. Thomas Fechner<br><i>Geotomographie GmbH, Neuwied, Germany</i>   | SP 4 – Development of a multistation borehole receiver array for shear wave tomography  |

\*now at UFZ Helmholtz Centre for Environmental Research, Department Monitoring und Exploration Technologies, Leipzig, Germany

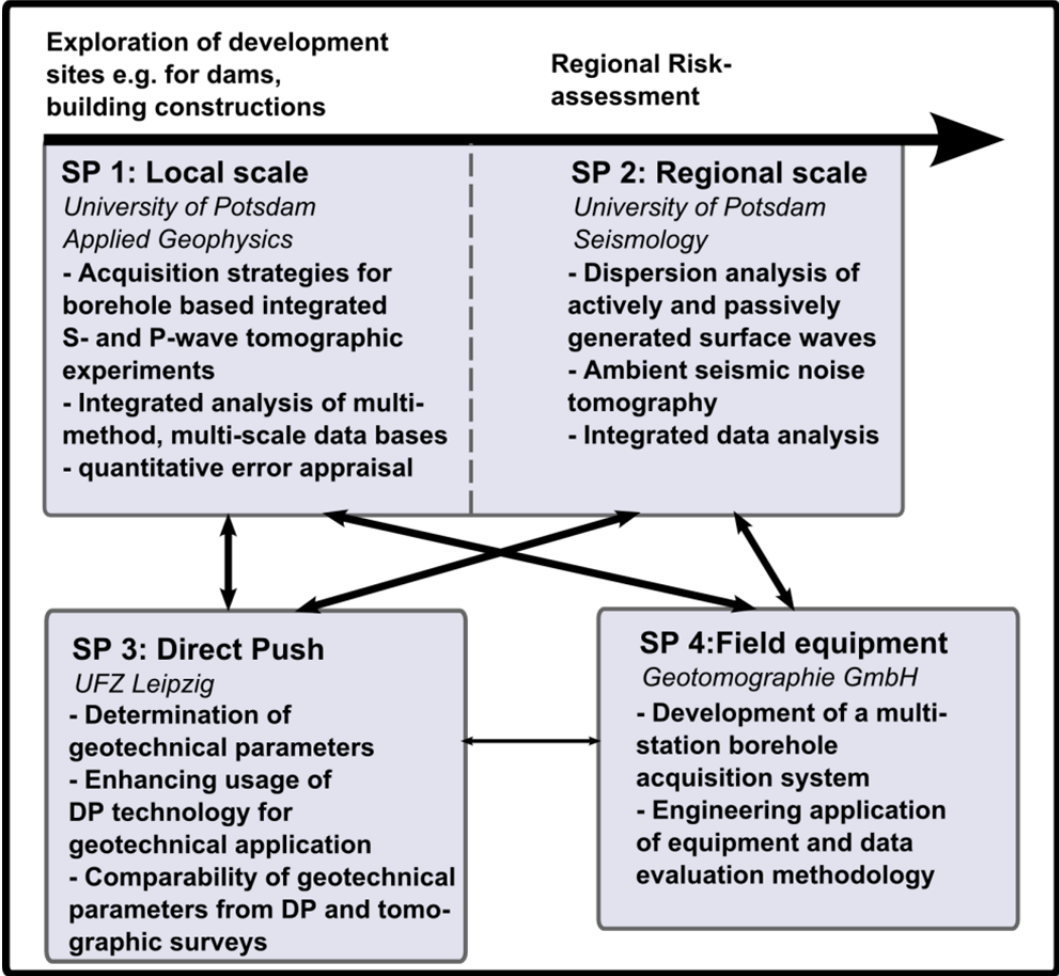


Figure 0-1: Overall concept illustrating the linkage of the subprojects and project partners as well as the spatial scale covered by the proposed project (PAASCHE ET AL., 2011).

## Appendix B

This appendix provides information about the DP-probings performed including method, name (raw data), short name (used in the thesis), performance date, investigation depth, and obtained groundwater level for the Löbnitz [L] (Table 0-1) and Taucha [T] test site (Table 0-2).

Table 0-1: Investigation depths of DP-measurements at the Löbnitz test site including ground water levels.

| Method       | Probing Name    | Short Name<br>[Thesis] | Date     | Depth<br>[m] | Water Level<br>[m] |
|--------------|-----------------|------------------------|----------|--------------|--------------------|
| <i>CPT</i>   | LOP10M095_CPT_1 | L/CPT-1                | 19.07.11 | 13.44        | 3.02               |
| <i>SONIC</i> | LO-SONIC_1      | L/SON-1                | 13.12.11 | 8.00         | N.A.               |
|              | LO-SONIC_2      | L/SON-2                | 13.12.11 | 8.00         | N.A.               |
|              | LO-SONIC_3      | L/SON-3                | 13.12.11 | 8.00         | N.A.               |
|              | LO-SONIC_4      | L/SON-4                | 13.12.11 | 8.00         | N.A.               |
|              | LO-SONIC_5      | L/SON-5                | 13.12.11 | 8.00         | N.A.               |

Table 0-2: Investigation depths of DP-measurements at the Taucha test site including ground water levels.

| Method         | Probing Name       | Short Name<br>[Thesis] | Date     | Depth<br>[m] | Water Level<br>[m] |
|----------------|--------------------|------------------------|----------|--------------|--------------------|
| <i>CPT</i>     | TAP1M80_CPT_5      | T/CPT-1                | 29.06.11 | 14.50        | 8.15*              |
| <i>DP – EC</i> | TAP1M40_EC_1       | T/EC-1                 | 20.06.11 | 13.94        | N.A.               |
|                | TAP1M50_EC_2       | T/EC-2                 | 11.05.11 | 15.21        | 6.40*              |
|                | TAP1M60_EC_1       | T/EC-3                 | 11.05.11 | 15.76        | 7.00*              |
|                | TAP1M70_EC_1       | T/EC-4                 | 11.05.11 | 15.85        | 7.77*              |
|                | TAP1M80_EC_1       | T/EC-5                 | 11.05.11 | 15.64        | 8.48*              |
|                | TAP1M90_EC_2       | T/EC-6                 | 20.06.11 | 15.68        | dry                |
| <i>SONIC</i>   | TAPM80_SONIC_1     | T/SON-1                | 23.06.11 | 16.00        | N.A.               |
| <i>DT22</i>    | TAP1M80_DT22_1     | T/DT-1                 | 13.05.11 | 15.64        | 8.20**             |
|                | vWc_Probenahme (A) | T/DT-2                 | 13.03.12 | 9.82         | 9.11               |
| <i>CLT</i>     | TAP1M50_SCOST_2    | T/CLT-50               | 09.05.11 | 16.10        | N.A.               |
|                | TAP1M60_SCOST_1    | T/CLT-60               | 10.05.11 | 15.81        | N.A.               |
|                | TAP1M70_SCOST_1    | T/CLT-70               | 10.05.11 | 16.42        | N.A.               |
|                | TAP1M80_SCOST_1    | T/CLT-80/1             | 09.05.11 | 15.96        | N.A.               |
|                | TAP1M80_SCOST_2    | T/CLT-80/2             | 23.06.11 | 15.88        | 8.15*              |
|                | TAP1M80_SCOST_3    | T/CLT-80/3             | 23.06.11 | 16.08        | 8.55*              |
|                | TAP1M80_SCOST_5    | T/CLT-80/4             | 23.06.11 | 15.86        | 8.45*              |
|                | TAP1M80_SCOST_6    | T/CLT-80/5             | 23.06.11 | 15.90        | 8.66*              |
|                | 20120315-Taucha    | T/CLT-80/6             | 15.03.12 | 9.96         | 9.02*              |
| <i>SMP</i>     | SMP_Taucha_A1      | T/SMP-1                | 13.03.12 | 9.50         | N.A.               |
|                | SMP_Taucha_A2      | T/SMP-2                | 13.03.12 | 9.26         | N.A.               |

\*depth of collapsed probing channel after pulling the probe

\*\*8.20–9.40 m water saturated core pull



## Curriculum Vitae

### Personal information:

Name: Jörg Hausmann  
DOB: 17.09.1980  
POB : Meißen  
Nationality: German



### Work Experience:

since 11/2010      Research Associate  
*UFZ - Helmholtz Centre for Environmental Research, Department  
Monitoring and Exploration Technologies, Leipzig, Germany*

02/2007 –  
10/2010      Geoscientist, Geotechnical Engineer  
*Geotechnisches Sachverständigenbüro Dr.-Ing. habil. Bernd Müller –  
Movement and Blasting Consulting, Leipzig, Germany*

### Education:

since 11/2012      PhD-student  
*Mathematisch-Naturwissenschaftliche Fakultät, Eberhard Karls  
Universität Tübingen, Germany*

since 11/2010      Helmholtz Interdisciplinary GRADuate School of Environmental  
Research (HIGRADE)

12/2006      Diploma in Geology (Diplom-Geologe, note 1.1)  
thesis: „Der Kulkwitzer See – Referenzobjekt für die Entwicklung  
anthropogener Standgewässer in der Bergbaufolgelandschaft  
Mitteldeutschlands --- Ein Beitrag zur Einordnung nach der  
Wasserrahmenrichtlinie 2000/60/EG“ [R. & M.-Teichmüller-Award,  
Deutsche Gesellschaft für Geowissenschaften e.V. (DGG) 09/2007]

10/2000 - 11/2006      degree course geology and palaeontology  
*University of Leipzig, Germany*  
*Martin Luther University Halle/Wittenberg, Germany*  
*Universidad Nacional Mayor de San Marcos, Lima, Perú [study stay  
in the framework of the German Academic Exchange Service (DAAD)  
08/2004 - 12/2004]*

07/1999 - 05/2000      Basic Military Service

07/1999      Abitur (Diploma for German secondary school qualifying for  
admission or matriculation)  
*Gymnasium Coswig (Saxony), Germany*

---